NANOPARTICLES FOR OIL DISPERSANTS AND NANO TRACERS

A Dissertation

Presented to

the Faculty of the Department of Chemical and Biomolecular Engineering

University of Houston

In Partial Fulfillment

of the Requirement for the Degree

Doctor of Philosophy

in Chemical Engineering

by

Daehak Kim

May 2015

Nanoparticles for oil dispersants and nano tracers

Daehak Kim

Approved:

Chair of the Committee
Dr. Ramanan Krishnamoorti,
Professor, Department of Chemical and Biomolecular Engineering

Committee Members:

Dr. Jeffrey Rimer,
Assistant Professor, Department of Chemical and Biomolecular Engineering

Dr. Gila Stein,
Assistant Professor, Department of Chemical and Biomolecular Engineering

Dr. Haleh Ardebili,
Assistant Professor, Department of Mechanical Engineering

Dr. Debora Rodrigues,
Assistant Professor, Department of Civil and Environmental Engineering

Dr. Suresh K. Khator,
Associate Dean, Graduate Programs,
Cullen College of Engineering

Dr. Michael P. Harold,
Chair, Department of Chemical and Biomolecular Engineering

Acknowledgements

First, I would like to thank my parents and parents in law for their financial and mental support, which made me to focus on my research works without any concerns.

And I would like to express my thanks to Dr. Ramanan Krishnamoorti for his constant encouragement and guidance during my study. I would also like to thank to Dr. Jeffrey Rimer, Dr. Gila Stein, Dr. Haleh Ardebili, and Dr. Debora Rodrigues for serving on my committee.

I am grateful to my research group members who helped and supported me throughout my study, I would like to thank Kai, Devesh, Chinedu, Katrina, Yoorang, Ryan, Titash, Kun, Jack, and Ammar. And I would also like to thank all my friends in University of Houston.

Finally, I would like to express my love and gratitude to my wife, Jungwon Jang, and my daughter Seoyeon Kim.

NANOPARTICLES FOR OIL DISPERSANTS AND NANO TRACERS

An Abstract

of a

Dissertation

Presented to

the Faculty of the Department of Chemical and Biomolecular Engineering

University of Houston

In Partial Fulfillment

of the Requirements for the Degree

Doctor of Philosophy

in Chemical Engineering

by

Daehak Kim

May 2015

ABSTRACT

Nanoparticles are promising candidates to improve the efficiency of various activities in oil and gas industry such as reservoir characterization, enhanced oil recovery, and oil dispersion due to their large surface area, interfacial activity, and tunable chemical properties. In this dissertation, the potential of surface modified inorganic nanoparticles as oil dispersants and nanosensors were examined and their behaviors were investigated. Silica nanoparticles with hydrophilic poly(oligo(ethylene oxide) monomethyl ether methacrylate) (POEOMA) homopolymer brushes were tested as oil dispersants. These hybrid nanoparticles successfully reduced hexane – water interfacial tension at low nanoparticle concentrations and oil – water emulsions formed using the nanoparticles were stable for more than 60 days. To increase interfacial activity, hydrophilic polystyrene (PS) chains were extended from the homopolymer grafted nanoparticles and synthesized amphiphilic P(OEOMA-b-sty) block copolymer grafted nanoparticles. The copolymer grafted nanoparticles presented improved interfacial activity and oil dispersion capacity. Oil – water emulsions formed by the copolymer grafted nanoparticles showed excellent stability and became solidified hard emulsions after 10 days. For both homopolymer and copolymer grafted particles, hydrodynamic diameters were the key parameter to determine their efficiency as oil dispersants. Cryo-scanning electron microscopy was used to investigate the behavior of the hybrid nanoparticles at oil – water

interfaces and the micrographs showed the segregation of the hybrid nanoparticles and their unique void-compensating behavior.

Transport behavior of negatively charged carbon nanoparticles in porous rock cores was also examined using single phase core flooding experiments and 1-dimesional convection-dispersion equation. Temperature dependence of transport parameters such as dispersion coefficients and retardation factors were evaluated. The retardation factors were inversely proportional to the rock permeabilities due to particle retention effects. Florescence microscopy revealed that the carbon nanoparticles were preferentially absorbed on the carbonate rock rather than the sandstone rock due to the surface charge effects.

Table of Contents

List of Figures

List of tables

List of Schemes

Chapter 1 Introduction

In oil and gas industry, many conventional oil fields are getting mature and recoverable amount of oil from reservoirs is decreasing. Moreover, strict environmental regulations, which most countries are imposing, as well as geopolitical problems in many oil fields make it difficult to deal with oil and gas in conventional ways. Consequently, oil industry changed their attentions to unconventional reservoirs, which situated in deep water or harsh conditions. To explore these unconventional oil fields, and producing oil and gas from them effectively and profitably, the application of new technologies is essential. However, optimal technologies to match industrial demands have not been developed completely.

First, it is required to discover and map the location of the hydrocarbon in these unconventional reservoirs. Seismic methods such as seismic reflection technique are widely used geophysical technique to characterize reservoirs. However, due to their poor resolution, inter-well information of the reservoir cannot be extracted by seismic method. The core data, whose resolution is high, only provide information from the small area of reservoir. In addition, the oil industry relied on downhole electrical and electromagnetic imaging method to improve the understanding of a reservoir. However, conventional sensors and measuring tolls are unreliable in high temperature and high pressure conditions. Moreover, to extract residual oil from the mature fields, where 60% of the original oil is still remains after conventional

recoveries, tertiary oil recovery methods, which are also known as enhanced oil recovery (EOR) methods, such as CO_2 flooding, steam flooding, and chemical flooding are required. CO_2 and steam EOR is most widely used method in United States due to the easy accessibility to their sources and their comparatively low cost. However, in CO_2 and steam flooding, the injection fluids often quickly channel through the formation bypassing most of the oil in place due to unfavorable mobility ratios. And, the application of the steam flooding is limited only for the light oils and high permeability reservoir. Chemical (polymers and/or surfactants) flooding methods have drawbacks due to their high costs and poor stability in high temperature and high pressure conditions, in spite of their high potential for the oil recovery from the heavy oil and low permeability reservoir. The oil and gas exploration and production in deep sea sites often cause environmental problems. For examples, the well-known Exxon Valdez oil spill (1989) and Deepwater Horizon oil spill (2010) made catastrophic influence on not only marine ecosystem but also financial condition of the oil production company due to the huge amount of spilled crude oil. To minimize this influence, oil dispersants were applied to the spilled oil but the environmental effects of the dispersants themselves are still questionable due to their hydrocarbon-based ingredients. According to the study conducted by Goodbody-Gringley *et al.*, the Corexit® dispersants, which were mainly used in cleanup efforts of the Deepwater Horizon oil spill, result in complete mortality of coral reefs,

which have undergone drastic declines in the last several decades even if other crude oils doesn't. Anderson *et al*. reported the Corexit® dispersants induced increase in dermal irritation and lymphocyte proliferation.

Recently, the oil industry started to use nanotechnologies, which are technologies dealing with nanomaterials, as a potential solution to these problems. Nanomaterials have a relatively high surface area compared to that of the same bulk materials with same weight, and this characteristic can enhance mechanical strength, electrical properties and make materials chemically more reactive. Such properties of nanomaterials make them useful in many areas of oil and gas exploration and production, such as drilling, reservoir mapping, oil recovery and reservoir completion. Nanomaterials are excellent tools for the development of sensors and tracing agents due to their tunable optical, magnetic and electrical properties along with their ability to form percolated structures at low volume fractions. Such nanomaterials, when combined with smart fluids, can be used as extremely sensitive downhole sensors for temperature, pressure and stress under extreme conditions.[1] Also, the replacement of metallic components and parts of the instruments with nanocomposite materials is attractive since the nanocomposite materials show better corrosion and chemical resistance as well as enhanced thermos-mechanical properties which are advantageous to withstand harsh operating conditions.[2] Nanoparticles are able to provide the improved sweep efficiency of the CO_2 EOR by producing CO_2-in-water foams

and help to recover more oil even if it is heavy oil saturated in low permeability reservoirs. The spreading force of the nanoparticle at the oil – rock interface makes it easier to detach the oil from the rock pore surface.[3] In addition, the environmentally friendly nanoparticles such as silica nanoparticles are good candidate to replace toxic chemical surfactant-based oil dispersant such as Corexit®.

This dissertation deals with two oil field applications of nanoparticles; oil dispersants and nanosensors. 15 nm silica nanoparticles with hydrophilic homopolymer brushes and amphiphilic copolymer brushes were tested as oil dispersants. The interfacial behavior of nanoparticles, whose interfacial activity was improved by tethered polymer brushes, was studied using various analytical techniques such as pendant drop interfacial tension measurement, small angle X-ray scattering, and Cryo-scanning electron microscopy. Moreover, transport behavior of negatively charged carbon nanoparticles in porous media under different conditions such as temperature, permeability, and surface charge was also investigated using core flooding experiment for their reservoir mapping and sensing application.

Chapter 2 Background

2.1. Nanotechnologies for oil and gas industry

2.1.1 Sensors

Nanoparticles' distinctive optical, magnetic, and electrical properties, which can be tuned by varying molecular parameters, as well as their ability to form percolating structures at their low concentration, make them attractive to be used as nanosensors.[1] In order to characterize oil reservoirs and locate target hydrocarbons, various techniques have been used in oil fields. Seismic methods such as a seismic reflection technique are widely used geophysical technique to characterize reservoirs. However, the vertical resolution of the seismic methods can be an issue in spite of their benefits like low cost, wide range of investigation. The seismic methods often fail to resolve the important small scale features which allow one to characterize the reservoir for such applications as flow simulations or the accurate placement of directional wells. Core and log data provide high resolution, but they only cover the information from limited range of reservoir. Nanosensors, mainly composed of nanoparticles, are promising reservoir exploration media which can overcome the drawbacks of both seismic methods and core/log analysis. If surfaces of the nanoparticles were tuned to be sensitive to chemical and physical properties of the reservoir fluids or rocks, they can be used as contrast agents to map inter – well matrix with high resolution and large range of investigation.

Recently, theoretical and experimental studies about the flow of multiphase fluids containing nanoparticles in porous media have been reported. Ryoo *et al*. conducted experimental and modeling study using paramagnetic nanoparticles as nanosensors. They measured oil – water interface displacements induced by nanoparticles under a magnetic field and expected to possibly sense oil in rock pores by measuring acoustic pressure wave generated from the displacement.[4] Kotsmar *et al.* studied the transport of magnetic iron oxide nanoparticles in the negatively charged core. Superparamagnetic nanoclusters of iron oxide particles were stabilized with small amounts of citrate ions in water and the nanoparticle dispersions were stable more than 2 month. Their strong negative charge indicates that the citrate ions provide electrostatic stabilization in aqueous solutions. The cluster sizes decreased with increasing pH up to pH 8, but became unstable at more than pH 10, which indicates competition in complex formation with the iron cations on the nanoparticle surface between the carboxylate group of the citrate ions and the hydroxide ions. Core flooding experiments with these nanoparticles showed their no retention in negatively charged cores due to their negative surface charge and small size.[5] Yu *et al.* observed the effect of the salt on the breakthrough time and nanoparticle retention by the core flooding experiment with the carbon nanoparticles and dolomite cores. They reported the high ionic strength dependence of the breakthrough of the carbon nanoparticles and conjectured that this was due to the charge

interaction of carbon nanoparticles - carbon nanoparticles and carbon nanoparticles – porous medium. And, this surface charge interaction was suppressed by surface modification techniques. They also produced transport parameters of nanoparticles in porous media such as dispersion coefficients and retardation factors using CXTFIT code.[6]

2.1.2 Nanocomposites

Due to the harsh conditions of unconventional oil fields, drilling and production activities are required to move deeper and remote area. Therefore, the development of materials with better mechanical, chemical, and thermal stability is essential. It is well known fact that the incorporation of nanoparticles into matrix materials can make them stronger and more durables. Compared to the metal based materials, the nanopariticle-incorporated materials and coatings can provide oil field equipment with better chemical resistance, anti-corrosion capacity, and lighter weight along with similar mechanical strength. Therefore they are promising materials for the process in harsh environments of unconventional oil fields.

According to the study of Amirpasha *et al*., the moisture transport performance and acid resistance of concrete pipes were significantly improved by applying small amount of graphite nanoplatelets. In order to assess the effects of graphite nanoplatelets, they prepared industrial-scale concrete pipes. By physisorption of polyacrylic acid (PAA) polyelectrolyte, the dispersion of the graphite nanoplatelets in concrete was improved. Unsing

only 0.05 vol% of graphite nanoplatelets in concrete, improvements in moisture transport performance and acid resistance of the concrete exceeded that from polyvinyl alcohol (PVA), which is a conventional concrete reinforcing additive.[7]

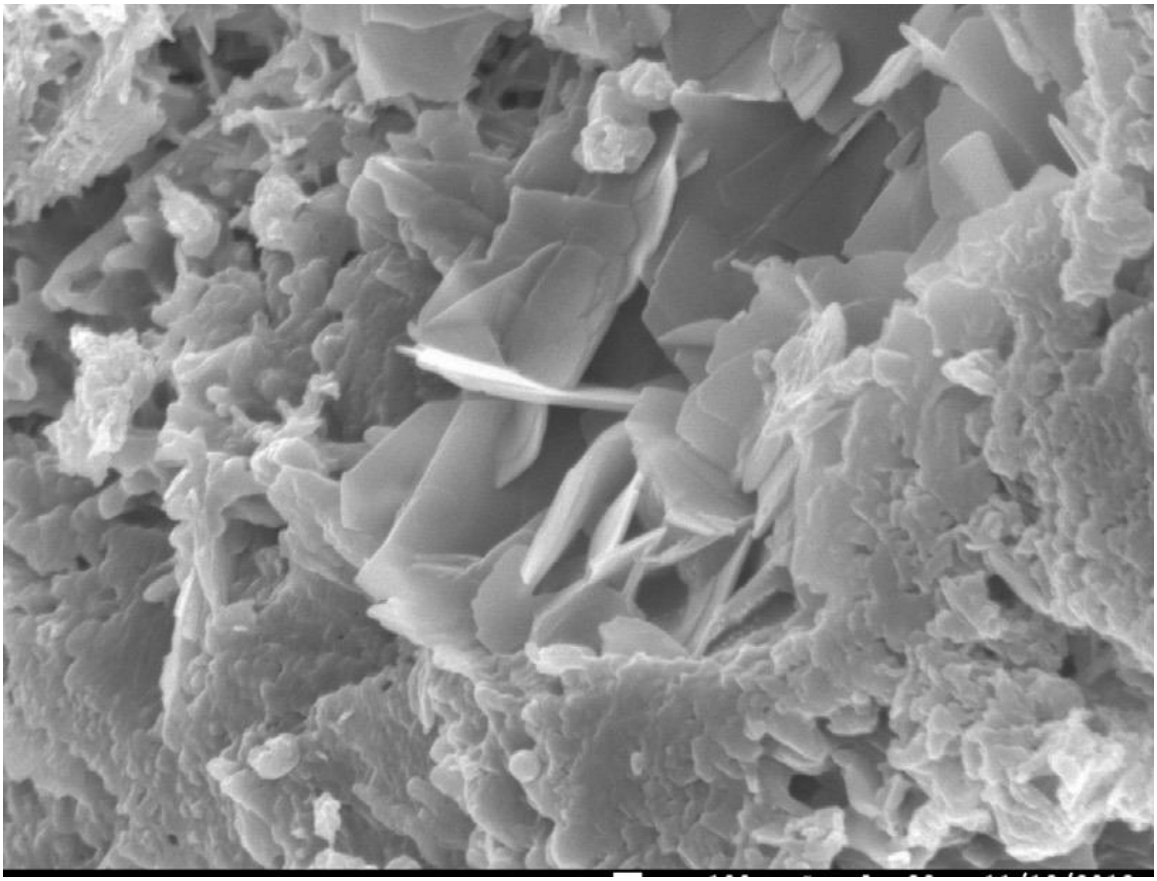

Figure 2.1 SEM images of graphite nanoplatelets in dry-cast concrete

Baker *et al.* reported that the transition metal nitride-nanocrystal nanocomposite (TiAlBN) provided more sustainability, hardness, and oxygen resistance to the metal alloy based drill. They deposited a range of TiAlBN

coating using an electron beam evaporation method and searched the optimal composition which can maximize the effect of the coating. According to their experimental results, the optimum microstructure for wet drilling applications consists of 26 nm (Ti,Al)N grains separated by 3 nm regions of amorphous.[8]

2.1.3 Drilling and completion

The efficiency of a "smart fluid", a fluid whose properties can be altered by stimulus such as electric field or pH, is facilitated by nanoparticles and this smart fluid can be applied to drilling, production and completion processes in oil and gas industry. The high surface to volume ratio of the nanoparticles, induced by their nanometer-scale size, causes the fluid to interact with the surrounding environment at very low concentrations. Abdo *et al*. tested palygorskite (Pal), which is natural hydrous clay nanoparticles with fibrous rod-like structure, for use in drilling fluids. Pal showed the capability to tailor the properties of drilling fluids by reducing the particle size. Moreover, pal had good stability at high temperature and pressure.[9] According to Wasan and Nikolov's study about the spreading behavior of smart fluids, the nanoparticles in smart fluids tend to spread into rock – fluid interface, providing the structural disjoining force, thereby improve drilling performance.[10] Nanoparticles in smart fluid also can improve the hydraulic fracturing process. Proppants are injected during hydraulic fracturing process to open the fractures for oil and gas to flow into the wellbore.

However the industry is required to develop proppants with higher mechanical strength and lighter weight to transport them to deeper into the formation. Conventional proppants travel only 100 – 130 feet in shale and tight sands reservoirs. Therefore, developing a more buoyant proppant that is light enough to go 180 feet or more into the reservoir, but strong enough to withstand high closure stresses is required.[11] The effect of nanoparticles on the proppant fluid was reported by Baker Hughes. By using nano-structured metal composites as proppants, the improved strength and the ability to be pumped away were achieved.[12]

2.1.4 Oil dispersants

When oil spill occurs, brown-colored continuous band of oil, called "oil slick" is formed on the ocean surface. This oil slick makes serious effects on marine lives by preventing the gas exchange and light penetration as well as sticking into their skin and feather.[13] In order to remove the oil slick, booming, skimming and direct combustion can be used,[14,15] but their efficiency is limited as the area of the oil spill is wide and strongly affected by weather conditions. Consequently, large amount of oil dispersants have been sprayed on the oil slick or injected directly into subsea and point sources to deal with the oil spills.[16] For example, when Deepwater Horizon oil spill occurred, some of commercial oil dispersants (Corexit9527®, Corexit9500®, Nalco Holding Company), which were mainly composed of chemical surfactants and solvents, were chosen based on their least toxicity and oil

dispersing efficiency, and total 1.8 million gallons of these dispersants were applied into the Gulf of Mexico.

However Corexit9527® was prohibited to be used in early stage of the oil spill due to the one of their main ingredients, 2-butoxyethanol, which can damage male reproductive system and also cause cancer. Moreover, lots of environmental studies have reported the harmful effects of these dispersants on marine lives. Rico-Martinez *et al.* studied the acute toxicity of Corexit9500® and crude oil mixture to the rotifers and reported that the acute toxicity of each Corexit9500® and crude oil was similar and acceptable, but their mixture showed 52 times higher toxicity.[17] Hamdan *et al.* presented that Corexit9500® reduce the population of hydrocarbon-degrading microorganism, so the capacity of natural oil degradation can decrease.[18] Therefore, it is required to develop less toxic and environment-friendly oil dispersants, which can replace the commercial chemical surfactant-based oil dispersants. One of the possible candidates for these alternative dispersants is small particles such as nanoparticles. Small particles can segregate at oil – water interface and produce emulsions by reducing their interfacial energy. Recently, a number of dispersants based on nanoparticles including silica, clay, iron oxide, and carbon black have been tested.

Rodd *et al.* reported the oil dispersing efficiency and environmental impact of the surface-modified carbon particles. They functionalized the surface of carbon black particles using diazonium chemistry to increase their

hydrophilicity and studied their impact on brine shrimp. The surface functionalization for increased hydrophilicity could not only improve the performance of particle-based dispersants but also reduce their adverse environmental impacts on marine organisms.[19] Dong *et al*. tested the clay microparticles as oil dispersants. With clay particles and small amount of surfactants (0.001% w/v), stable oil – water emulsions were formed by synergistic effect of their combination in spite of the poor interfacial activity of each clay particle and surfactant.

2.1.5 Enhanced oil recovery (EOR)

As more than 60% of original oil in place (OOIP) remains in reservoir after primary and secondary recoveries, additional oil recovery is needed. Steam, CO_2, and chemicals are commonly used to extract remaining heavy and unrecoverable oil. These EOR agents alter the mobility, solubility, and wettability of unrecoverable oil and make them recoverable. In addition to these conventional EOR agents, nanoparticles can also be used as an alternative. It has been reported that the nanoparticles can change the rock wettability to water-wet state and stimulate additional recovery as, for example, silicon oxide dispersed in ethanol is a good candidate.[20,21] The sweep efficiency can also be improved using nanoparticles by increase viscosity of injecting fluids in spite of their comparatively low concentrations due to their high surface to volume ratio.[22] Moreover, nanoparticles can provide

structural disjoining pressure helping in the detachment of oil from the rock surface.[21]

Zhang *et al*. tested the efficiency of 19 nm hydrophilic silica particles as EOR agents and studied the underlying mechanism of oil recovery induced by nanoparticles. As Wasan and Nikolov reported first, the nanofluid wedge film spread to oil – rock interface and the structural disjoining pressure played an important role (Figure 2.2). Thus, 55% crude oil was recovered by silica nanofluid, compared to only 17% recovered by the brine solution.[23]

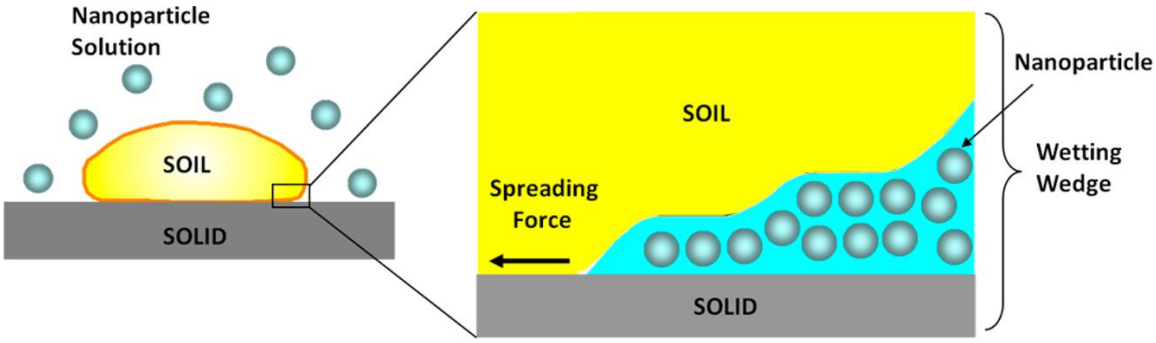

Figure 2.2 Oil – solid displacement driven by film tension gradient and the role of structural force.

In addition, nanoparticles can be used to stabilize CO_2 foams. Because of the very low viscosity of CO_2 gas, they preferentially channel through high-permeability layers of reservoir resulting in the poor sweep efficiency. Generally surfactant-stabilized CO_2 foams are used to increase viscosity for CO_2 EOR, but foams stabilized by nanoparticles provide additional advantages for EOR applications. Due to their comparatively large

adsorption energy, the stability of the foams can be improved. Moreover, Nanoparticle-stabilized foams exhibit better thermal stability compared to the surfactant-stabilized foams. Espinosa *et al*. reported the formation of the very stable CO_2-in-water foams using polyethylene glycol-functionalized silica nanoparticles, which is two to eighteen times more resistant to flow than the same fluids without nanoparticles.[24]

2.2 Oil – water emulsion

2.2.1 Oil dispersing mechanism

When the oil spill occurs, oil dispersants are applied to the oil slick to disperse it to micrometer-sized emulsion droplets by natural energy source such as wind and ocean wave. These dispersed small oil droplets are consumed by microbial lives in the ocean (Figure 2.3). Generally, the oil dispersants are composed of surfactants and solvents. When the oil dispersants were sprayed, the solvents carry the surfactant molecules to the oil slick. Since the surfactant molecules have both hydrophilic part and oleophilic part, they segregate at oil-water interface and reduce their interfacial tension. Under the reduced interfacial tension, it is easier to make small emulsion droplets by wind or wave. Production of such small oil emulsion droplets increases their surface area dramatically and facilitates the biodegradation of spilled oil due to the increased opportunity for microbial living in the ocean to contact the oil phase.

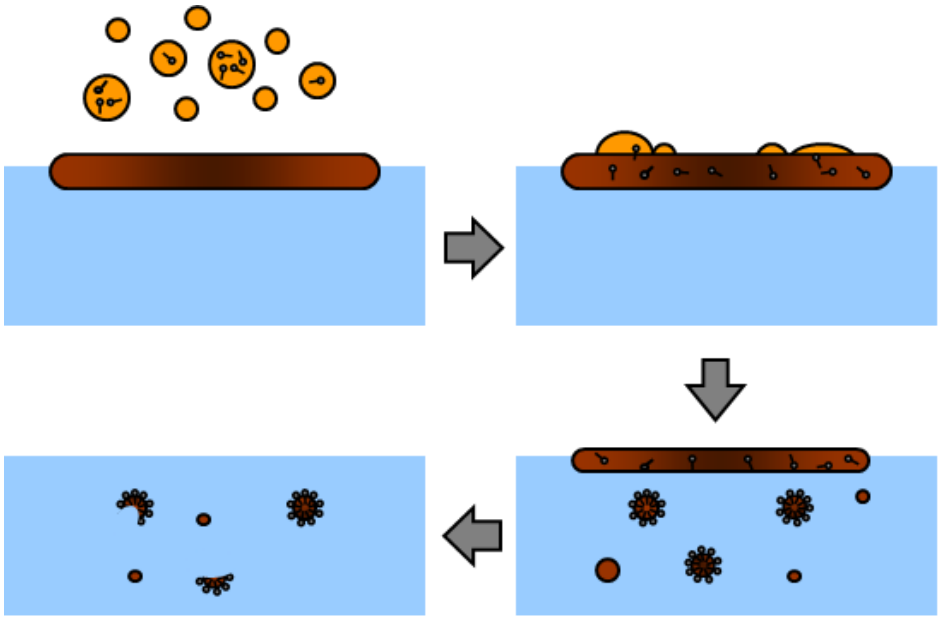

Figure 2.3 Oil disperse mechanism

2.2.2 Emulsion destabilizing mechanisms

Without proper emulsifiers, the emulsification is thermodynamically unfavorable process due to the increase in interfacial free energy induced by increasing interfacial area. Therefore, emulsions collapse over time (demulsification) as the two immiscible phases tend to minimize their contact area. There are four main mechanisms that cause demulsification, which are creaming, aggregation, coalescence, and Ostwald ripening (Figure 2.4). The creaming (or sedimentiation) is induced by differences in density between the two phases and this leads to phase separation due to the effect of gravity.[25]

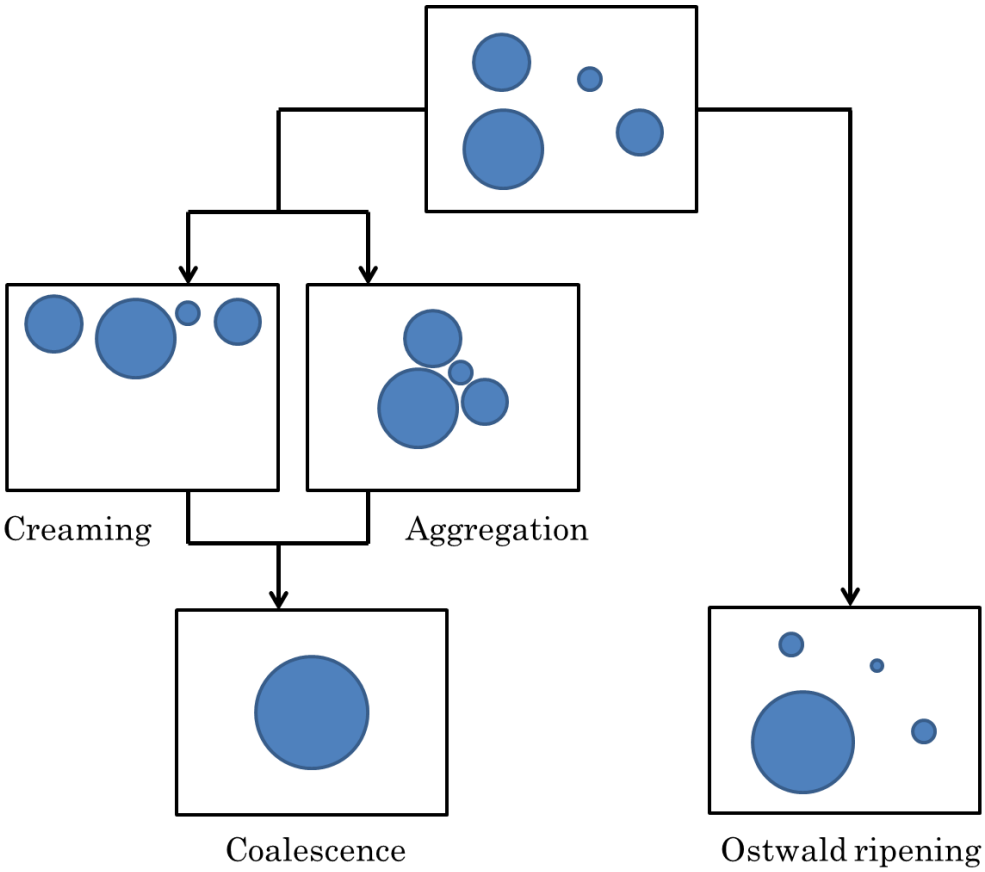

Figure 2.4 Demulsification mechanisms

The aggregation of emulsion droplets occurs due to attractive forces between colloids, which is well-described by the Derjaguin, Landau, Verwey and Overbeek (DLVO) theory.[26] The aggregation of colloidal particles (or droplets) relies on the interactions (attraction and repulsion) between two particles as a function of inter-particle distance. For the emulsion droplets, the attraction arises from their London-van der Waals forces and repulsion arise from emulsifier molecules such as surfactants at the fluid interface.[27] When the emulsion droplets assemble by the creaming or aggregation, colliding droplets

can form a single larger droplet by the coalescence if the energy barrier between droplets can be overcome by their attractive force. Ostwald ripening is the growth of larger droplets at the expense of smaller ones and is related to the solubility difference between small and large droplets.[28]

2.2.3 Creaming (sedimentation)

The differences in density between the continuous phase and the dispersed phase are driving the sedimentation process. For water-in-oil emulsions, the sedimentation process of the emulsion droplets is well described by the Stokes equation which is expressed as

$$V_m = \frac{gD^2(\rho_w - \rho_o)}{118\mu_o}, \quad \text{(Eq. 2.1)}$$

where, V_m is the velocity of the droplet sedimentation, g is the acceleration due to gravity, ρ_w is the density of the dispersed phase (water), ρ_o is the density of the continuous phase (oil), and μ_o is the viscosity of the continuous phase (oil). The sedimentation rate is faster when the droplet size is larger and density difference is bigger. The term "sedimentation" is used when the droplets move to the direction of the gravity for the system with $\rho_w - \rho_o > 0$. Otherwise, the term "creaming" is used when the droplets float against the direction of the gravity ($\rho_w - \rho_o < 0$). Water-in-oil emulsions and solid particle dispersions normally present sedimentation. Oil-in-water emulsions and gas bubbles usually show creaming process.

However, the Stokes equation does not well describe the sedimentation of the emulsion droplets if the system is not composed of diluted

dispersions.[29] When the volume fraction of the dispersed emulsion droplets (ϕ) is large enough (> 0.01), the hindered sedimentation can be observed. A empirical study was reported in order to describe the hindered sedimentation. Richardson *et al.* proposed an empirical equation about the effect of volume fraction of the dispersed emulsion droplets on the reduction of sedimentation rate as

$$\frac{V_{m,H}}{V_m} = (1-\phi)^n, \qquad \text{(Eq. 2.2)}$$

where, $V_{m,H}$ is the hindered sedimentation rate and n is an empirical constant.

2.2.4 Aggregation and coagulation

The aggregation of emulsion droplets takes place as a result of the balance between their attractive and repulsive interactions. This colloidal interaction between the droplets (or particles) is well explained by DLVO theory, developed by Derjaguin, Landau, Verwey and Overbeek.[30,31] This theory considers the force between two close particles as the result of long range van der Waals attraction and electrostatic repulsion induced by the overlap of electrical double layers of their charged surfaces. H. Hamaker derived an expression for the London-van der Waals attraction, U_A of two spherical particles with radius a and center-to-center distance H by integrating the interaction energy dU_A over the total volumes of the two particles.[32]

$$U_A = -\frac{A}{6}\left[\frac{2a^2}{h^2+4ah} + \frac{2a^2}{h^2+4ah+4a^2} + \ln\left(\frac{a^2+4ah}{h^2+4ah+4a^2}\right)\right] \quad \text{(Eq. 2.3)}$$

$$h = H - 2a,$$

where, A is Hamaker constant and h is the minimum distance between the two approaching surfaces. If h is sufficiently larger than a, this equation can be simplified as

$$U_A = -\frac{Aa}{12h}. \quad \text{(Eq. 2.4)}$$

On the other hand, the analytical expression of electrostatic energy, U_E, for two approaching spherical particles with electrical double layers on their surface does not exist but approximate expressions have been suggested as

$$U_E = \frac{64\pi a c_0 N_A kT \aleph_0^2}{\kappa^2}\exp(-\kappa h), \quad \text{(Eq. 2.5)}$$

where, c_0 is the bulk concentration of the ionic specie, N_A is the Avogadro's number, $\aleph_0 = \tanh(ze_0\psi_0/4kT)$ (z is the magnitude of the ion valence, e_0 is the electronic charge), κ^{-1} the Debye length indicating the thickness of the electrical double layer, and ψ_0 the electrical potential at the interfaces. This expression is valid if the radius is much larger than the Debye length.

The overall interaction energy of the two colloidal droplets (or particles), U, is the sum of the London-van der Waals force (U_A) and electrostatic force (U_E). At very close droplet-droplet distance (primary minimum), attractive forces is dominant and the droplets are expected to

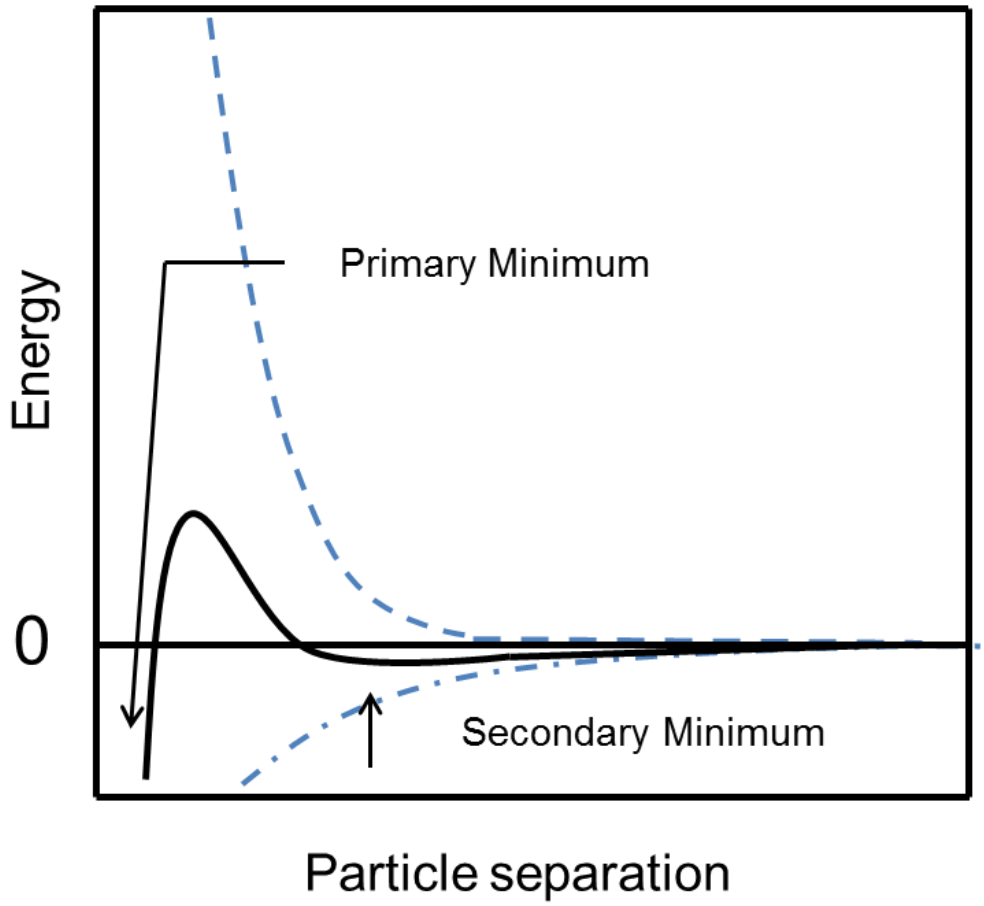

Figure 2.5 Particle-particle interaction energy as a function of the particle separation.

aggregate irreversibly (coagulation). When a secondary energy minimum appears, particles aggregate reversibly and it is possible for them to be dispersed again (aggregation). The overall interaction energy profile depicted in Figure 2.5 is also useful to understand the kinetics of aggregation. If U_{max}, which is the maximum peak shown in the overall interaction energy plot, is zero, there is no energy barrier to prevent the two surfaces from approaching

each other. Therefore fast aggregation occurs. In contrast, if $U_{max} > 0$, an energy barrier must be overcome to achieve aggregation (slow aggregation).

2.2.5 Ostwald ripening

Ostwald ripening is a process whereby larger droplets grow by diffusion at the expense of smaller ones because the solubility of a component in a droplet increases as the interfacial curvature increases. The first detailed theory for Ostwald ripening was developed independently by Lifshitz and Slevoz, and by Wagner. They assumed dilute system where a droplet growth is independent of its surrounding and considered the diffusion of dispersed phase across the droplet boundary. They reported that there is a critical droplet radius a_c. If the droplet diameter a is larger than a_c, it grows, whereas a is smaller than a_c, it shrinks. The mean particle radius ($\bar{a}$) was a function of time and can be expressed as

$$\bar{a}^3 = \bar{a}_0^3 + \frac{4}{9}Kt, \qquad \text{(Eq. 2.6)}$$

where, $\bar{a}_0$ is the initial mean radius, t is the time, and K is a constant that depends on interfacial energy, diffusion coefficient. The droplet size distribution function was derived as

$$f(\rho) = \frac{4}{9}\rho^2 \left(\frac{3}{3+\rho}\right)^{\frac{7}{3}} \left(\frac{3}{3-2\rho}\right)^{\frac{11}{3}} \exp\left(-\frac{2\rho}{3-2\rho}\right), \qquad \text{(Eq. 2.6)}$$

$$\rho \geq \frac{3}{2},$$

where, $\rho = a/\bar{a}$. This probability density function describes emulsion droplets mainly grown by diffusion.

2.3 Thermodynamics of a particle at oil – water interface

2.3.1. A particle with homogeneous surface nature at oil – water interface

Particles can reduce the interfacial tension of two immiscible fluids and stabilize their emulsion by being segregated at their interface. This colloidal emulsion system, which is stabilized by small particles, is called "Pickering emulsion". When a fluid containing the particles faces another immiscible fluid, the particles tend to place at the interface of two fluids because the free energy of the particles at interface is lower than the free energy of particles dispersed in the bulk fluid.

The free energy of a system that a particle were situated at the oil – water interface can be expressed as

$$F = \gamma_{12}A_{12} + \gamma_{p1}A_{p1} + \gamma_{p2}A_{p2} + \tau L - \gamma_{12}A_{st}, \qquad \text{(Eq. 2.7)}$$

where A_{ij} is the contact area of two different phases, A_{st} is the contact area removed by nanoparticles from original interface between two fluids and L is length of the three phase contact line. γ_{ij} refers to the interfacial tension of species i and j, and τ represent the line tension, which are given by

$$\gamma_{ij} = \left(\frac{\partial F}{\partial A_{ij}}\right) \text{ and} \qquad \text{(Eq. 2.8)}$$

$$\tau = \left(\frac{\partial F}{\partial L}\right). \qquad \text{(Eq. 2.9)}$$

Also, the free energy of the system that the particle immersed in one of the fluid can be expressed as,

$$F_0 = \gamma_{12}A_{12} + \gamma_{p1}A_p. \qquad \text{(Eq. 2.10)}$$

Accordingly, the free energy difference of particle absorption at interface is derived from above two equations as

$$F_{int} = \left(\gamma_{12}A_{12} + \gamma_{p1}A_{p1} + \gamma_{p2}A_{p2} + \tau L - \gamma_{12}A_{st}\right) - \gamma_{12}A_{12} - \gamma_{p1}A_p. \qquad \text{(Eq. 2.11)}$$

This can be simplified using the relation, $A_p = A_{p1} + A_{p2}$ as

$$F_{int} = \left(\gamma_{p2} - \gamma_{p1}\right)A_{p2} - \gamma_{12}A_{st} + \tau L. \qquad \text{(Eq. 2.12)}$$

This is the general equation of the particle placed at the interface of two immiscible fluids which was not relevant to the shape of the particle.[33]

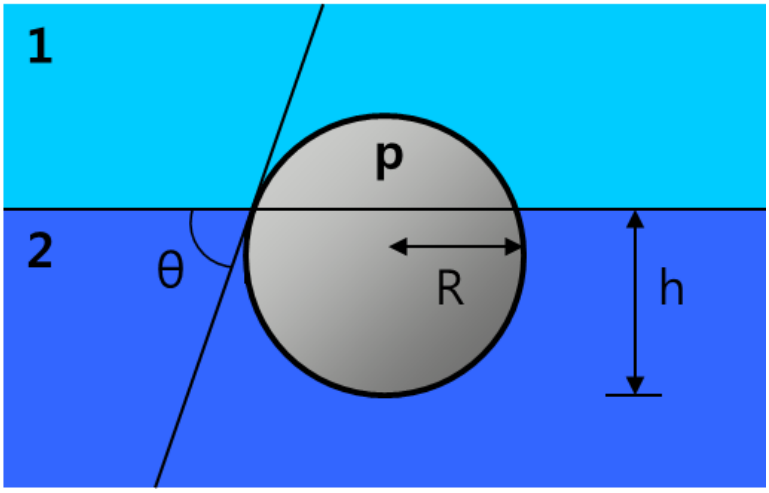

Figure 2.6 A spherical particle placed at the interface of two immiscible fluids

For a spherical particle, A_{p2} (particle-water contact area) is expressed with $2\pi Rh = 2\pi R^2(1 - \cos\theta)$ and A_{st} can be replaced with $\pi R^2\sin\theta = \pi R^2(1 - \cos^2\theta)$, where R is the radius of the particle, h is the depth of immersion and θ

is the contact angle of the water on the particle surface (Figure 2.6). And, from the Young's equation, the interfacial tensions have a relationship as

$$\gamma_{p1} - \gamma_{p2} = \gamma_{12} \cos\theta. \quad \text{(Eq. 2.13)}$$

Since the effect of gravity and line tension are small enough, they can be neglected. Then, the equation (2.6) is converted to

$$F_{int} = -\pi R^2 \gamma_{12}(\cos\theta \pm 1), \quad \text{(Eq. 2.14)}$$

where, γ is the interfacial tension between two immiscible fluids, and θ is a water contact angle on the particle surface.[33,34] The sign inside the bracket is negative for a particle originally dispersed in water phase, and positive for a particle originally dispersed in oil phase. Since F_{int} has always a negative sign regardless of the signs and values of the other parameters, small particles preferentially segregate into fluid interface and reduce the interfacial energy. Reduction of the interfacial energy with the small particles is maximized with contact angle (θ) of 90˚ and minimized with contact angles of 0 and 180˚. However, it is limited for nanoparticles to reduce the interfacial energy due to their small radius even if the contact angle is 90˚, thus additional techniques are required to improve their interfacial activity and use them as efficient emulsion stabilizers.

2.3.2. A particle with Janus surface nature at oil – water interface

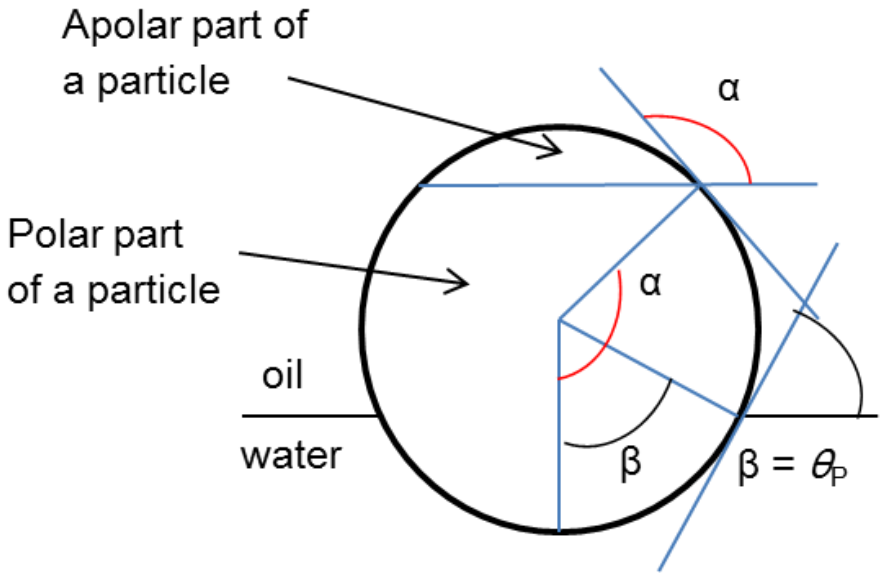

Figure 2.7 Geometry of amphiphilic Janus particles situated at oil-water interface

Binks *et al.* theoretically predicted the improvement of the interfacial activity of the "Janus" particle, a particle has two different surface regions with two contact angles, compared to the particle with homogeneous surface wettability.[35] A simple system where a amphiphilic Janus particle situated in oil – water interface was defined as Figure 2.7. The ratio of apolar and polar region is determined by angle α (0°< α <180°, α = 0° or 180°: homogeneous particle). Contact angle of apolar and polar region are θ_A and θ_P respectively (0°< $\Delta\theta$ <90°). The amphiphilicity was defined as $\Delta\theta = (\theta_P - \theta_A)/2$. The free energy of the system composed of amphiphilic Janus particle at oil – water interface is given as

For $\beta \leq \alpha$

$$E(\beta) = 2\pi R^2 \left[\gamma_{AO}(1+\cos\alpha) + \gamma_{PO}(\cos\beta - \cos\alpha) + \gamma_{PW}(1-\cos\beta) - \frac{1}{2}\gamma_{OW}(\sin^2\beta)\right] \text{ and} \quad \text{(Eq. 2.15)}$$

For $\beta \geq \alpha$

$$E(\beta) = 2\pi R^2 \left[\gamma_{AO}(1+\cos\beta) + \gamma_{PO}(\cos\alpha - \cos\beta) + \gamma_{PW}(1-\cos\alpha) - \frac{1}{2}\gamma_{OW}(\sin^2\beta)\right]. \quad \text{(Eq. 2.16)}$$

This expression of the free energy was referenced by the free energy of the original state which the particles dissolved in one of the phase (oil or water). Then, the equation was plotted with average contact angle which was set as

$$\theta_{average} = \frac{\theta_A(1+\cos\alpha)+\theta_P(1-\cos\alpha)}{2}. \quad \text{(Eq. 2.17)}$$

For a half polar and half apolar particle (α=90°), the free energy (adsorption energy) of the particle at oil-water interface increased with increasing amphiphilicity through the whole average contact angle range. Desorption energy of homogeneous particles ($\Delta\theta$ = 0°) is less than desorption energy of Janus particles ($\Delta\theta$ > 0°) Unlike homogeneous particles, Janus particles retain their adsorption even for average contact angle of 0° and 180° (Figure 2.8). Therefore, it theoretically shows that amphiphilic Janus particles can be more efficient emulsion stabilizers than homogeneous particles.[35] Inspired by this theoretical study, the effectiveness of the Janus nanoparticles as emulsion stabilizer was confirmed experimentally by Glaser *et al.*[36] They

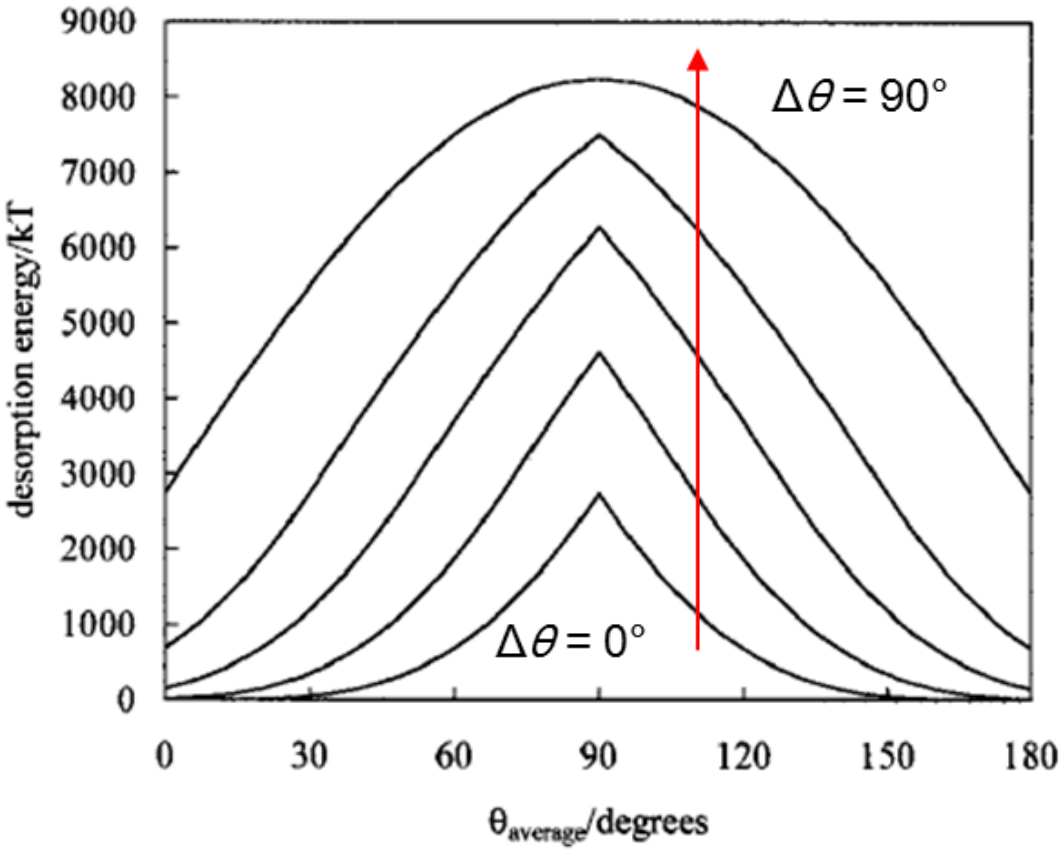

Figure 2.8 Free energy of a Janus particles at hexane – water interface. Parameters used for calculation: α=90°, R=10 nm, γ(OW)=36 mN/m

made snowman-like gold-iron nanoparticles and attached dodecanethiol (DDT) or octadecanethiol (ODT) onto the gold surface to form apolar surface to get the Janus-like surface nature. When they applied these Janus particles, the water – hexane interfacial tension reduction increased compared to that with homogeneous iron oxide or gold nanoparticles (Figure 2.9). This study

presented the effectiveness of amphiphilic Janus nanoparticles as effective emulsifiers.

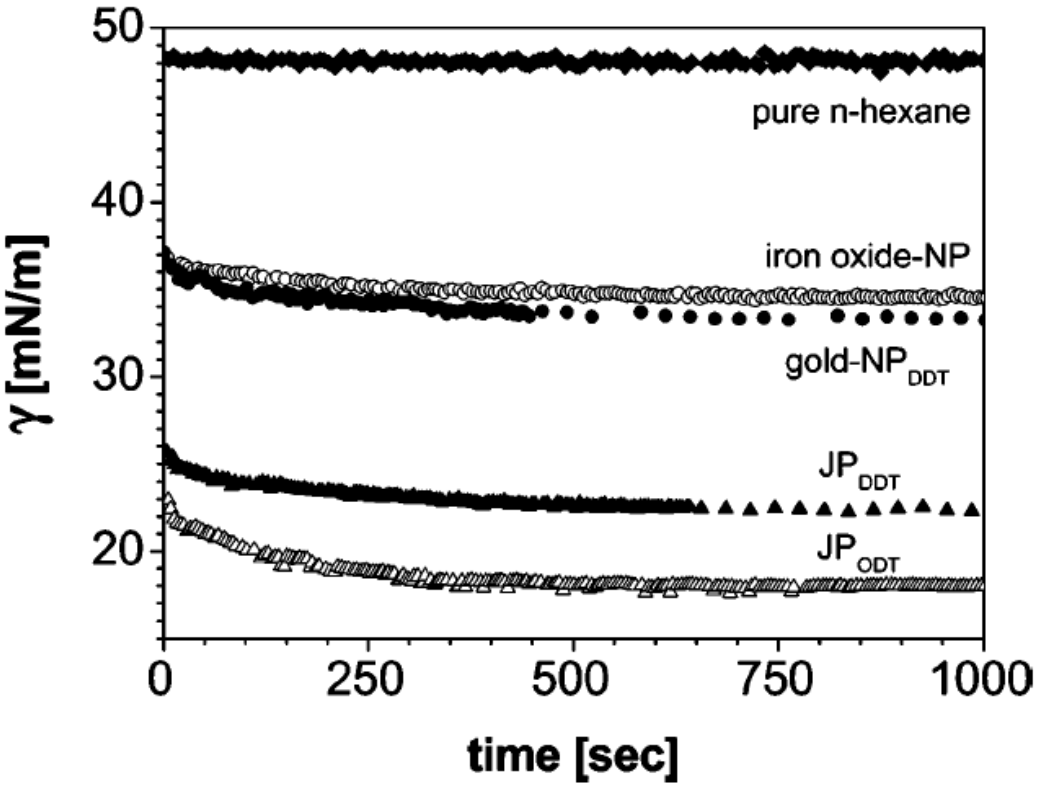

Figure 2.9 Dynamic water-hexane interfacial tension with inorganic particles as emulsion stabilizer.[36]

2.4. Polymer brushes

2.4.1 Polymer brushes

"Polymer brush", which is also known as "tethered polymer chain", is widely used term indicating polymer chains grafted to a supporting surface. Since one end of the polymer brush is immobilized by connecting to the supporting surface and grafted polymer brushes possibly cause overlap

between adjacent chains, their conformational behavior is different from that of untethered free polymer chains.

The structure of polymer brushes can be evaluated by the distance between grafting point (D) and the height of the grafted polymers (h). As the height of grafted polymers approaches the distance between grafting points, they start to overlap. This is a transition point of the polymer brushes from "mushroom" regime to "brush" regime. To characterize this point quantitatively, the reduced tethered density (Σ) can be used as

$$\Sigma = \sigma\pi R_g^2, \qquad \text{(Eq. 2.18)}$$

where, σ is grafting density and Rg is radius of gyration of the polymer. Σ physically means the number of chains occupying an area where a free non-overlapped polymer chains would normally fill under same conditions. Generally, the "mushroom" regime occurs when Σ is less than 1, the crossover regime occurs when Σ is about 1, and "brush" regime occurs when Σ is larger than 1.[37]

Covalently grafted polymer brushes can be formed by "grafting-from" and "grafting-to" techniques. The "grafting-to" technique can be performed by chemical reaction between pre-synthesized polymer chains and functional groups on the supporting surface. The "grafting-from" technique can be performed by *in situ* polymerization of the chains from initiated functionalized supporting surface. In spite of comparatively simple process of

"grafting-to" technique, "grafting-from" is also broadly used due to its capacity to achieve the high grafting density.

2.4.2 Emulsion stabilizing effect of polymer brushes

Introduction of polymers, covalently grafted or physically adsorbed, on the particle surface, also improve the emulsion stabilizing ability of the particles.[38,39] The polymers provide dilatational modulus to the particles and help to prevent the demulsification induced by Ostwald ripening, which is a process whereby larger droplets grow at the expense of smaller ones because the solubility of a component in a droplet increases as the interfacial curvature increases.[40] It is known that if following condition is satisfied, Ostwald ripening is unfavorable.

$$E = \frac{d\gamma}{d \ln A} \geq \frac{\gamma}{2}, \qquad \text{(Eq. 2.12)}$$

where, E is surface dilatational modulus, γ is interfacial tension, A is a surface area of an oil droplet.[41] In addition, particles with amphiphilic block copolymer brushes can behave like Janus particles at the fluids interface. Simulation studies of a particle with block copolymer brushes situated at the fluids interface showed that the Janus-like arrangement of the brushes due to different hydrophilicities of copolymer blocks (Figure 2.10).[42,43] Therefore, the advantage of the Janus surface nature can be taken simply by grafting amphiphilic block copolymer brushes on the nanoparticles without challenging synthesis steps for Janus particles.

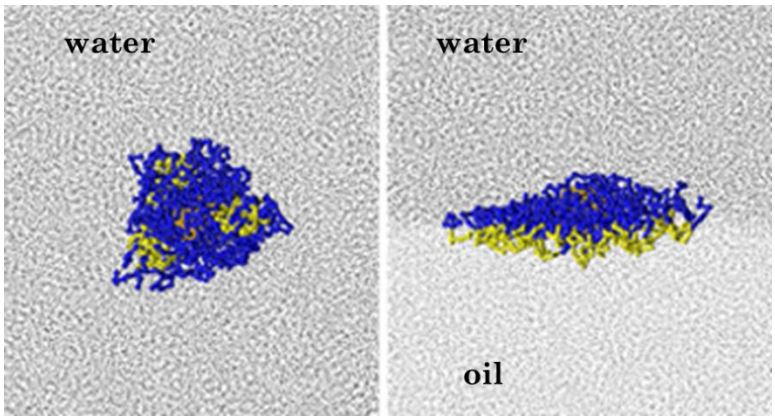

Figure 2.10 Block copolymer grafted silver nanoparticles dispersed in water (left) and situated at oil – water interface (right). Blue: hydrophilic components; Yellow: hydrophobic components.[42]

2.4.3 Previous works about effect of polymers on emulsion stabilization

There have been many efforts to improve the interfacial activity and emulsification efficiency of the small particles by introducing covalently grafted or physically adsorbed polymer chains. Foster *et al.* reported significantly improved emulsification efficiency of the polymer grafted iron oxide nanoparticle clusters. They grafted hydrophilic POEOMA polymer brushes onto iron oxide nanoparticles using a free radical aqueous polymerization method which have several benefits including readily accessible initiators, a reduction in the number of synthetic steps, the lack of a need for catalysts, and the flexibility of utilizing aqueous soluble monomers to produce a wide range of hybrid amphiphilic particles for stabilizing emulsions and dispersions. They achieved relatively high polymer content (~89 wt%) using this "grafting-from" polymerization method. Interestingly

the polymer grafted iron oxide nanoparticles presented a critical particle concentration of 0.003 w/v%, which is a very low value compared to a critical micelle concentration of 0.1 w/v % for the free untethered polymer with same molecular weight. They suggested the reason of this low critical particle concentration of polymer grafted nanoparticles that (1) the high adsorption energy given the large particle size, (2) the high local polymer concentration delivered to the interface by the particles, (3) the ability of the hybrid particles cores to conform to the interface, and (4) the ability of the segments of the very high molecular weight conformable polymer on the deformable iron oxide cores to interact with water and oil to lower interfacial tension (figure 2.11).

Moreover, they reported that the grafting polymer brushes onto the iron oxide cluster also changes the rheological properties, which then had a large influence on the stability of oil – water emulsions. For the hybrid particles, the viscosity in deionized water and synthetic seawater was much larger at all shear rates compared to free polymers dissolved in those solvents, indicating strong interparticle interactions. They conjectured that the emulsion destabilization by coalescence can be prevented by the large viscosity of the hybrid particles in the continuous aqueous phase and the physical barrier provided by the irreversibly adsorbed particles.[39]

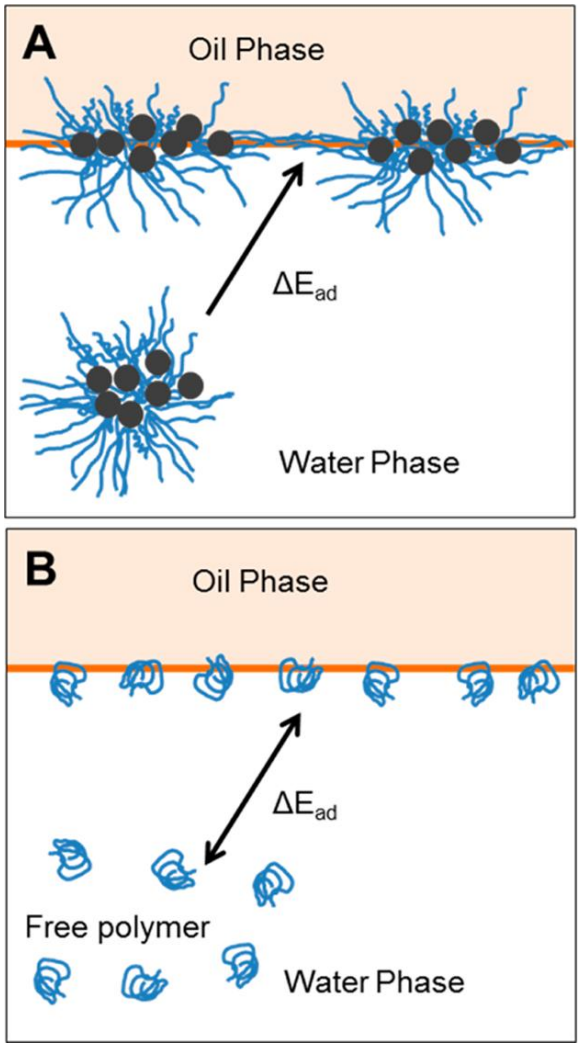

Figure 2.11 a) irreversible adsorption of polymer grafted iron oxide clusters and b) spontaneous adsorption and desorption of free untethered polymers

Yoon *et al*. reported a low dodecane – water interfacial tension with amphiphilic polymer – iron oxide nanoparticles complex. They synthesized a series of sub-100 nm superparamagnetic iron oxide nanoclusters stabilized by amphiphilic PAA-*b*-PBA or PAA-*co*-PBA copolymers. With only 0.27 wt% of these nanoclusters, dodecane-water interfacial tension reduced up to 27.6

mN/m. They reported that thin copolymer shells adsorbed on iron oxide particle surface played an important role in the reduction of the oil – water interfacial tension. Moreover, stable oil – water emulsions were formed by the nanoclusters with 12.1 µm droplet diameter in spite of their low concentrations (0.27 wt %). They also investigated the pH sensitivity of the nanoclusters on emulsion stability. The block copolymer coatings effectively stabilized emulsions over a broad range of pH values (pH = 6–10), while the random copolymer coatings were effective at pH = 8. They estimated the adsorption of the nanoclusters at the oil - water interface from the concentration of nanoclusters in the excess phase and the interfacial surface area calculated using microscopy images. Since the surface coverage of the nanoclusters was below that of a monolayer, they concluded the oil droplets were stabilized by a bilayer patch of nanoparticles.[38]

Saleh *et al*. synthesized water soluble poly(styrene sulfonate) (PSS) grafted silica nanoparticles and reported reduction in the interfacial tension between trichloroethylene and water from 30 mN/m to 14.5 mN/m at an extremely low concentration of nanoparticle (5 mg/ml). The trichloroethylene – water emulsions made by the PSS grafted silica nanoparticles was stable more than 6 months. They reported the PSS grafted silica nanoparticles were stable and well dispersed in water and there was no flocculation. Since the PSS vinyl backbone has the hydrophobic nature and they also have the hydrophilic nature induced by surface charge, the PSS grafted silica

nanoparticles showed amphilphilic surface nature resulting in their great interfacial activity.[44]

Isa *et al*. grafted hydrophilic poly(ethylene glycol) PEG brushes onto iron oxide nanoparticles and studied the structure of the nanoparticle monolayer at the oil – water interface. They reported that the architecture of the stabilizing shell controls the adsorption behavior of nanoparticles at liquid interfaces. Also, the separation between nanoparticle cores at their saturated state at the oil – water interface, was much larger than the size of the hydrated polymer shell in bulk. This cannot be explained by electrostatic repulsion stemming from a residual charge at the core surface due to the screening of the thick polymer shells and the highly hydrophilic nature of the nanoparticles. This implies that saturation is achieved with low nanoparticle core content at the interface and that most of the space is filled by the polymer shells. Therefore strong deformation and flattening of the polymer shells at the interface is required at this state (Figure 2.12). The resulting observed inter-particle distance is supported by a simple model for a two-dimensional polymer brush confined within the interface.[45]

van Rijn *et al*. reduced the perfluorodecalin – water interfacial tension from ~50 mN/m to 20.5 mN/m using PNIPAAm grafted ferritin and studied its dynamics. They compared the interfacial activity of PMIPAAm grafted ferritin particles to the individual PMIPAAm free polymers and bare ferritins. The lower saturated oil – water interfacial was achieved by PNIPAAm

grafted nanoparticles as well as faster interfacial tension reduction rate compared those with single components, PMIPAAm free polymer and bare ferritins. Moreover, iy was found that a single PNIPAAm grafted ferritin covers about 283 nm^2 of interface, which is significantly more than the ferritin and PNIPAAm (0.08 ± 0.01 nm^2/particle and 0.54 ± 0.1 nm^2/chain, respectively). The interfacial activity is mainly attributed to the PNIPAAm polymer component, since the PNIPAAm free polymer also displays high interfacial activity.[46]

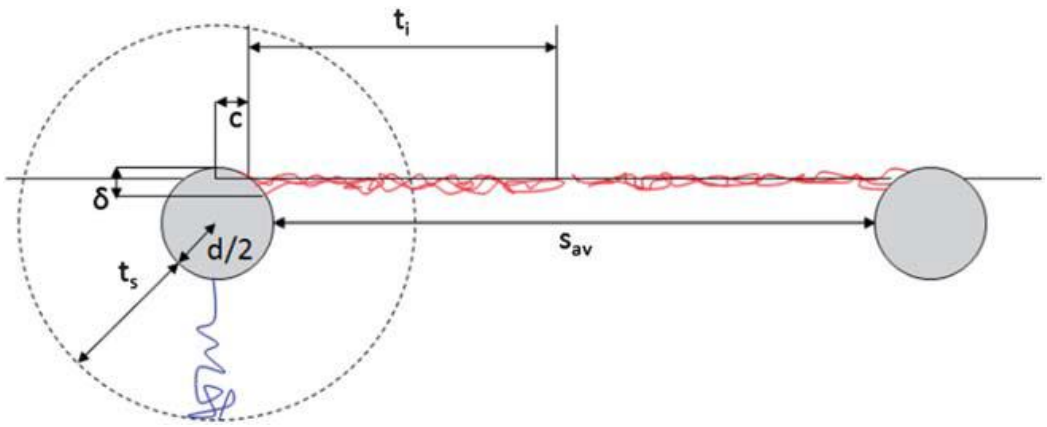

Figure 2.12 Conformation of polymer brushes grafted onto nanoparticles arranged at oil – water interface.

Saigal *et al*. investigated the effect of polymer grafting density of the hybrid particles on their interfacial activity. PDMAEMA brushes were grafted from 20 nm diameter silica nanoparticles. The hybrid nanoparticles form very stable xylene – water emulsions at extremely low particle concentrations. Particles with lower grafting densities were the most efficient emulsifiers due to the conformational freedom of the polymer brushes (Figure

2.13). Stable emulsions were formed with about 0.05 wt% of the low grafting density particles (0.077 chains/nm^2).

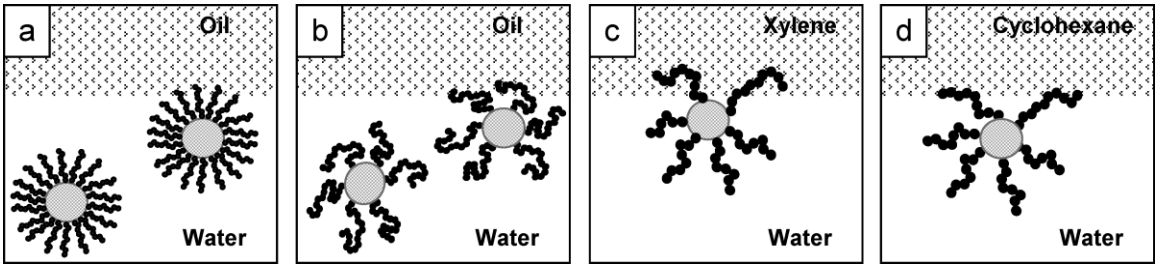

Figure 2.13 Interfacial behavior of polymer grafted nanoparticles with different grafting densities. a) high, b) low grafting density, and c) good, d) bad solvent oil phase

A poor solvent for PDMAEMA such as cyclohexane, could be emulsified under limited conditions of temperature, pH, and ionic strength compared to xylene, a good solvent for PDMAEMA. Moreover, they reported that the oil – water emulsions were thermally responsive, and demulsified rapidly by increasing the temperature above the critical flocculation temperature.[47]

2.5. Atom transfer radical polymerization

2.5.1. Controlled radical polymerization

Controlled radical polymerization (CRP), which is also called as living radical polymerization, is the method to synthesize comparatively well controlled polymers. The controllability of the polymerization method comes from suppressed termination reactions between radicals and its distribution

can be relatively narrow (M_w/M_n<1.1). Since the molecular weight of the polymers is linearly proportional to the reaction time, it is possible to control the molecular weight of the polymer easily. By using the propagation ends which are still active even after the termination of the reaction, making diverse architectures or compositions such as star polymers and block copolymers is possible.

There have been mainly three types of CRP methods so far. For atom transfer radical polymerization (ATRP), the transition metal halide catalysts are used for reversible deactivation of propagating radical to form dormant species. Reversible addition-fragmentation chain transfer (RAFT) is done by degeneration of the transfer between propagating radical using reversible chain transfer agent. For the stable free radical polymerization (SFRP), which is another important CRP method, the radical can be stable and does not initiate polymerization by being embedded in the (2,2,6,6-tetramethylpiperidinyloxy) "TEMPO" group.[48,49]

2.5.2. Principles of atom transfer radical polymerization

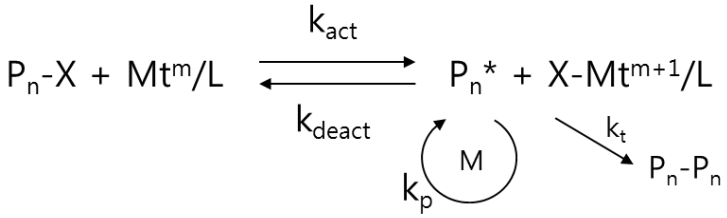

Scheme 2.1 ATRP equilibrium

ATRP is conducted by three main elements, which are initiators, metal halide catalysts, and ligands. The alkyl halide initiator or macromolecular dormant species are activated by the transition metal-ligand complexes. This activation process produces growing radicals (P_n^*) and transition metal complexes in higher oxidation state which act as deactivators. Although radicals are produced and activated, they are deactivated again immediately due to the low equilibrium constant ($K_{ATRP} = k_{act}/k_{deact}$). Therefore, only small number of growing radicals remains activated and termination reactions can be suppressed.

The reaction rate of ATRP can be expressed as

$$R_p = k_p[M][P_n^*] = k_p K_{ATRP}\left(\frac{[P_nX][Cu^I/L][M]}{[X-Cu^{II}/L]}\right), \qquad \text{(Eq. 2.13)}$$

where, k_p is the propagating rate constant and K_{ATRP} is the catalytic activation-deactivation equilibrium constant. Reaction rate depends on the concentration of initiator, transition metal-ligand complex, and monomer.[49]

2.6 Transport of nanoparticles in porous media

2.6.1 Porous media

Porous media are materials containing pores in their body and usually characterized by their porosity and permeability. Most conventional oil reservoirs are porous media where the oil and gas are saturated in their pores in high temperature and pressure. In this study, carbonate and sandstone rocks, which are major components of petroleum reservoirs, were

used for lab-scale transport experiments. Sandstones are predominantly composed of silica minerals which are negatively charged at neutral pH.[50] The carbonates are positively charged because they are rich in calcium and magnesium ions.[51]

2.6.2 One – dimensional convection – dispersion equation

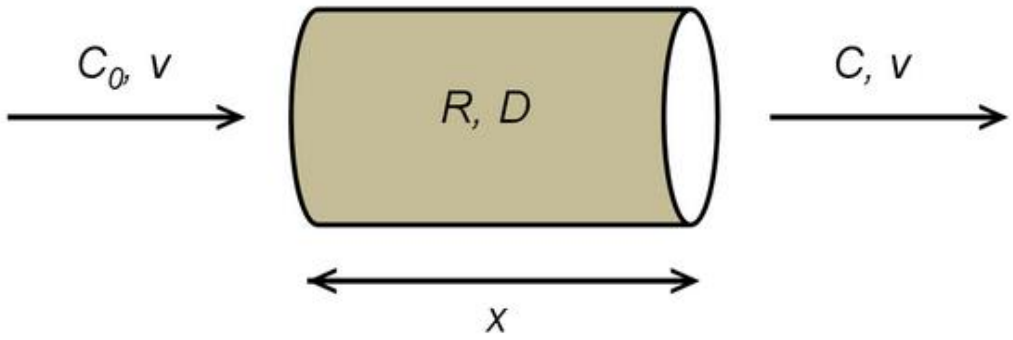

Figure 2.14 Parameters to model the behavior of nanoparticles transporting through porous media

Considering the interaction with the rock cores, nanoparticle transport through the finite porous media can be expressed with one dimensional convection-dispersion equation

$$\mathrm{R}\frac{\partial C}{\partial t} = D\frac{\partial^2 C}{\partial x^2} - v\frac{\partial C}{\partial x} - k_d C, \qquad \text{(Eq. 2.14)}$$

where, C is the concentration of the nanoparticles, x is the distance from the inlet of the injection, t is the time, D is the dispersion coefficient, v is the pore velocity, R is retardation factor and k_d is the first order removal constant. R and k_d are written as

$$R = 1 + \frac{\rho_b K_d}{\phi} \text{ and} \qquad \text{(Eq. 2.15)}$$

$$k_d = -\frac{u}{L}\ln\left(\frac{C_e}{C_0}\right), \qquad \text{(Eq. 2.16)}$$

where, ρ_b is the bulk density of the rock core, K_d is the partition coefficient, ϕ is the porosity of the rock core, u is the pore velocity of the fluid, C_0 is the influent concentration of the nanoparticles, and C_e is the steady state effluent concentration of the nanoparticles.[52]

The initial condition used is

$$C(x,t) = 0\,; t = 0, x \geq 0.$$

The boundary conditions used are

$$C(x,t) = C_0\,; x = 0, t > 0 \text{ and}$$

$$\frac{\partial C(x,t)}{\partial x} = 0\,; x \to \infty, t \geq 0.$$

From these initial and boundary conditions, the analytical solution of the one dimensional convection-dispersion equation was derived by Kumar *et al* as

$$\frac{C}{C_0} = \frac{1}{2}\exp\left[\frac{\left(u-\sqrt{u^2+4k_dD}\right)x}{2D}\right]\text{erfc}\left[\frac{Rx-\left(\sqrt{u^2+4k_dD}\right)T}{2\sqrt{DRT}}\right]$$

$$+\frac{1}{2}\exp\left[\frac{\left(u+\sqrt{u^2+4k_dD}\right)x}{2D}\right]\text{erfc}\left[\frac{Rx+\left(\sqrt{u^2+4k_dD}\right)T}{2\sqrt{DRT}}\right].^{53} \qquad \text{(Eq. 2.17)}$$

Based on the nanoparticle breakthrough curves from the core flooding experiments and the one dimensional convection – dispersion equation, transport parameters were estimated.

Chapter 3 Experimental methods

3.1 Preparation of polymer-grafted nanoparticles

3.1.1 Synthesis of 1-chlorodimethylsilyl propyl 2-bromo-2-methylpropionate.

0.8 g of allyl 2-bromo-2-methylpropionate (3.9 mmol), 6.0 mL of chlorodimethylsilane (79.344 mmol), and 10 mg of Pt_C (10% Pt) catalyst were added to a round-bottom flask. After darkening the surround of the flask, the mixture was purged with nitrogen for 10 min and reacted for 1 h in the oil bath which had been preheated to 40°C. And the mixture was stirred overnight at the room temperature in the air. After the reaction, the platinum catalyst was removed with syringe filter (0.2 μm, PTFE) and the unreacted chlorodimethylsilane was evaporated under low pressure at room temperature.

3.1.2 Synthesis of 2-bromoisobutyrate initiator functional silica nanoparticles.

Various amounts (1.67 and 10 g) of 1-chlorodimethylsilyl propyl 2-bromo-2-methylpropionate were added to the silica dispersion (50g, 30wt% in MIBK) and this mixture was refluxed overnight at 80°C. After cooling to room temperature, hexamethyldisilazane (HMDS) (6.0 mL, 28 mmol) was introduced and stirred for 3 h at room temperature. A white powder was formed by another reflux for 2 h at 40°C. The powder was separated by centrifugation, and the clear orange supernatant was added in dropwise fashion into methanol to precipitate colloids. The precipitate was dissolved with 50 mL of THF and precipitated again into *n*-hexanes (500 mL). After a

couple of hours, nanoparticles were recovered by centrifugation and dried under vacuum overnight at room temperature.

3.1.3 Synthesis of SiO_2-POEOMA hybrid nanoparticles by surface initiated ATRP

CuBr (12 mg, 0.08 mmol) and Cu(II)Br (1.1 mg, 0.005 mmol) were placed in a round bottom flask. N,N,N′,N″,N″-Pentamethyldiethylenetriamine (10 μl, 0.05 mmol), monomer (20 g, 66.7 mmol), anisole (20 g) and SiO_2 initiator synthesized earlier as described previously (0.2 g, 0.04 mmol) were added to another round bottom flask. After sealed with rubber septum, both flasks were purged with nitrogen gas under stirring for an hour. The solution in the second flask was transferred to another flask by cannula needle using the nitrogen pressure. The reaction mixture was stirred for 5 minute and put into the oil bath with 75°C. The polymerization was proceeded for 10~160 minute and terminated by introducing air to the reaction mixture and cooling the flask. The catalysts were removed from the product solution by passing through a column filled with neutral alumina after diluted with THF. The THF was evaporated in the rotary evaporator and remaining solution was precipitated in the cyclohexane. The precipitant was recovered by centrifugation and dried overnight at room temperature in the vacuum.

3.1.4 Synthesis of SiO_2-P(OEOMA-b-sty) hybrid nanoparticles by polystyrene (PS) chain extension

PS chains were grown from POEOMA chain ends using the ATRP method. CuBr (12 mg, 0.08 mmol) were placed in a round bottom flask. N,N,N′,N″,N″-Pentamethyldiethylenetriamine (PMDETA, 16.7 µl, 0.08 mmol), styrene (10.4 g, 125 mmol), anisole (10 g) and SiO_2-POEOMA macroinitiator (0.2 g) were added to another round bottom flask. After sealed with rubber septum, both flasks were purged with nitrogen gas for an hour. The mixture in the second flask was transferred to another flask using cannula needle by nitrogen pressure. The reaction mixture was stirred for 5 minute and put into the oil bath which was preheated to 100°C. The polymerization was conducted for 0.5 - 4 hours and then terminated by introducing air to the mixture and cooling the flask. The reaction mixture was diluted with THF, and copper catalysts were removed by passing through a column filled with neutral alumina. The THF was evaporated in the rotary evaporator and remaining solution was precipitated in methanol. The precipitants were recovered by centrifugation and dried overnight at 80°C under the vacuum.

3.2 Analysis of oil – water emulsions

3.2.1 Pendant drop interfacial tension measurement

Interfacial tension of hybrid nanoparticles-dissolved water and hexane was measured by pendent drop method. In order to get reasonable interfacial tension values, *n*-hexane (ACS grade, 98.5%) and toluene (ACS grade, 99.5%) were purified by column chromatography three times with basic alumina as stationary phase. Purified hexane was filled in a quartz cuvette and used as an atmospheric phase. A 6~7 μl of water droplet was injected into the hexane atmosphere. The picture of the droplet was taken by time period with the optical contact angle measuring instrument (OCA 15EC, DataPhysics) and processed using software to get the diameter and shape factor by counting the pixels of the picture (Figure 3.1). From measured parameters and densities of water and hexane, water-hexane interfacial tensions were calculated. Figure 3.2 indicates the empirical formula to calculate interfacial tension from the pendent drop experiment.[54] For every measurement, the interfacial tension was regularly monitored to confirm the saturated minimum value.

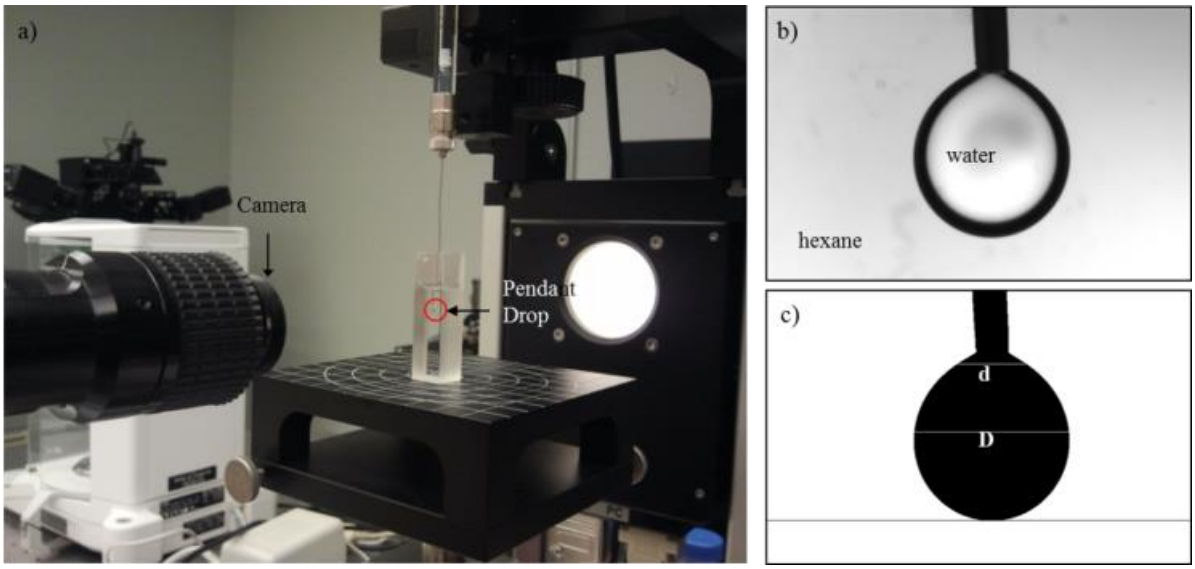

Figure 3.1 a) Equipment for the interfacial tension measurement, b) a picture of the pendant drop, c) a picture converted by the Matlab

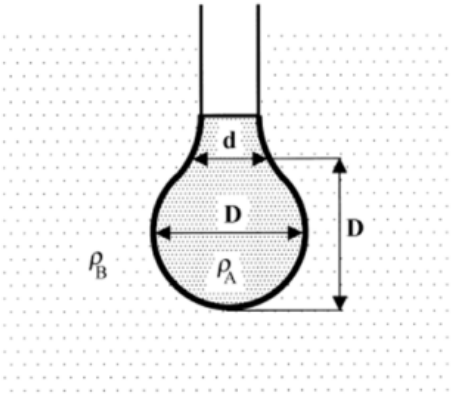

$$\gamma = \frac{\Delta\rho g D^2}{H}$$

$$\frac{1}{H} = \frac{B_4}{S^A} + B_3 S^3 - B_2 S^2 + B_1 S - B_0$$

Figure 3.2 Empirical equation for the pendent drop method. The shape parameter S is calculated from the ratio of D and d.

Table 3.1 Empirical constants for pendant drop measurement

Range of S	α	B_4	B_3	B_2	B_1	B_0
0.40-0.46	2.56651	0.32720	0	0.97553	0.84059	0.18069
0.46-0.59	5.59725	0.31968	0	0.46898	0.50059	0.13261
0.59-0.68	2.62435	0.31522	0	0.11714	0.15756	0.05285
0.68-0.90	2.64267	0.31345	0	0.09155	0.14701	0.05877
0.90-1.00	2.84636	0.30715	-0.69116	-1.08315	-0.18341	0.20970

3.2.2 Axisymmetric drop shape analysis – profile (ADSA-P)

Hexane – water interfacial tensions were estimated with ADSA-P software. The software processed images of aqueous pendant droplet in hexane atmosphere (Figure 3.3) and estimated interfacial tensions. Estimated interfacial tensions were 48.0 mN/m and 17.9 mN/m for pure water and hybrid nanoparticle aqueous solution respectively. These values were not very different from the interfacial tensions calculated by empirical equation (50.9 mN/m and 16.7 mN/m). Density of water, density of hexane, and the size of a pixel used were 0.997 g/cm^3, 0.655 g/cm^3, and 0.0008333 cm/pixel respectively.

Figure 3.3 Pictures of pendant drop of a) pure water and b) hybrid nanoparticle (M_w = 208 kDa, = 0.1 chain/nm^2; 1000 ppm) aqueous solution in hexane atmosphere.

3.3 Analysis of nanoparticle transport behaviors

3.3.1 Characterization of carbon nanoparticles

Negatively charged carbon nanoparticles were synthesized by the citrate chemistry.[55] Surface charges of the carbon nanoparticles were measured with Zetasizer Nano (Malvern). 2 wt% of 5 nm carbon nanoparticles and 0.1 wt% of 50 nm carbon nanoparticles in deionized water were prepared separately and their zeta potentials were measured. The high concentration nanoparticle dispersions were used for sufficient particle count and signal intensity for the measurements. The diameters of the carbon nanoparticles (5 nm and 50 nm in diameters) were measured by transmission electron microscopy (TEM). The concentration of the carbon nanoparticles in artificial sea water solution was estimated using UV-vis spectroscopy. The absorbance peak intensities at then wavelengths of 346 nm and 252 nm were measured for 5 nm and 50 nm carbon nanoparticles respectively. Then the concentrations of the

carbon nanoparticles in effluent solutions were estimated based on the peak intensity of calibration samples. The adsorption of the carbon nanoparticles on rock surface was visually observed by fluorescence microscopy from the several sections of rock cores.

3.3.2 Core flooding experiments

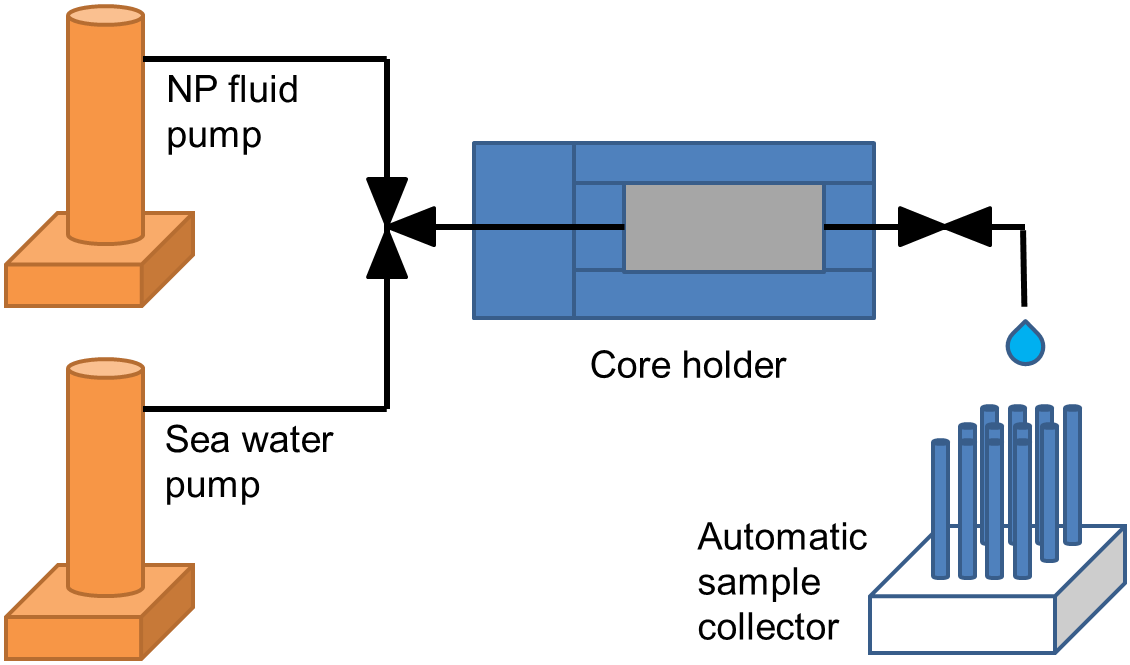

Figure 3.4 Brief description of core flooding setup.

Lab-scale reservoir tracking experiments were conducted by core flooding set up as described in Figure 3.4. Synthetic sea water and nanoparticle aqueous solutions were injected into the rock core which was held by tri-axial core holder to investigate the transport behavior of nanoparticles. Concentrations of nanoparticles in effluent samples, collected by automatic sample collector, were estimated by adsorption peak analysis of

UV-vis spectroscopy measurements. Pressure across the core was recorded during the experiments and the temperature of the core was controlled by placing the entire equipment in the oven.

Chapter 4 Hydrophilic homopolymer grafted silica nanoparticles as oil dispersants

4.1 Introduction

The development of highly effective oil dispersants that are less toxic has become increasingly important in order to minimize their environmental impact.[13,15,17,18,56-61] One of the alternatives is the use of colloidal particles and nanoparticles, whose toxicity and potential environmental impact might be relatively low. Significant efforts have been focused on understanding the interfacial activity of nanoparticles at fluid – fluid interfaces,[21,62] with several recent studies describing the interfacial behavior of polymer decorated nanoparticles at polymer – polymer interfaces.[39,63-66] Nevertheless, the molecular parameters controlling the interfacial activities of polymer grafted nanoparticles at the interface of two simple liquids remain uncertain.

The interfacial activity of oil – water systems stabilized using particles is best understood through a thermodynamic analysis. The change in free energy of a system where a particle 'p' is placed at the interface of two immiscible fluids '1' and '2' can be expressed as

$$F_{int} = \left(\gamma_{12}A_{12} + \gamma_{p1}A_{p1} + \gamma_{p2}A_{p2} + \tau L - \gamma_{12}A_{st}\right) - \gamma_{12}A_{12} - \gamma_{p1}A_{p}, \qquad \text{(Eq. 4.1)}$$

where, A_{ij} and γ_{ij} refer to the contact area and the interfacial tension between species i and j, L is the length of the three phase contact line, and τ represent the line tension. A_{st} is the contact area removed by nanoparticles from the

original interface between two fluids. This can be simplified using the relation, $A_p=A_{p1}+A_{p2}$, and expressed as

$$F_{int} = (\gamma_{p2} - \gamma_{p1})A_{p2} - \gamma_{12}A_{st} + \tau L. \quad \text{(Eq. 4.2)}$$

For a spherical particle, equation (2) can be simplified using Young's equation to

$$F_{int} = -\pi R^2 \gamma_{12}(\cos\theta - 1)^2, \quad \text{(Eq. 4.3)}$$

where, R is the radius of the particle and θ is the contact angle of a fluid on the particle surface.[34] Therefore, particles can reduce the interfacial tension between two immiscible fluids by segregating to the interface. Such particle-stabilized colloidal systems are termed "Pickering emulsions".[33,34] Well designed Pickering emulsions, with colloidal particles with tuned contact angle properties, exhibit high stability due to the large adsorption energy of the particles at the interface.[67]

However, most bare inorganic particles do not lower the interfacial free energy significantly as they are not sufficiently surface-active.[36,68,69] Consequently, several studies have been undertaken to improve the interfacial activity of inorganic particles as well as stabilize emulsions of oil and water.[35,36,70,71] In combination with polymers inorganic particles have been used to make the particles more surface-active. Saleh *et al.* synthesized poly(styrene sulfonate) grafted silica nanoparticles and reported reduction in the interfacial tension between trichloroethylene and water from 30 mN/m to 14.5 mN/m at a concentration of nanoparticle of 5 mg/ml.[44] Yoon *et al.*

recently reported a low dodecane – water interfacial tension with 0.27 wt% amphiphilic polymer – iron oxide nanoparticles complex.[38] Rijn *et al*. reduced the perfluorodecalin – water interfacial tension from ~50 mN/m to 20.5 mN/m using PNIPAAm grafted ferritin and studied its dynamics.[46] Isa *et al*. grafted PEG brushes onto iron oxide nanoparticles and studied the structure of the nanoparticle monolayer at the oil – water interface.[45] However, most studies required nanoparticle concentrations of more than several hundred ppm to achieve the maximum interfacial tension reduction. Moreover, a few studies have been reported concerning the effect of molecular weight and grafting density of these grafted polymer chains on the nanoparticle's interfacial activity at the interface of simple liquids.[41,72]

In this chapter, we report on the interfacial activity of silica nanoparticles grafted with a hydrophilic poly(oligo(ethylene oxide) monomethyl ether methacrylate) (POEOMA) at the interface of oil and water. Recent reports of Johnston and coworkers demonstrate the efficacy of POEOMA grafted iron oxide nanoparticles to reduce the interefacial tension in comparison to the free polymer.[16] We utilize a chemically similar polymer, and vary the molecular weight and grafting density of the polymer on silica, to examine the effect of the grafted polymer's nature on the interfacial behavior and thereby clarify the key molecular parameters and provide further insight into the variation of critical particle concentration on the physical properties of the hybrid nanoparticles.

4.2 Methodology

4.2.1 Materials

Colloidal silica nanoparticles (MIBK-ST, effective diameter ~15.5 ± 0.9 nm (from dynamic light scattering and small angle x-ray scattering[73]), 30~31 wt% silica in methyl isobutyl ketone) were acquired from Nissan Chemical. Allyl 2-bromo-2-methylpropionate (98%, Sigma-Aldrich), chlorodimethylsilane (98%, Sigma-Aldrich), 5% platinum on activated charcoal (Sigma-Aldrich), Hexamethyldisilazane (HMDS, 99.9%, Sigma-Aldrich), tetrahydrofuran (THF, 99.9+%, Sigma-Aldrich), copper(I) bromide (98%, Sigma-Aldrich), copper(II) bromide (99%, Sigma-Aldrich), anisole (anhydrous, 99.7%, Sigma-Aldrich), N,N,N′,N″,N″-Pentamethyldiethylenetriamine (PMDETA, 99%, Sigma-Aldrich), 4,4'-dinonyl-2,2'-dipyridyl (dNbpy, 97%, Sigma-Aldrich) methanol (99.8%, Mallinckrodt), hydrofluoric acid (48~51%, VWR), magnesium sulfate (97+%, Sigma-Aldrich), and squalene (98+%, Sigma-Aldrich) were used as received. *n*-Hexane (98.5%, Macron), used for the interfacial tension measurements, was purified by passing through a basic alumina column three times. Oligo(ethylene oxide) monomethyl ether methacrylate (OEOMA, M_n=300, Sigma-Aldrich) was passed through the column which was packed with inhibitor remover (for monomethyl ether hydroquinone, Sigma-Aldrich) and neutral alumina (Sigma-Aldrich) to remove inhibitors.

4.2.2 Preparation of polymer-grafted nanoparticles

Silica nanoparticles were grafted with POEOMA by surface-initiated atom transfer radical polymerization (ATRP) using anisole as a solvent, PMDETA as a ligand, CuBr and Cu(II)Br as catalysts at 75°C for 15-160 min (Scheme 4.1), following the protocol published previously.[74] Reaction

mixtures were diluted with THF and passed through a column packed with neutral alumina to remove the catalysts after the polymerization to eliminate any residual copper catalyst (Supporting Information). Dried samples were dispersed in THF and then *n*-hexane was added to the solution until it became cloudy. After heating at 50°C and making the solution clear again, it was allowed to settle in a separatory funnel overnight. The cloudy phase, which did not contain the untethered polymer chains, was taken and re-precipitated in *n*-hexane.

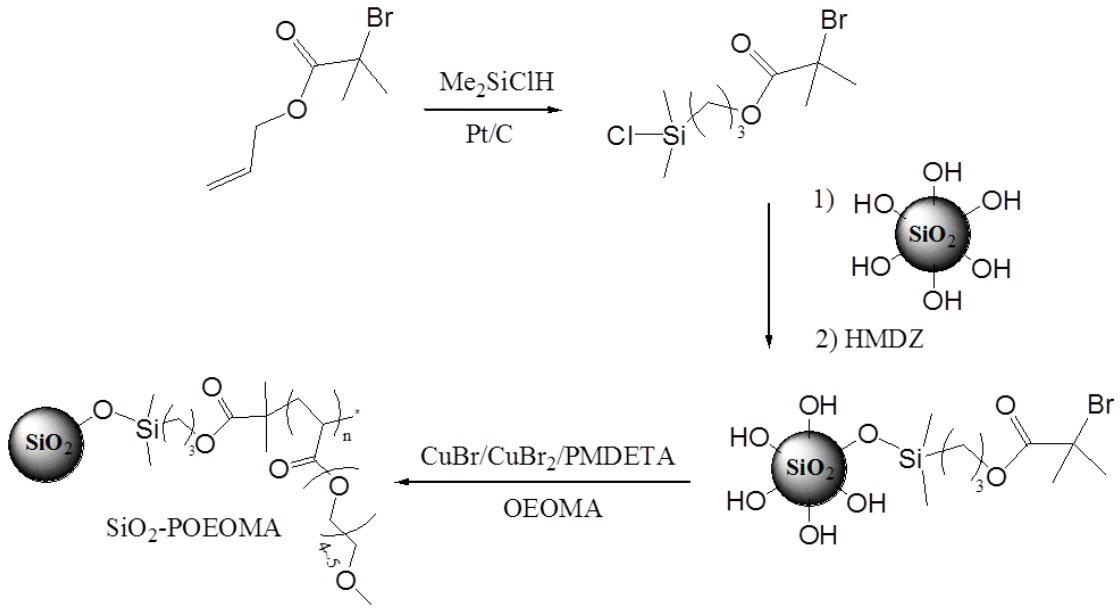

Scheme 4.1 General scheme for synthesis of initiator attached silica nanoparticles and surface initiated ATRP of POEOMA.

Table 4.1 ATRP of POEOMA from initiator-grafted silica nanoparticles

Sample	Reaction Time	M_w (kDa)	M_w/M_n	Grafting density (chains/nm^2)	Number of polymer chains per particle	d[1)] (nm)	D[2)] (nm)
a	15 min	423	1.1	0.021 ±0.001	16±1	23±1	78±1
b	160 min	505	1.4	0.034 ±0.002	25±3	36±3	97±2
c	15 min	108	1.4	0.126 ±0.006	95±9	33±2	87±2
d	35 min	370	2.5	0.143 ±0.007	108±10	45±3	118±3
e	60 min	794	2.1	0.133 ±0.007	100±10	55±5	168±4
f[3)]	21 hours	208	1.6	0.100 ±0.005	76±7	44±3	77±2

1) Center-to-center distance of silica nanoparticles measured by SAXS in bulk melt state of the polymer
2) Hydrodynamic size of dispersed hybrid nanoparticles measured by DLS in water
3) The reaction was done with 4,4'-dinonyl-2,2'-dipyridyl (dNbpy) as a ligand and THF as a solvent for 21 hours

4.2.3 Thermal gravimetric analysis (TGA)

Polymer content in hybrid nanoparticles was measured by thermal gravimetric analysis (TGA Q500, TA instrument). The measurement was performed under argon atmosphere from 25 °C to 800 °C at a heating rate of 10 °C/min. Effective weight losses of the hybrid nanoparticles during the

heating process were obtained by the measurement and used towards the calculation of the grafting density.

4.2.4 Size exclusion chromatography (SEC)

The molecular weight and molecular weight distribution of the grafted polymers were determined by size exclusion chromatography (Viscotek 270 triple detection system). Since the polymers were covalently attached to the silica nanoparticles, they were cleaved from the silica by the following process.[74] The hybrid particles were first dissolved in 4 ml of THF then 2 ml of 49% HF were added. After stirring the solution overnight, it was neutralized using saturated aqueous solution of NaOH. The THF layer was collected, and the solvent was removed through rotary evaporation. The transparent, viscous, and gel-like cleaved polymer was recovered. The average molecular weights of cleaved polymer brushes obtained from the SEC were used together with the weight loss data from the TGA measurement in order to calculate the grafting density of the hybrid nanoparticles.

4.2.5 Dynamic light scattering (DLS)

Hydrodynamic diameters of the bare silica nanoparticles and polymer grafted hybrid nanoparticles in a good solvent were measured by dynamic light scattering (Brookhaven Instrument, BI-200SM). Scattering of 1000 ppm aqueous solutions were measured at three different scattering angles (60°, 90°, 120°) using a laser emitting a light with a wavelength of 637.6nm. The fluctuations in the intensity of the scattered light as a function of the delay

time is expressed by an autocorrelation function and mathematically treated as an exponential decay function. The diffusion coefficient of the particle in the solvent can be calculated from the decay rate and based on the calculated diffusion coefficient, hydrodynamic radius is determined through the Stokes-Einstein equation.

4.2.6 Small angle X-ray scattering (SAXS)

The structure of the hybrid nanoparticles and the characterization of the inter-particle distance were obtained by small angle X-ray scattering measurements using a Rigaku SMax3000 with a MicroMax-007HF rotating anode X-ray generator. If hybrid nanoparticles contain regularly ordered structures, constructive interference of X-ray beams results in scattering peaks and the type of crystal structure can be estimated based on the arrangement of those peaks. From the geometry of this crystal structure and the q value of the first scattering peak (q_1^*), the size of the hybrid particles and inter-particle distance were calculated. The structure factor was extracted from the 1-D X-ray scattering plots[75,76], and q_1^* values from the structure factors are reported.

4.2.7 Pendant drop method

The interfacial tension between hexane and water was measured by the standard pendent drop method. Purified *n*-hexane was filled in a quartz cuvette and used as the atmospheric phase. 6~7 μl of water was injected into the *n*-hexane atmosphere using a syringe to make a water pendant drop. The

image of the water droplet (Supporting information), deformed by gravity and interfacial interactions, were taken using the tensiometer (OCA 15EC, DataPhysics), and processed with software to get the equatorial diameter δ, and the diameter δ′ in a selected plane, located a distance equal to δ vertically from the vertex. From these parameters, shape factor (H) and hexane – water interfacial tensions were calculated by the empirical equation[54]

$$\frac{1}{H} = \frac{B_4}{S^A} + B_3S^3 - B_2S^2 + B_1S - B_0 \text{ and} \quad (4)$$

$$\gamma = \frac{\Delta\rho g\delta^2}{H}, \quad (5)$$

where, A, B_0, B_1, B_2, B_3, and B_4 are empirical parameters and S is defined as δ'/δ. For every measurement, the interfacial tension was regularly monitored to confirm the saturated minimum value. We note that we processed selected data sets covering the breadth of interfacial tensions reported in this paper using a direct fitting of the droplet to the Young-Laplace equation based on the drop shape analysis developed by Neumann et al[77] and the resulting values for the interfacial tension were found to be within the errors of the measurement identical to the simpler description used here. This is not surprising considering the near-spherical nature of the droplets considered here and the criterion for the shape factor developed for the applicability of equations 4 and 5 to calculate interfacial tension by Misak [54].

4.3 Results and discussions

Polymers of oligo(ethylene oxide) monomethyl ether methacrylate were grafted from silica nanoparticles using surface initiated ATRP and a set of six materials, described in Table 4.1, were prepared. The average molecular weight and the grafting densities of polymer brushes were changed by varying the reaction time and by varying the ratio of initiator to silica. The weight average molecular weight (M_w) of polymer brushes, measured using SEC, varied from 108 to 794 kDa. The grafting density was calculated based on the method from literature using thermogravimetric analysis, the molecular weight data and the particle size.[78] Thermogravimetric analyses of hybrid nanoparticles made with different reaction time were conducted (Figure 4.1). The volatile portion of the ATRP initiator attached nanoparticles was about 8 wt% and those of hybrid nanoparticles were varied from 79 wt% to 95 wt%. When the grafting densities were fixed with about 0.15 chains/nm^2, weight loss of the hybrid nanoparticles increased with increasing average molecular weight of the polymer brushes. As presented in Figure 4.1b, the inverse of the amount of residue in TGA measurements linearly increased with the average molecular weight of polymer brushes, and this linear proportion indicates the constant grafting densities of three different hybrid nanoparticles. For every TGA measurement, the effective weight loss of the hybrid particles were taken in the temperature range of 200°C to 800°C for the calculation of the grafting densities.

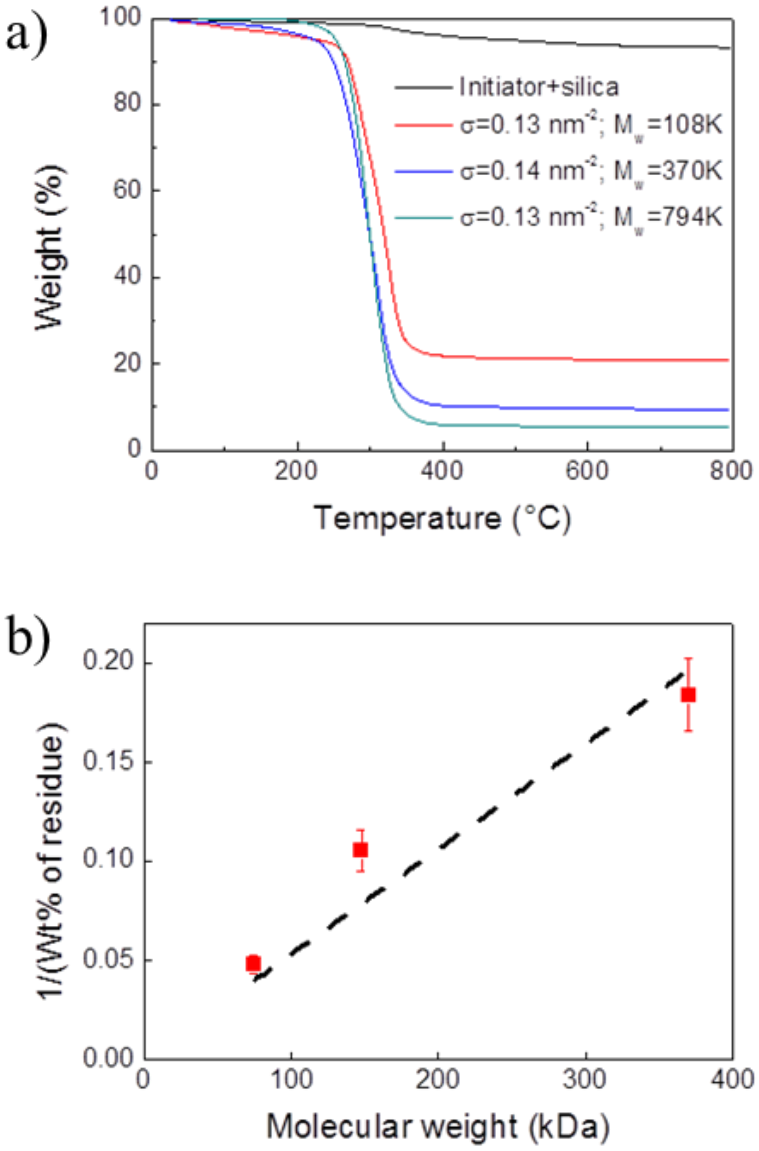

Figure 4.1 a) TGA plots of silica-polymer hybrid nanoparticles b) relationship between reciprocal wt% of residue of TGA and molecular weight. Grafting densities of hybrid nanoparticles were fixed.

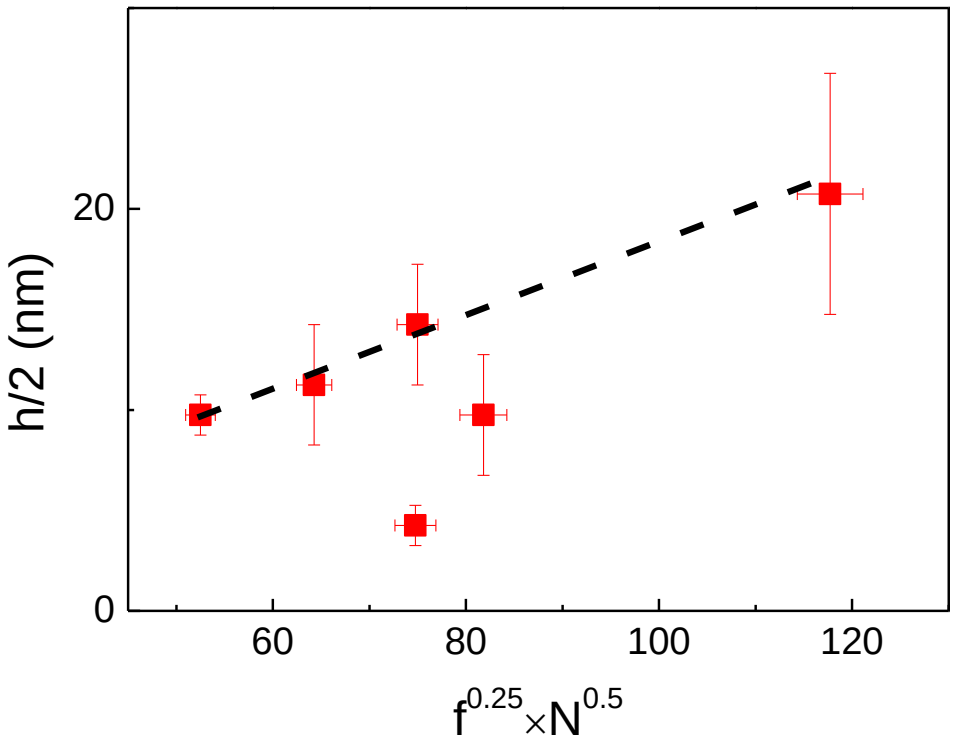

Figure 4.2 Scaling relationship between polymer brush height (h/2) and grafting properties. f and N indicate the number of polymer chains per particles and the degree of polymerization respectively.

The density of the silica nanoparticles was assumed to be 2.65 g/m^3 for the calculation.[79] The diameter of silica core was 15.5 ± 0.9 nm which was obtained by DLS and SAXS measurement of the colloidal bare silica nanoparticles.[73] This uncertainty in the particle size resulted in the calculated grafting densities to not be significantly impacted. The grafting densities of all samples were controlled between 0.02 and 0.14 chains/nm^2.

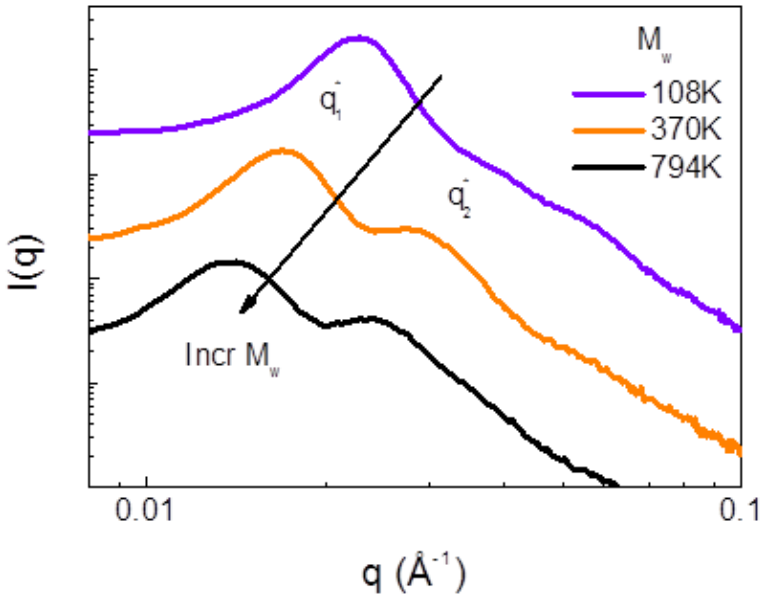

Figure 4.3 Small angle X-ray scattering data for POEOMA-SiO_2 hybrid nanoparticles with varying molecular weight and fixed grafting density of the grafted POEOMA brushes.

The structure of solvent free hybrid nanoparticles was evaluated by small angle X-ray scattering (SAXS) measurements. As shown in Figure 4.3, the scattered intensity of X-rays from the bulk hybrid nanoparticles with 370 kDa and 794 kDa polymer molecular weight presented two clear scattering peaks labeled as q_1^* and q_2^* and a weak third order scattering peak at around $\sqrt{7}q_1^*$. With increasing molecular weight the location of the primary scattering peak (q_1^*) (and the secondary peak at q_2^*) shift to smaller q-values. The values of q_1^* and q_2^* were observed to follow q_1^*: q_2^*:: 1:$\sqrt{3}$. The absence of a peak at $\sqrt{2}q_1^*$ indicates that the structure of the dry hybrid nanoparticles is a face centered cubic (FCC) or random hexagonal close packed (HCP)

ordering. A similar observation regarding the arrangement of polymer – silica hybrid particles with high grafting density was reported by Goel *et al*[73] and by Vlassapoulos *et al*[80] for star polymers with over 100 star arms. We note however that the particles prepared here have on average between *16 and 110 polymer chains per nanoparticle* and certainly not in the high grafting density regime previously explored by Goel *et al*.[73] Perhaps the bulky nature of the repeat unit of the POEOMA causes additional steric hindrance than more flexible repeat units and showed a clear ordered pattern in the SAXS measurement.

From the melt-state scattering data (Figure 4.3), the center-to-center distance, *d*, between hybrid nanoparticles formula was calculated as

$$d = a\left(\frac{2\pi}{q_1^*}\right), \qquad (6)$$

where, *a* is 1.22 for the FCC and HCP lattice. Additionally, the surface-to-surface distance between silica cores, h, was calculated by subtracting the diameter of silica core from d. Although the bulk hybrid nanoparticles with 108 kDa polymer molecular weight present weak secondary X-ray scattering peak, we estimated their size from the lattice parameter of FCC or HCP structures as well.

Data for all six hybrid nanoparticles (d) estimated by SAXS were reported in Table 3.1 and varied from 23 to 55 nm. The mean-field model of Daoud and Cotton[81] suggests that in the "strong-brush regime" the height of the polymer brush (estimated here as $h/2$, where $h = d - d_{NP}$) is proportional

to $f^{1/4}N^{1/2}$, where f and N represent the number of polymer chains per particle and degree of polymerization, respectively. In this study, polymer brushes with comparatively high grafting density (c-f, Table 3.1) followed the relationship well. However, those with low grafting density (a-b, Table 3.1) did not exhibit the same behavior possibly attributable to the fact that these samples are not representative of the brush-like regime (Supporting Information).

To understand the interaction of different solvents with the hybrid nanoparticles, the swelling behavior of the grafted polymer brushes in water, toluene and *n*-hexane were examined. As presented in Figure 4.4a, increasing water and toluene contents decreased the value of q_1^* for all samples while maintaining the same ratio for q_1^* and q_2^*. This indicates that for dispersions containing as much as 80% solvent maintained their local ordering of hybrid nanoparticles and the distance between adjacent silica cores increased due to swelling of polymer brushes with both solvents. Further, the observed swelling of the samples was more for the dispersions in water than those in toluene at comparable solvent concentrations. The hybrids were not swollen by *n*-hexane to any appreciable extent. These suggest that although the hybrid nanoparticles have affinities to both water and toluene, their hydrophilic character dominates presumably because of the polar ether groups in the polymer repeat units.

a) (i)

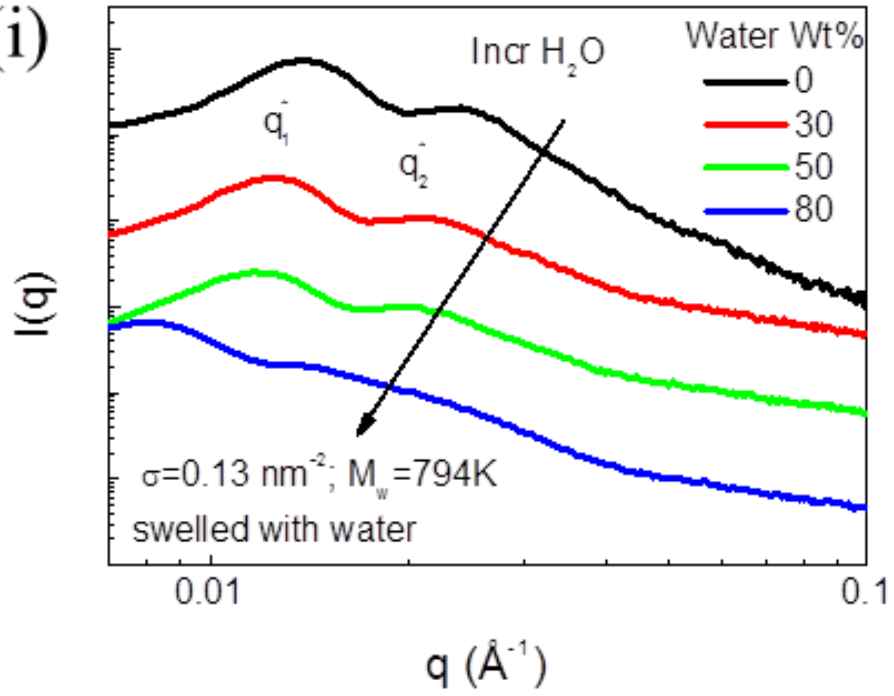
Incr H_2O
Water Wt%
0
30
50
80
q_1^*
q_2^*
I(q)
σ=0.13 nm^{-2}; M_w=794K
swelled with water
0.01
0.1
q (Å^{-1})

(ii)

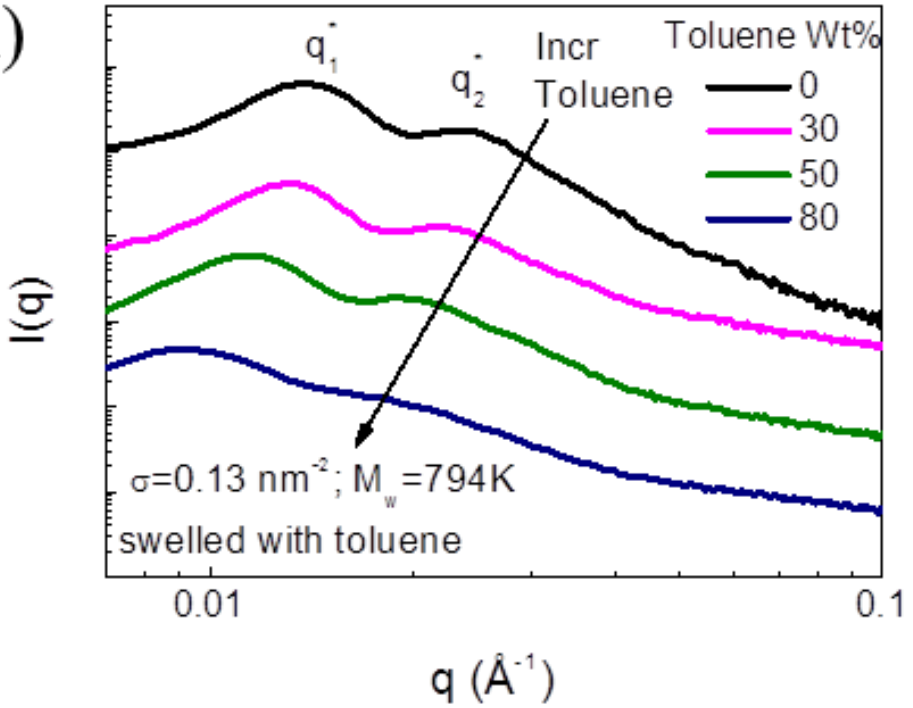
q_1^*
q_2^*
Incr
Toluene
Toluene Wt%
0
30
50
80
I(q)
σ=0.13 nm^{-2}; M_w=794K
swelled with toluene
0.01
0.1
q (Å^{-1})

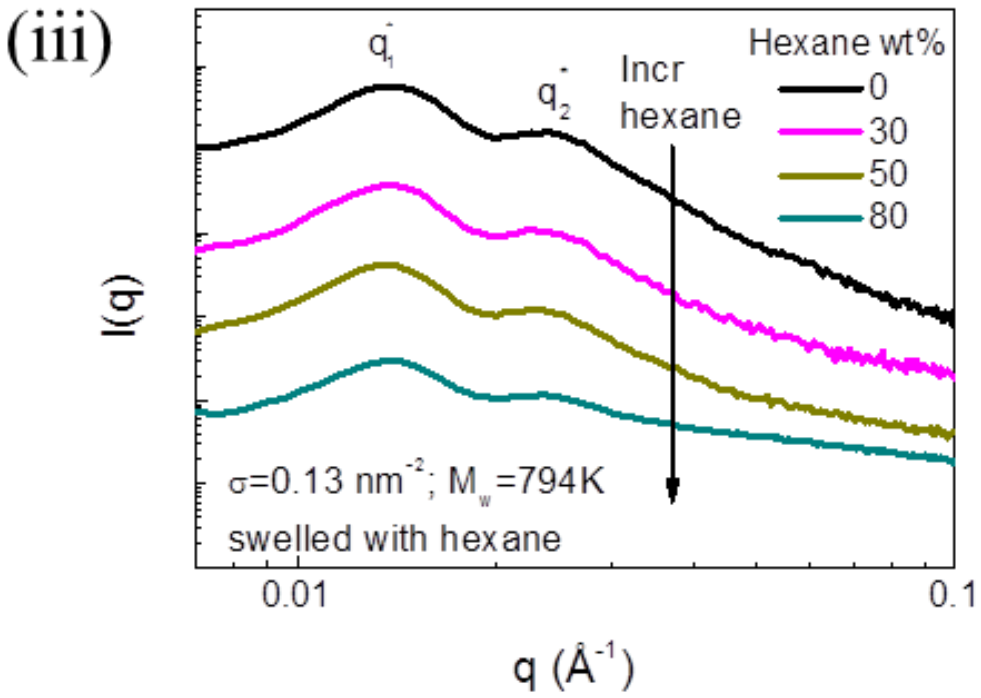
(iii)
q1*
q2*
Incr hexane
Hexane wt%
0
30
50
80
I(q)
σ=0.13 nm-2; Mw=794K
swelled with hexane
0.01
0.1
q (Å-1)

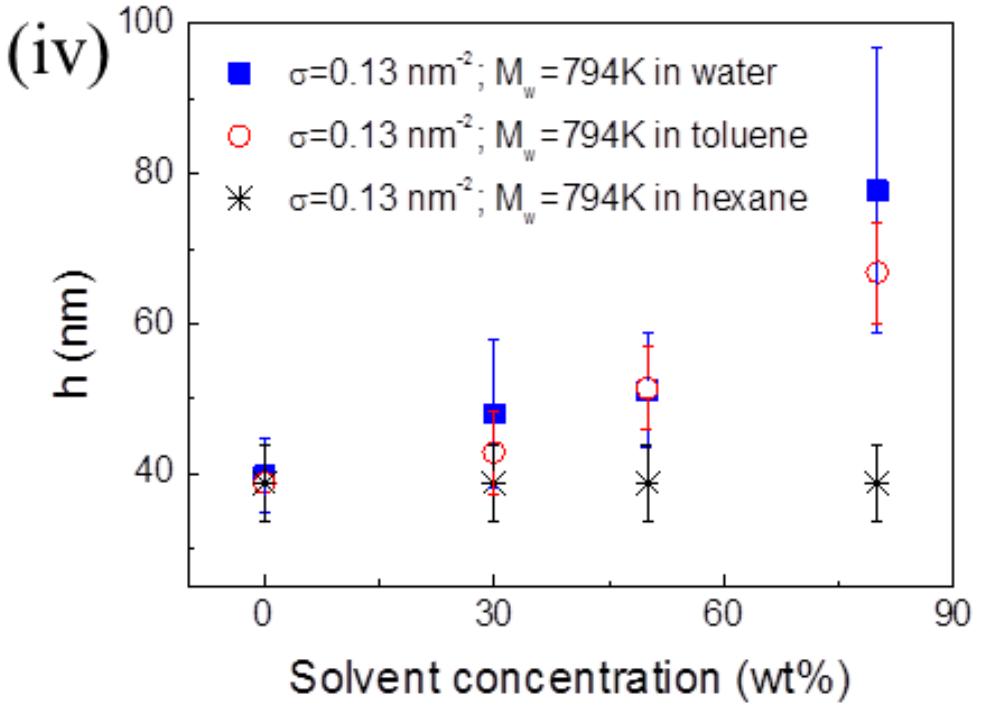
(iv)
σ=0.13 nm-2; Mw=794K in water
σ=0.13 nm-2; Mw=794K in toluene
σ=0.13 nm-2; Mw=794K in hexane
h (nm)
100
80
60
40
0
30
60
90
Solvent concentration (wt%)

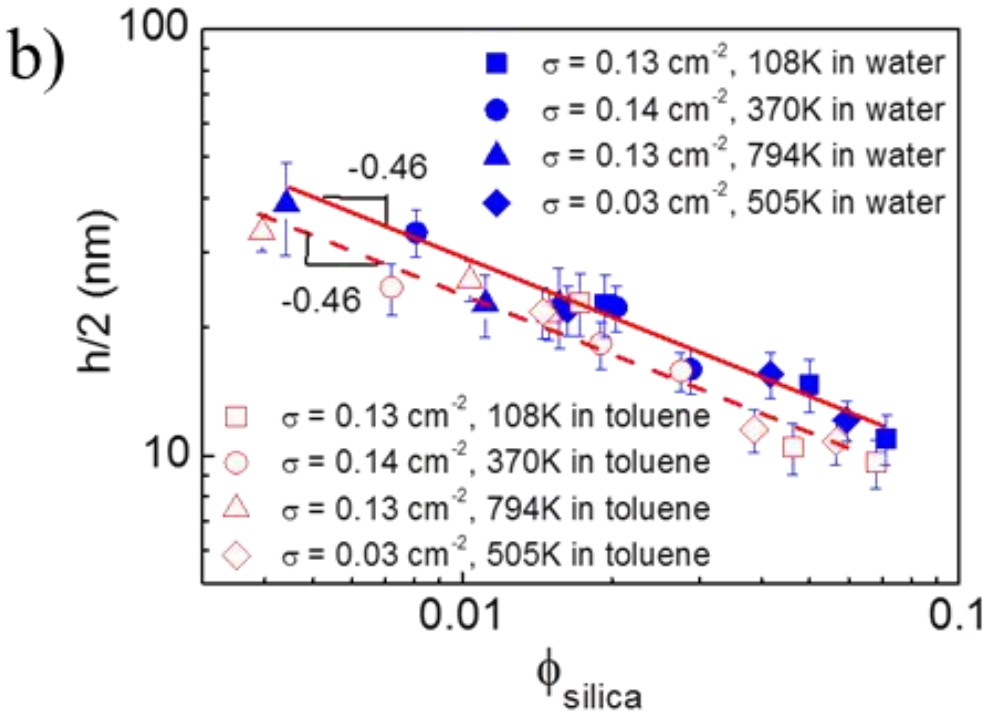

Figure 4.4 a) SAXS data demonstrating the swelling of the hybrid nanoparticles by water b) The scaling of the height of polymer brush (h/2) with silica volume fraction (ϕ_{silica}).

We note that the dilute solution limit of the hydrodynamic size of the individual hybrid nanoparticles dispersed in water (*D*), measured by DLS on highly dilute dispersions, ranged from 77 nm to 168 nm. The values of *the center-to-center distance between nanoparticles* for the semi-dilute and concentrated dispersions of the nanoparticles in water (and toluene) were smaller than the hydrodynamic size (*D*), which indicated that the chains of POEOMA were not fully stretched (or swollen) in the semi-dilute or concentrated dispersions.

Figure 4.4b shows the height of the polymer brush (h/2) as a function of volume fraction of silica (ϕ_{silica}) in the hybrid nanoparticle dispersions. Interestingly the brush height scales as $(\phi_{silica})^{-0.46}$ for both solvents, with the brush height being somewhat larger for the water-based dispersions. We attempt to understand the swelling behavior in the context of the Flory-Rehner (FR) theory of polymer swelling, where the nanoparticles act as multi-functional crosslink junction points. According to the FR theory the equilibrium linear swelling of a polymer *gel* by a good solvent is proportional to the degree of crosslinking to the -0.2 power.[82] In the case of the surface-grafted polymer nanoparticle hybrids, the degree of crosslinking can be replaced by the number of grafting points on the silica surface or silica volume fraction. Alternately, considering the polymer chains are swollen by a good solvent and are only tethered to the nanoparticle at one point, we can reconcile the strong dependence of the swelling of the polymer chains by the solvent to represent simple swelling of a polymer chain by a good solvent. Nevertheless, it would be interesting issue to pursue an understanding of the role of solvent quality on the swelling properties of the nanoparticle hybrids.

Figure 4.5 shows the hexane – water interfacial tension as a function of time. Aqueous dispersions of the hybrid nanoparticles were used with purified *n*-hexane. The hexane – water interfacial tension was reduced from ~50 mN/m to ~20 mN/m presumably because of the segregation of

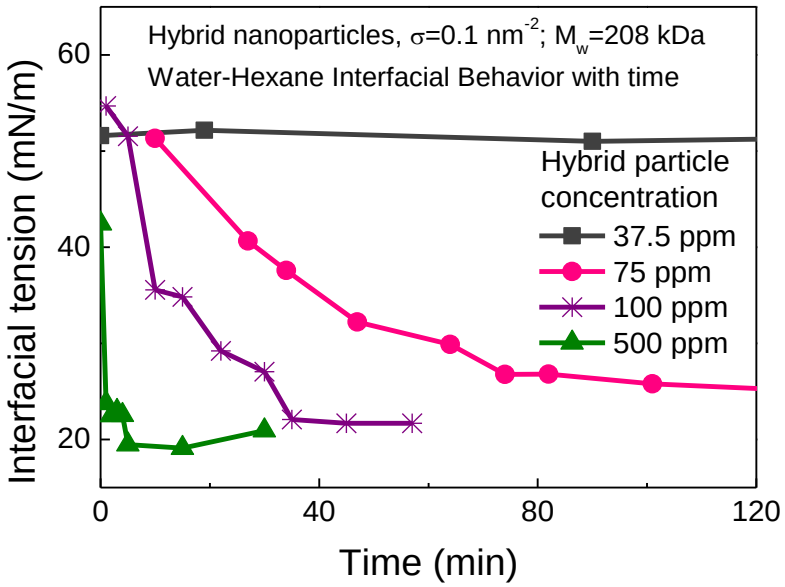

Figure 4.5 Change of hexane – water interfacial tension as a function of time. Four different concentrations of hybrid nanoparticle aqueous solutions were applied as the water phases.

nanoparticles to the interface. For homogeneous particles and hexane – water system, a 30 mN/m reduction in the interfacial tension is noteworthy when compared with previous efforts.[36,38,47,68] POEOMA brushes successfully improved the interfacial activity of the silica nanoparticles and resulted in a significant interfacial tension reduction. The attainment of the maximum reduction in interfacial tension occurred faster when the concentration of hybrid nanoparticles was higher because more nanoparticles can reach to the oil – water interface by diffusion in the same time.

However, for concentration of hybrid nanoparticle dispersions below a certain value, the interfacial tension was not altered from that of the solvent

value in spite of long equilibration times. We identify the concentration of the hybrid nanoparticles where the interfacial tension reached the saturated value first as critical hybrid particle concentration. Figure 4a presents the saturated interfacial tensions as a function of hybrid nanoparticle concentration. Interestingly, the hybrid nanoparticles with σ = 0.13 chains/nm^2; M_w = 794 kDa presented very low critical hybrid particle concentration, the hexane – water interfacial tension reached the minimum at nanoparticle concentration of around 10 ppm. The critical hybrid particle concentration of the systems with varying molecular weight at a fixed grafting density decreased with increasing average molecular weight of the polymer brushes (Figure 4.6a, triangles). Nevertheless, the critical hybrid particle concentration did not have universal correlation with hybrid particle properties such as average molecular weight, grafting density and hydrodynamic hybrid particle diameter (Figure 4.7). However, the critical core concentration based on the silica core concentration of the hybrid nanoparticle (*i.e.,* the number of nanoparticles per unit volume) provides a systematic variation for the efficacy of reducing interfacial tension (Figure 4.6b, 4.8).

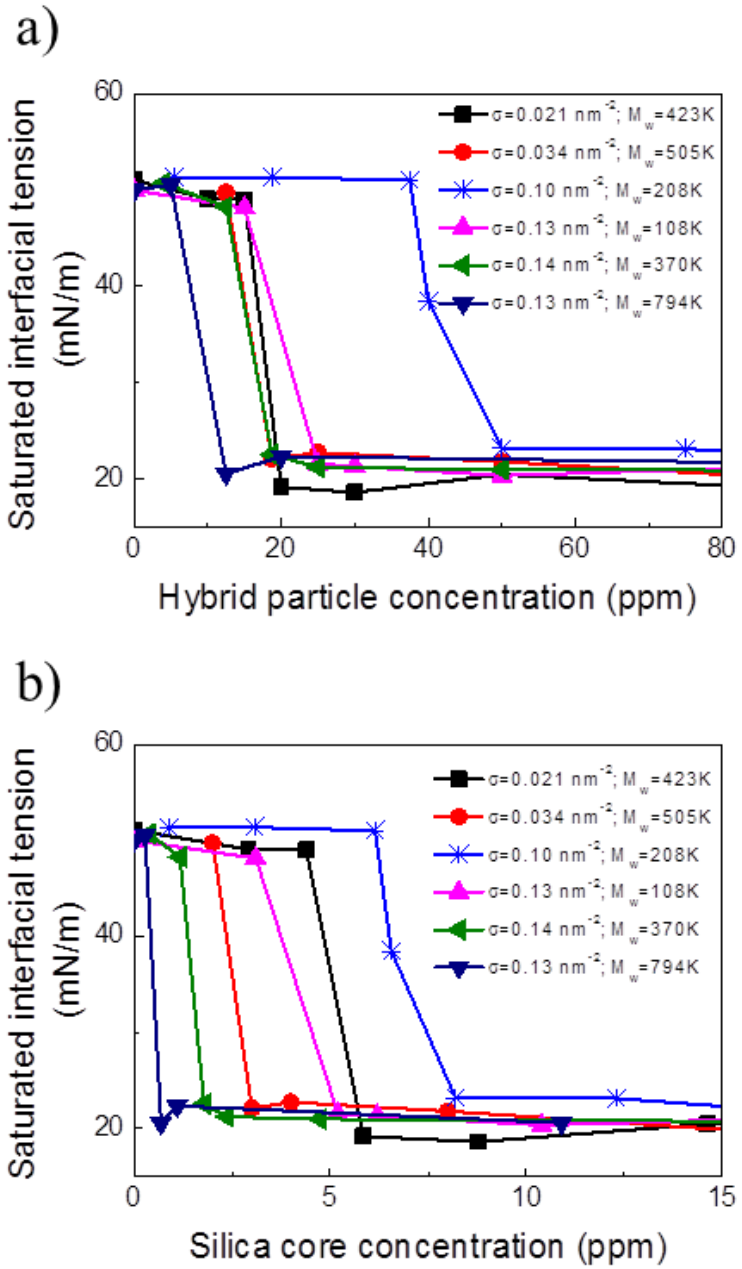

Figure 4.6 Saturated hexane – water interfacial tension as a function of a) hybrid nanoparticle concentration, b) silica core concentration.

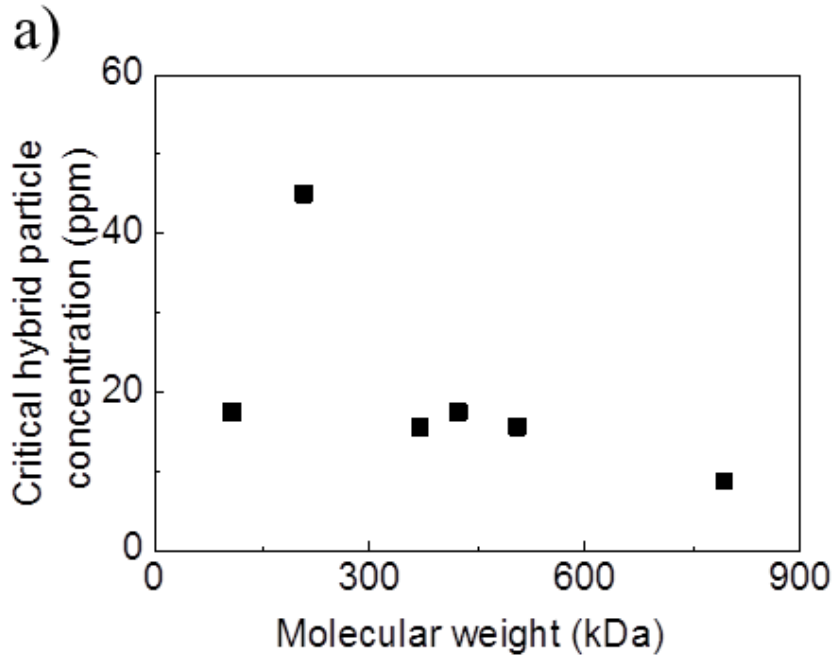
a)
Critical hybrid particle concentration (ppm)
0
20
40
60
0
300
600
900
Molecular weight (kDa)

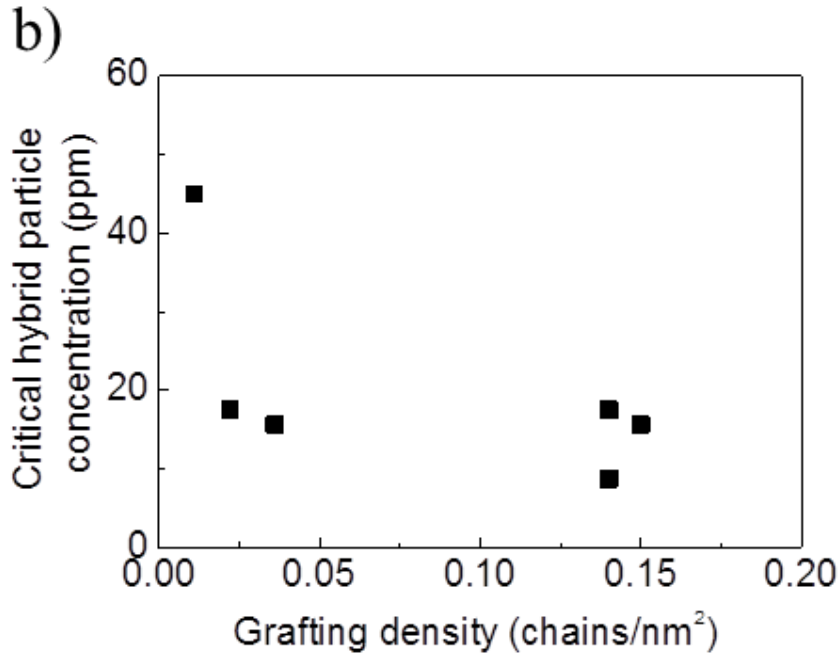
b)
Critical hybrid particle concentration (ppm)
0
20
40
60
0.00
0.05
0.10
0.15
0.20
Grafting density (chains/nm^2)

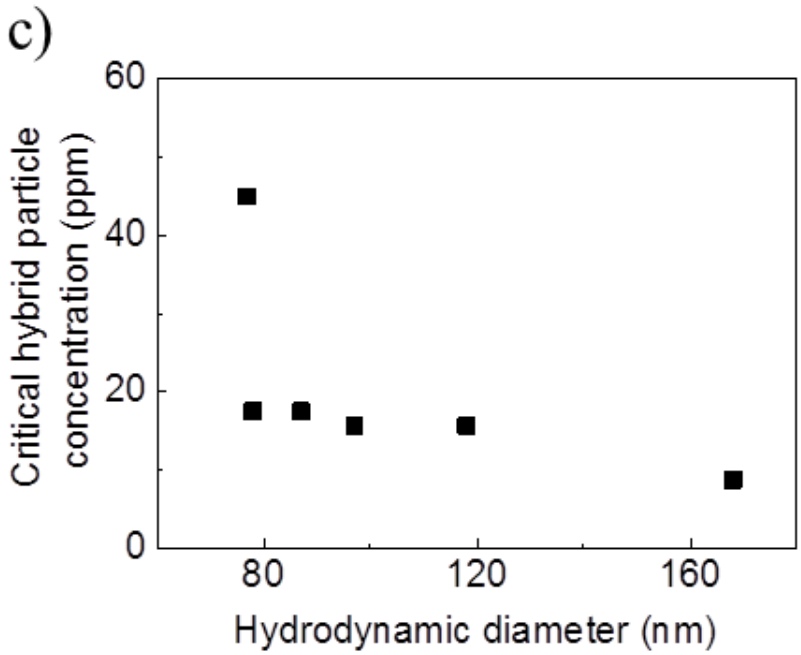

Figure 4.7 Critical hybrid particle concentration as a function of a) weight average molecular weight of polymer brush, b) grafting density, and c) hydrodynamic diameter of the hybrid particles.

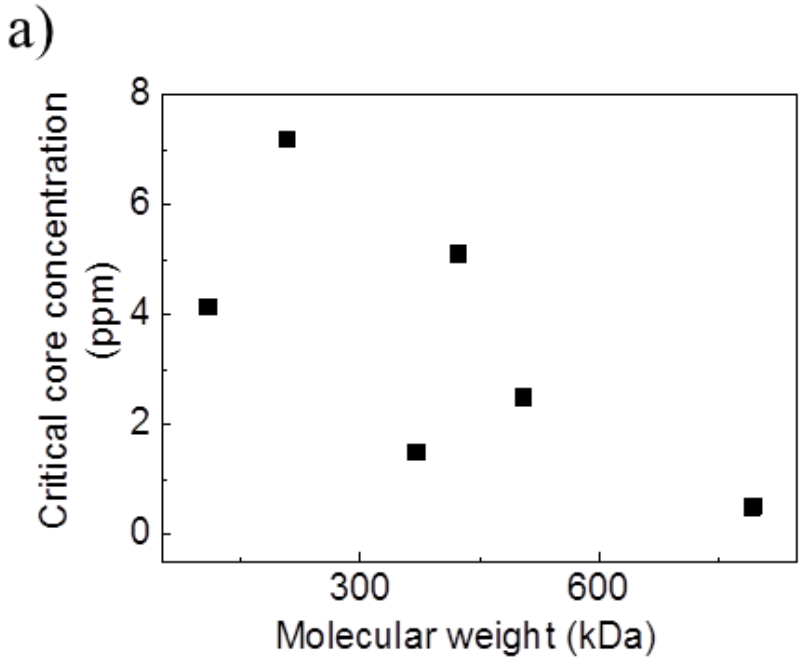

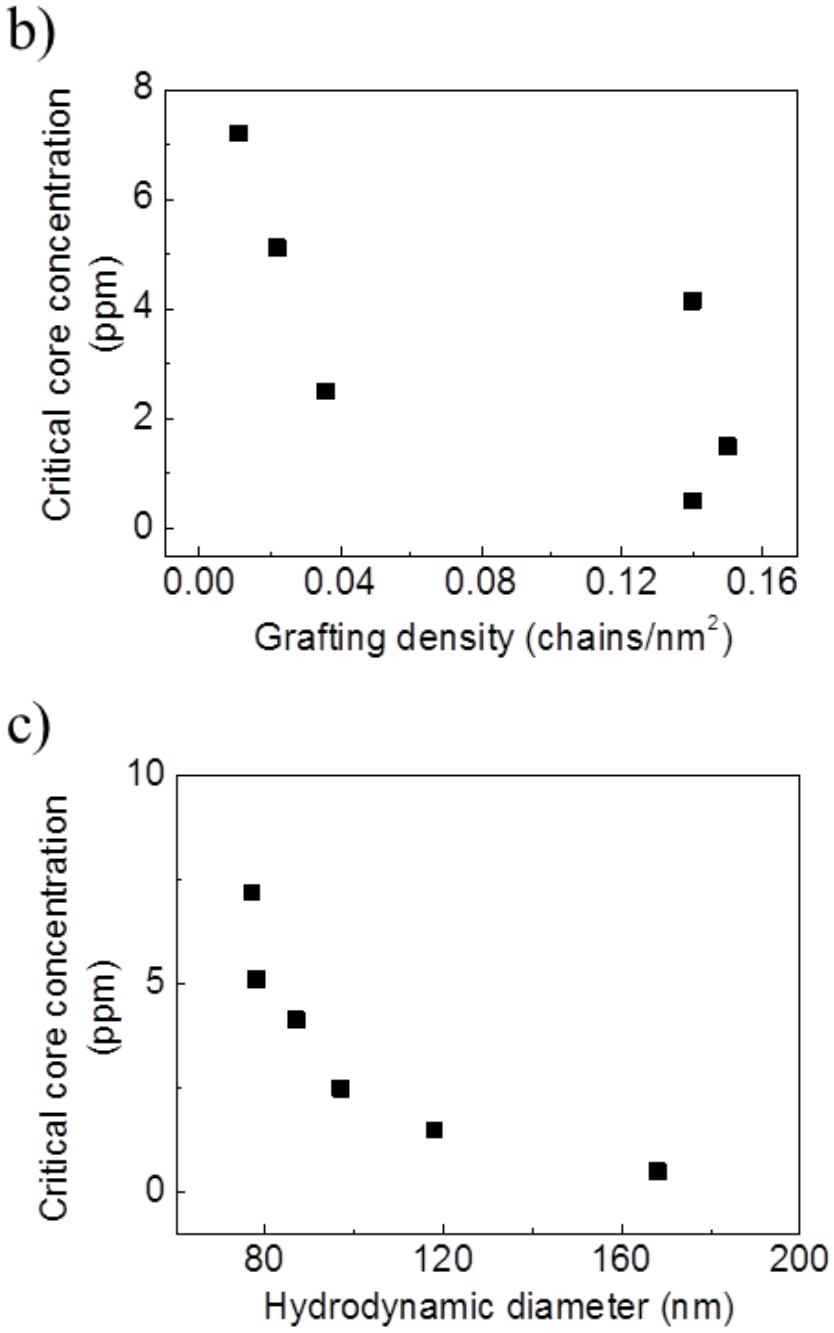

Figure 4.8 Critical core concentration as a function of a) weight average molecular weight of polymer brush, b) grafting density, and c) hydrodynamic diameter of the hybrid particles.

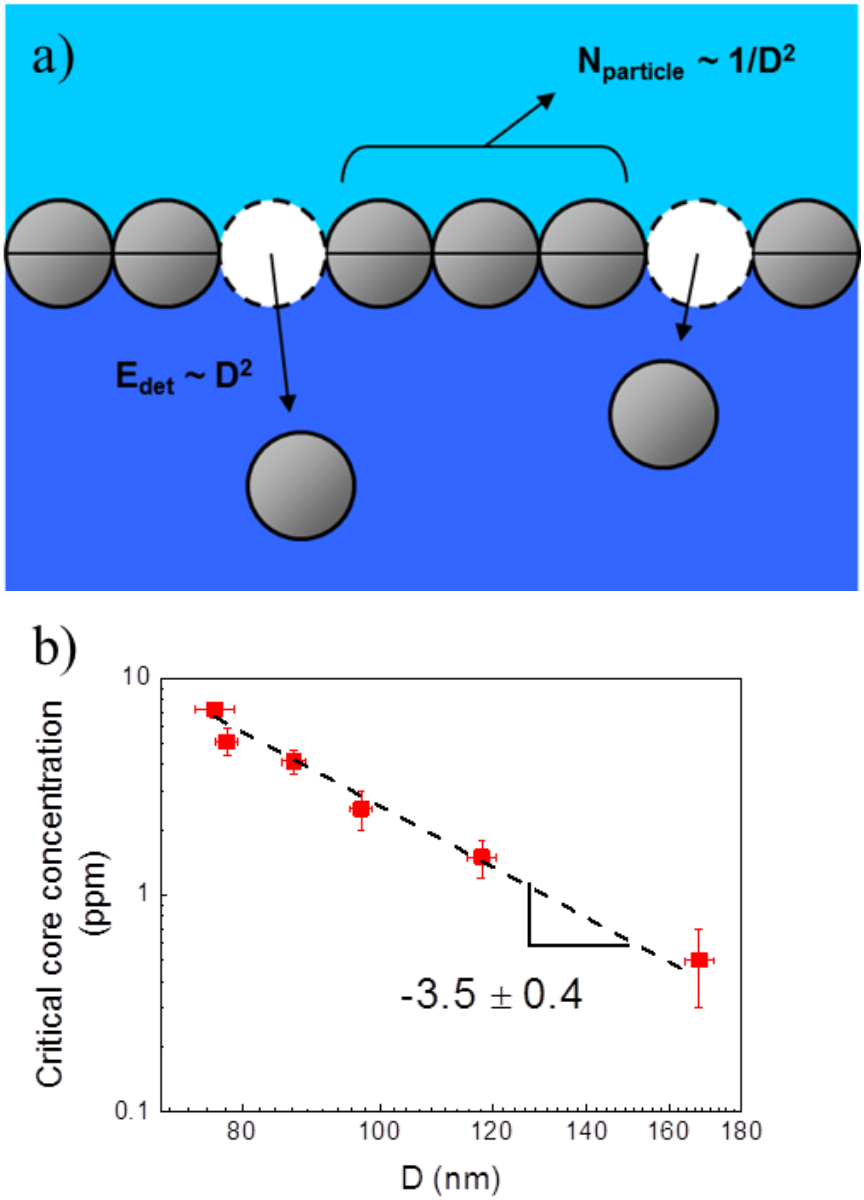

Figure 4.9 a) A simple model for particle size effect on the critical particle concentration. b) The critical core concentration as a function of hydrodynamic hybrid nanoparticle diameter.

To understand the mechanism of hybrid nanoparticle induced reduction in the hexane – water interfacial tension and to explain the strong dependence of the critical core concentration on the hydrodynamic size of the nanoparticle, we conjecture a simple physical model, shown in Figure 4.9a,

that the critical core concentration occurs when the nanoparticles enrich the interface and form a jammed or ordered structure at the interface. Previously, it has been shown that charged particles arrange as a two-dimensional hexagonally-ordered structure at the oil – water interfaces and we conjecture that the hybrid nanoparticles exhibit similar behavior.[83] Assuming that these hybrid nanoparticles behave as hard spheres and that they occupy non-preferentially at the interface, the maximum number of nanoparticles per unit area of hexane – water interface ($N_{particle}$) scales inversely as the cross-sectional area of the nanoparticle (i.e., D^2). Additionally, more particles can overcome the thermal fluctuation and situate at the interface if their size is larger because the detachment energy of a single particle (E_{det}) is proportional to square of its diameter, D^2.[34] In the absence of any differences in chemical structure of the particle or the polymer, the specific detachment energy per unit area does not change as the hydrodynamic size of the particle is changed through a manipulation of grafting density and molecular weight. Therefore the concentration required to overcome thermal energy for the assembly of nanoparticles at the oil – water interface is reduced with a D^{-2} scaling. Combining the contributions of the change in detaching energy and the maximum number of particles per unit interfacial surface, the critical core concentration (or the number of spherical particles in solution to result in saturating the interface) is expected to scale as D^{-4}.

The experimental variation of the critical core concentration dependence on D is shown in Figure 4.9b. The data suggest that the critical core concentration varies as $(D)^{-3.5\pm0.4}$. The discrepancy from the simple phenomenological model can be attributed to the changes in chain stretching of the grafted polymers at the hexane – water interface, as would be expected based on the solvation potential of the two solvents. As previous studies have reported, the size and conformation of the hybrid particle at the oil – water interface is possibly changed from that in the bulk solvent to minimize the interfacial free energy.[45-47,84] Moreover, the model used above expects the particle and the attached polymer to partition non-preferentially at the oil-water interface. Any deviation from this would lead to a weakening of the power law behavior. Consequently, the experimental results disagree slightly from the hard sphere model we suggested, and it possibly the cause for the slight discrepancy between the theoretical and the experimental values of exponents (4 and 3.5 respectively). However, the result demonstrates that the hybrid nanoparticles' hydrodynamic size which can be controlled by properties of polymer brushes (molecular weight and grafting density) is the essential parameter to control the efficacy of such hybrid nanoparticles to alter the interfacial properties at the interface of two immiscible liquids.

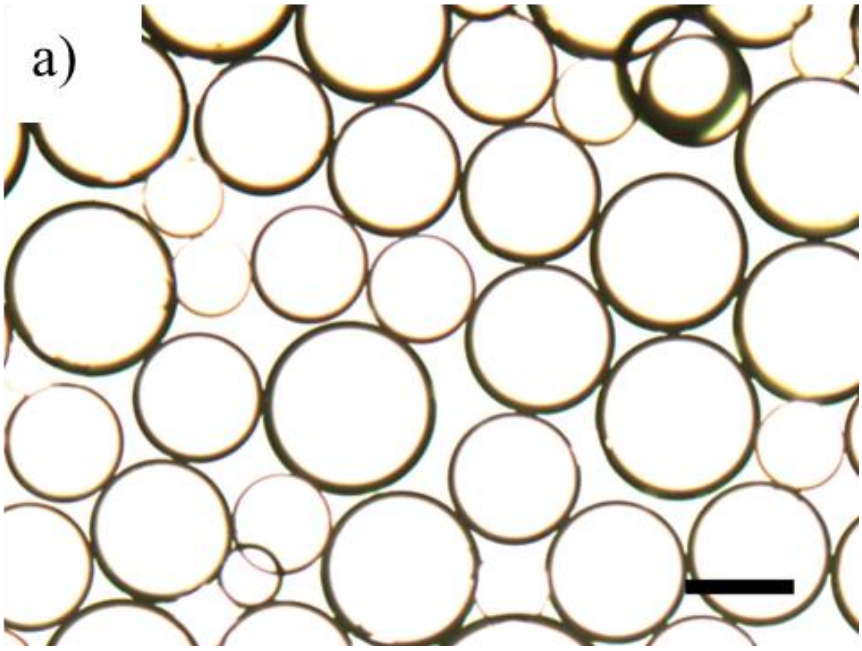
a)

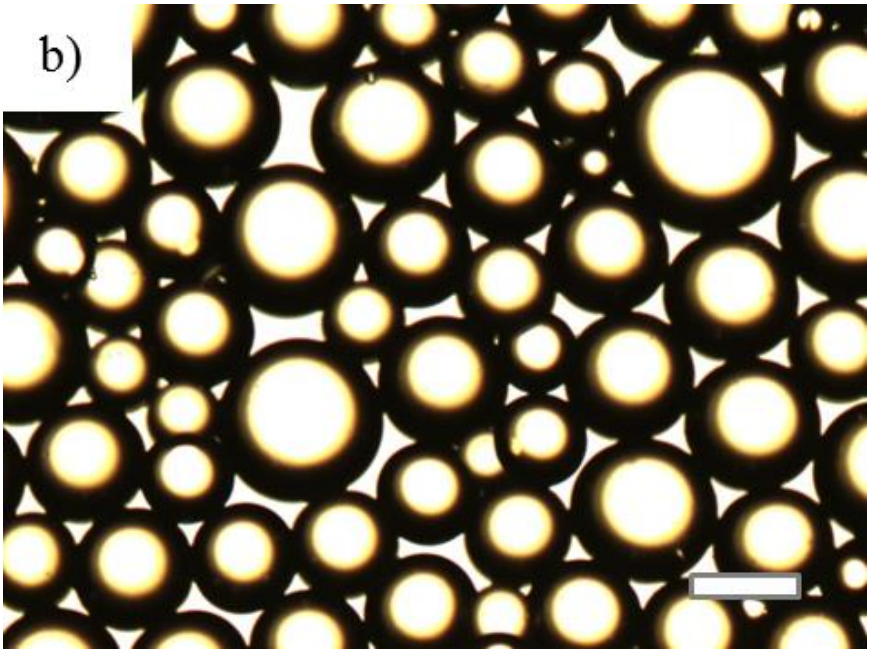
b)

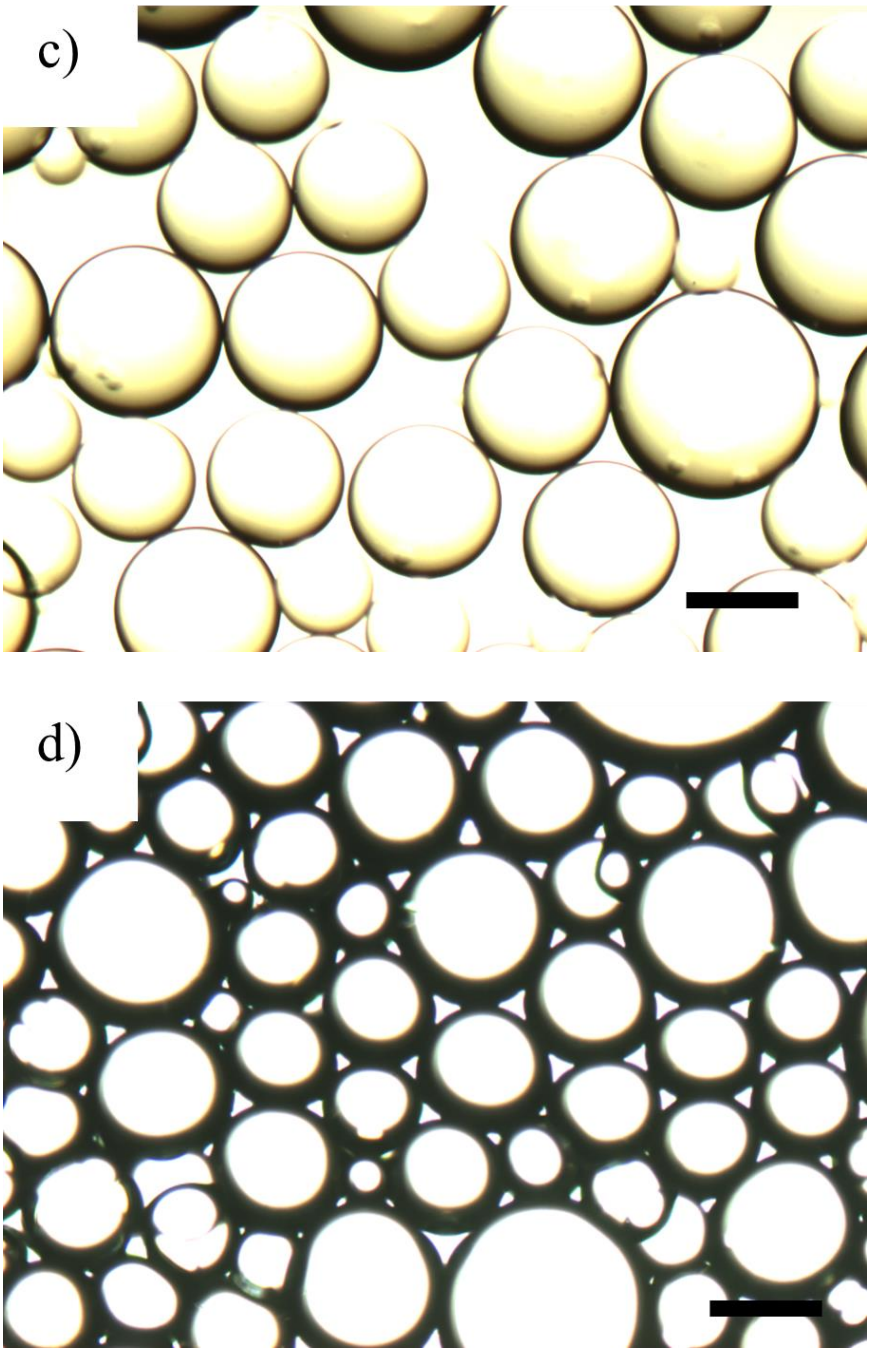

Figure 4.10 A microscope picture of hexane – water emulsion a) 22 hours, b) 69 hours after mixing, a squalene – water emulsion c) 22 hours, d) 69hours after mixing (The scale bar indicates 200 μm.)

a)

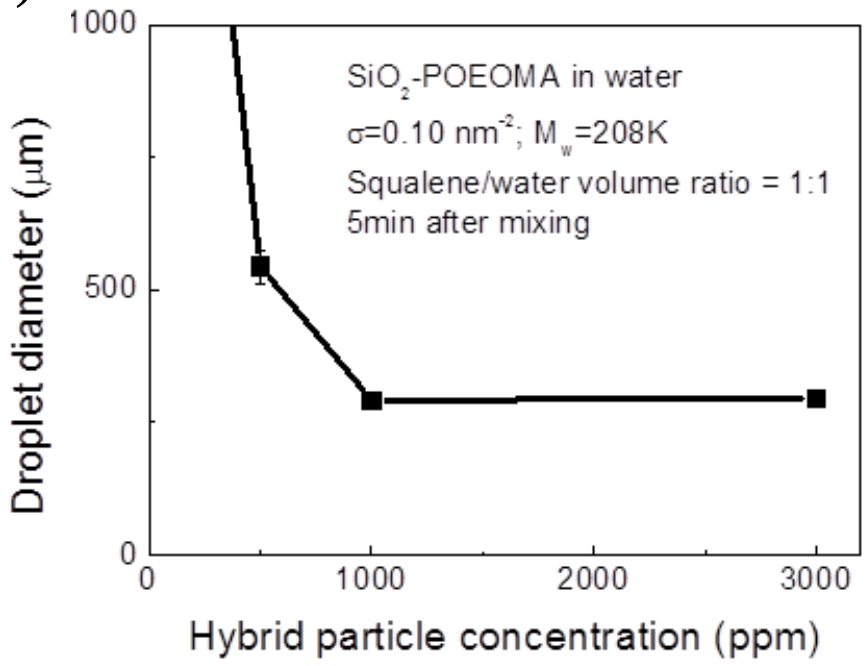
1000
500
0
0
1000
2000
3000
Droplet diameter (μm)
Hybrid particle concentration (ppm)
SiO2-POEOMA in water
σ=0.10 nm-2; Mw=208K
Squalene/water volume ratio = 1:1
5min after mixing

b)

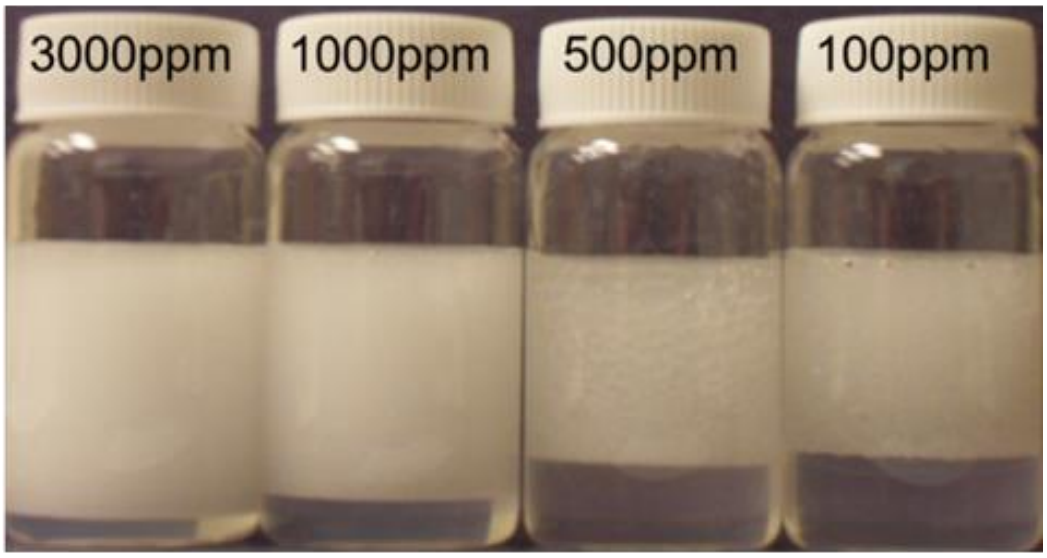
3000ppm
1000ppm
500ppm
100ppm

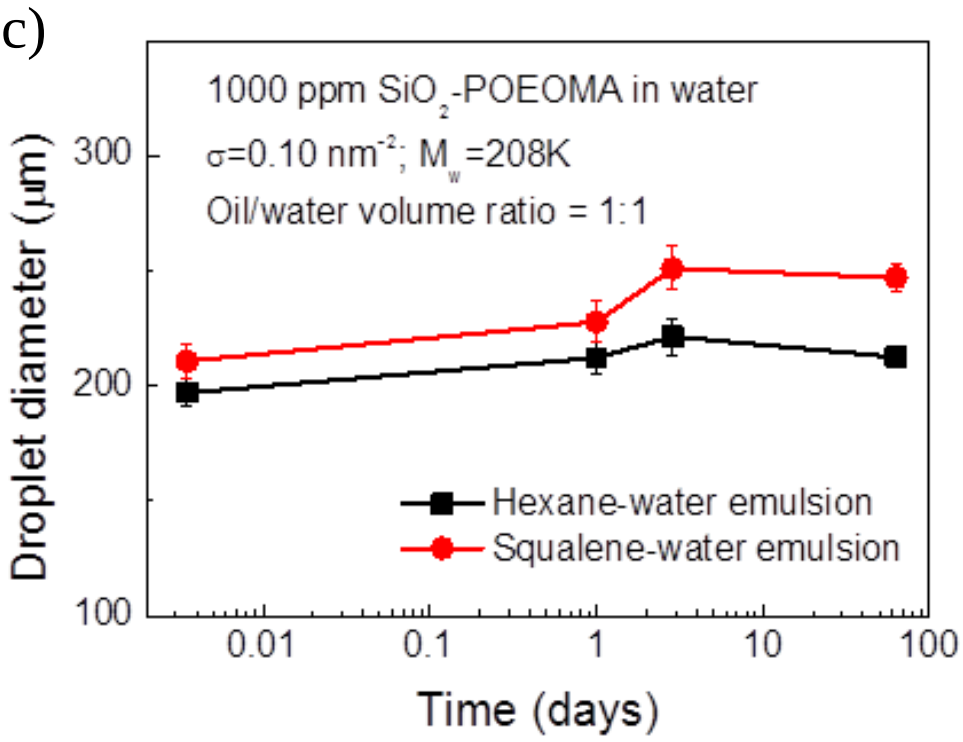

Figure 4.11 Emulsion droplet size analysis: a) emulsion droplet diameter as a function of nanoparticle concentration b) a picture of squalene – water emulsions c) droplet diameter as a function of time.

From the observed surface activity and structural behavior of the hybrid nanoparticles, oil – water emulsions were made by applying the hybrid nanoparticles to an equi-volume mixture of oil and water to examine their capacity as oil dispersants. *n*-Hexane and squalene were used as representative oil-like species and mixed to aqueous solutions (with dispersed hybrid nanoparticles) resulting in 1:1 oil – water volume ratio mixtures. Mixing was obtained using a vortex mixer for 60 sec at the max speed to form oil – water emulsions. Segregation of nanoparticles at oil – water interface

was confirmed by cryo-scanning electon microscopy (SEM) of the emulsion droplets. The size variation of the emulsion droplet with different concentration of aqueous hybrid nanoparticle solutions in water, and the stability of the emulsion droplet were observed based on the images taken by optical microscopy. Because of their lower interfacial tension (10 mN/m), squalene and water made somewhat smaller emulsion droplet than hexane – water system (Figure 4.10a-b). Five minutes after the emulsification with different hybrid nanoparticle concentrations, the emulsion droplets made with a 100 ppm hybrid nanoparticle aqueous solution rapidly coalesced. However, by increasing the concentration of hybrid nanoparticles, the emulsions became stable and the droplet size reached 290 μm for 1000 ppm hybrid nanoparticle aqueous solution (Figure 4.10c). Also, the amount of the emulsion increased with increasing hybrid nanoparticle concentration (Figure 4.10d). Oil – water emulsions with 1000 ppm hybrid nanoparticles aqueous solution were stable after 63 days without significant change in droplet sizes (Figure 4.11a). This implies that the emulsion is stable if the concentration of the hybrid nanoparticles is high enough that their attachment to the oil – water interface is dominant compared to the detachment.

4.4 Conclusions

We have studied the structure and the interfacial activity of silica nanoparticles, grafted with hydrophilic polymers by surface initiated atom transfer living radical polymerization, at oil – water interface. In spite of their low grafting density (< 0.15 chains/nm2), the small angle X-ray scattering patterns of solvent-free hybrid nanoparticles showed characteristic scattering peaks, consistent with a face centered cubic or hexagonal close packed structure. The interparticle distance between silica nanoparticles, estimated from SAXS measurements for the modest grafting density were consistent with the scaling predicted by Daoud and Cotton for highly grafted brushes. On the other hand, the swelling behavior of these nanoparticles in a good solvent were consistent with free-swelling of polymer chains rather than that of cross-linked polymer gels and an interesting avenue of future research would be to pursue the swelling characteristics with systematic variation in solvent quality.

The hybrid nanoparticles reduced the hexane – water interfacial tension from ~50 mN/m to ~20 mN/m even at very low concentration (~ 10 ppm) of nanoparticles. A strong correlation between critical nanoparticle concentration and hybrid particle diameter (D) was observed. We conjecture that the strong dependence of the critical particle concentration on hydrodynamic size is due to the packing of the hybrid nanoparticles at interface and the interfacial free energy of the hybrid nanoparticles. The

slightly weaker than expected dependence might be caused by the modest grafting density of the polymer chains and the adjustment of chain conformations afforded at the interface as compared to the good solvent case where the hydrodynamic size was measured. We expect a systematic study of solvent quality on hydrodynamic size and the behavior of such hybrid nanoparticles at high grafting densities are natural follow-ups of this work.

Using the hybrid nanoparticles as emulsion stabilizers, hexane – water and squalene – water emulsion were made and their stabilities and droplet sizes was observed. By applying more than 0.1% hybrid nanoparticles, both emulsions were stable more than 3 months and oil phase were dispersed to 200~300 micrometer size droplets. Future work include mechanisms to control the size of dispersed oil in water emulsions as well as mechanisms to further lower the interfacial tension of oil-water mixtures using simple hybrid nanoparticles.

Chapter 5 Amphiphilic copolymer grafted silica nanoparticles as oil dispersants

5.1 Introduction

The distinctive properties of nanoparticles, which were originated from huge surface area to volume ratio and their surface tenability, make them attractive for potential applications in various fields such as enhanced oil recovery, food, and drug delivery as interfacial agents.[1,85-87] It is also known that small particles such as nanoparticles are able to reduce oil – water interfacial energy and make emulsions by segregating into their interface. The segregating tendency of the small particles is thermodynamically well explained. Change in free energy, F_{int}, of a system where a spherical particle situates at oil – water interface can be expressed as

$$F_{int} = -\pi R^2 \gamma (\cos\theta \pm 1)^2, \quad (1)$$

where R is the radius of the particle, γ is the interfacial tension between two immiscible fluids, and θ is a water contact angle on the particle surface.[33,34] The sign inside the bracket is negative for a particle originally dispersed in water phase, and positive for a particle originally dispersed in oil phase. Since F_{int} has always a negative sign regardless of the signs and values of the other parameters, small particles preferentially segregate into fluid interface rather than the bulk fluids and reduce the interfacial energy. The reduction of the interfacial energy with the small particles is maximized with contact

angle (θ) of 90° and minimized with contact angles of 0 and 180°. However, it is limited for nanoparticles to reduce the interfacial energy due to their small radius even if the contact angle is 90°; thus additional techniques are required to improve their interfacial activity and use them as efficient emulsion stabilizers.

Binks *et al.* theoretically predicted the improvement of the interfacial activity of the "Janus" particle, a particle having two different surface regions with two contact angles, compared to the particle with homogeneous surface wettability.[35] By assuming the maximum amphiphilicity, desorption energy of the Janus particle placed at the fluid interface was 3-fold greater than that of the homogeneous particle. Moreover, the Janus particle presented strong adsorption even if the average contact angle, which was calculated based on the relative area of hydrophilic and hydrophobic particle surface regions, was set as 0 and 180°. The desorption energy of the particle is an identical value with interfacial energy reduction induced by a particle segregation into the interface of two fluids. Therefore, efficiency of the particles as emulsifiers can be improved by making their surface wettability inhomogeneous like Janus particles. Glaser *et al.* experimentally confirmed this theoretical prediction by showing improved interfacial activity of surface modified gold-iron Janus nanoparticles against that of homogeneous iron and gold nanoparticles.[36]

Introduction of polymers, covalently grafted or physically adsorbed on the particle surface, also improve the emulsion stabilizing ability of the

particles.[38,39] The polymers provide dilatational modulus to the particles and help to prevent the demulsification induced by Ostwald ripening which is a process whereby larger droplets grow at the expense of smaller ones because the solubility of a component in a droplet increases as the interfacial curvature increases.[40] It is known that if the following condition is satisfied, Ostwald ripening does not occur.

$$E = \frac{d\gamma}{d \ln A} \geq \frac{\gamma}{2}, \quad (2)$$

where, E is surface dilatational modulus, γ is interfacial tension, A is a surface area of an oil droplet.[41] In addition, particles with amphiphilic block copolymer brushes can behave like Janus particles at the fluid interface. Simulation studies of a block copolymer grafted particle, situated at the fluid interface, showed their Janus-like surface nature induced by arrangement of the each block of copolymer brushes.[42,43] Therefore, the advantage of the Janus surface nature can be taken simply by grafting amphiphilic block copolymer brushes on the nanoparticles without challenging steps to synthesize the Janus particles.

In this chapter, we grafted amphiphilic block copolymer brushes with two different blocks of poly(oligo(ethylene oxide) monomethyl ether methacrylate) (POEOMA) and polystyrene (PS) from the surface of silica nanoparticles in order to improve their interfacial activity and emulsion stabilizing ability. Using these hybrid nanoparticles, interfacial activity improvement induced by amphiphilic block copolymer brushes were

investigated and the unique behavior of hybrid nanoparticles at the oil – water interface was visually observed.

5.2 Methodology

5.2.1 Materials

Colloidal silica nanoparticles (MIBK-ST, effective diameter ~15 nm, 30~31 wt% silica in methyl isobutyl ketone) were acquired from Nissan Chemical. Allyl 2-bromo-2-methylpropionate (98%, Sigma-Aldrich), chlorodimethylsilane (98%, Sigma-Aldrich), 5% platinum on activated charcoal (Sigma-Aldrich), Hexamethyldisilazane (HMDS, 99.9%, Sigma-Aldrich), tetrahydrofuran (THF, 99.9+%, Sigma-Aldrich), copper(I) bromide (98%, Sigma-Aldrich), copper(II) bromide (99%, Sigma-Aldrich), anisole (anhydrous, 99.7%, Sigma-Aldrich), N,N,N′,N″,N″-Pentamethyldiethylenetriamine (PMDETA, 99%, Sigma-Aldrich), 2,2'-bipyridyl (bpy, 99+%, Sigma-Aldrich) methanol (99.8%, Mallinckrodt), hydrofluoric acid (48~51%, VWR), and magnesium sulfate (97+%, Sigma-Aldrich) were used as received. Toluene (99.5%, Macron) and *n*-hexane (98.5%, Macron), used for the interfacial tension measurements, was purified by passing through a basic alumina column three times. Oligo(ethylene oxide) monomethyl ether methacrylate (OEOMA, Mn=300, Sigma-Aldrich) and styrene monomer (99+%, Sigma-Aldrich) was passed through the column which was packed with inhibitor remover (for monomethyl ether

hydroquinone, Sigma-Aldrich) and neutral alumina (Sigma-Aldrich) to remove inhibitors.

5.2.2 Preparation of amphiphilic copolymer grafted silica nanoparticles.

PS chains were grown from polymer chain ends of the SiO_2-POEOMA macroinitiator using the ATRP method. CuBr (12 mg, 0.08 mmol) were placed in a round bottom flask. N,N,N′,N″,N″-Pentamethyldiethylenetriamine (PMDETA, 16.7 μl, 0.08 mmol), styrene (10.4 g, 125 mmol), anisole (10 g) and SiO_2-POEOMA macroinitiator (0.2 g) were added to another round bottom flask. After sealed with rubber septum, both flasks were purged with nitrogen gas for an hour. The mixture in the second flask was transferred to another flask using cannula needle by nitrogen pressure. The reaction mixture was stirred for 5 minute and put into the oil bath which was preheated to 100°C. The polymerization was conducted for 0.5 - 4 hours and then terminated by introducing air to the mixture and cooling the flask. The reaction mixture was diluted with THF, and copper catalysts were removed by passing through a column filled with neutral alumina. The THF was evaporated in the rotary evaporator and remaining solution was precipitated in methanol. The precipitants were recovered by centrifugation and dried overnight at 80°C under the vacuum.

Table 5.1 ATRP of PS from SiO_2-POEOMA

Sample	M_n (kDa)	M_w (kDa)	M_w/M_n	PS/ POEOMA weight ratio[1)]	Grafting density (chains/nm^2)	Number of polymer chains per particle	d[2)] (nm)	D[3)] (nm)
SiO_2-POEOMA	15	21	1.4	0	0.57±0.04	487±54	27±1	69±1
SiO_2-P(OEOMA-b-sty)	26	37	1.4	1.2	0.62±0.05	530±61	39±1	81±2
	55	104	1.9	2.8	0.51±0.04	436±50	51±2	146±4
	82	119	1.5	3.8	0.53±0.04	453±52	54±3	155±4

1) Estimated from H-NMR measurements
2) Center-to-center distance of silica nanoparticles measured by SAXS in bulk melt state of the polymer
3) Hydrodynamic size of dispersed hybrid nanoparticles measured by DLS in toluene

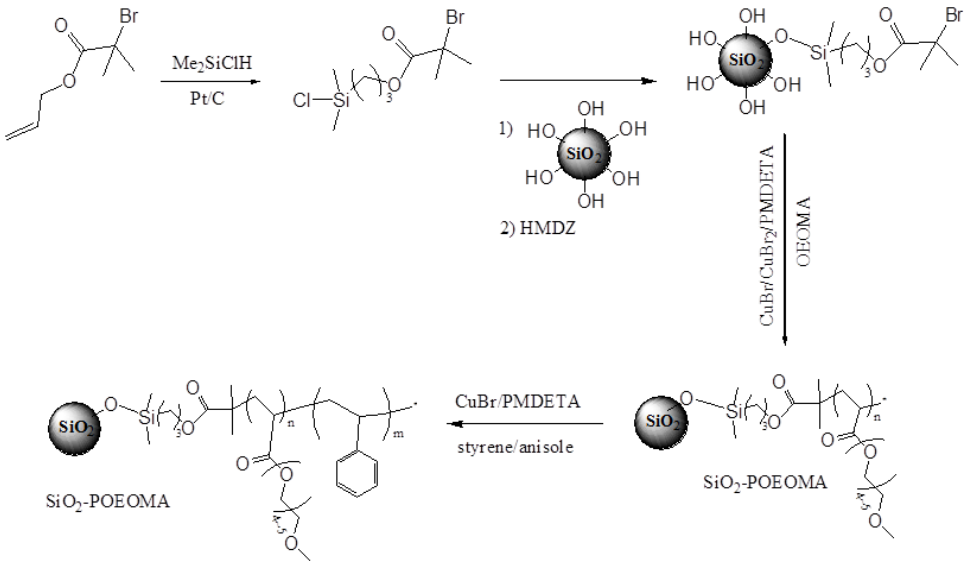

Scheme 5.1 General scheme for synthesis of initiator attached silica nanoparticles, surface initiated ATRP of POEOMA, and chain extension of PS.

5.2.3 Thermal gravimetric analysis (TGA)

Polymer content in hybrid nanoparticles was measured by thermal gravimetric analysis (TGA Q500, TA instrument). The measurement was performed under argon atmosphere from 25 °C to 800 °C at a heating rate of 10 °C/min. Effective weight losses of the hybrid nanoparticles during the heating process were obtained by the measurement and used towards the calculation of the grafting density.

5.2.4 Size exclusion chromatography (SEC)

The molecular weight and polydispersity index (PDI) of polymer brushes grafted on silica nanoparticles were determined by size exclusion chromatography (Viscotek 270 triple detection system). Before the measurements, the polymer brushes were cleaved from the nanoparticles using hydrofluoric acid. These average molecular weights of the cleaved polymer brushes obtained from the SEC and weight loss data from the TGA measurements were used to calculate the grafting densities of the hybrid nanoparticles.

5.2.5 Dynamic light scattering (DLS)

Hydrodynamic diameters of the bare silica nanoparticles and polymer grafted hybrid nanoparticles in a good solvent were measured by dynamic light scattering (Brookhaven Instrument, BI-200SM). Scattering of 1000 ppm aqueous solutions were measured at three different scattering angles (60°, 90°, 120°) using a laser emitting a light with a wavelength of 637.6nm. The

fluctuations in the intensity of the scattered light as a function of the delay time is expressed by an autocorrelation function and mathematically treated as an exponential decay function. From the decay rate, the diffusion coefficient of the particles in a solvent was calculated. The hydrodynamic radius of the particles was determined through the diffusion coefficient and Stokes-Einstein equation.

5.2.6 Small angle X-ray scattering (SAXS)

The structure of the hybrid nanoparticles and the inter-particle distance were estimated by small angle X-ray scattering measurements using a Rigaku SMax3000 with a MicroMax-007HF rotating anode X-ray generator. If hybrid nanoparticles were arranged in regular order, constructive interference of X-ray beams results in diffraction peaks and the type of crystal structure can be estimated based on the arrangement of those peaks. From the geometry of this crystal structure and the q value of the first diffraction peak (q1*), the size of the hybrid nanoparticles and inter-particle distance were calculated.

5.2.7 Pendant drop method

The interfacial tension between toluene and water was measured by the standard pendent drop method. Toluene was purified by passing through a neutral alumina column before the measurements. The purified toluene was filled in a quartz cuvette and used as the atmospheric phase. 5~6 μl of water was injected into the toluene atmosphere from a needle to make a

water pendant drop. The image of deformed water droplet was captured using the tensiometer (OCA 15EC, DataPhysics), and the toluene – water interfacial tension was calculated from the geometry of the pendant drop.[54]

5.3 Results and discussions

Block copolymers of oligo(ethylene oxide) monomethyl ether methacrylate and styrene (POEOMA-b-PS) were grafted from 15 nm silica (SiO_2) nanoparticles using the surface initiated atom transfer polymerization method. In order to produce nanoparticles with amphiphilic surface nature, hydrophilic POEOMA was first grown from silica nanoparticles then hydrophobic PS chains were extended (Scheme 4.1), and a set of four hybrid nanoparticles described in Table 4.1 was prepared. The weight average molecular weight (M_w) of polymer brushes, which was varied from 21 to 119 kDa, and successful PS chain extension from POEOMA chain ends was confirmed by SEC (Figure 5.1). The composition of the each POEOMA and PS block was confirmed with proton nuclear magnetic resonance spectroscopy (H-NMR) as well (table 5.1). The grafting density was calculated using thermogravimetric analysis (figure 5.2) of hybrid nanoparticles, the molecular weight data of polymer brushes, and the density value of the silica nanoparticles acquired from literature (2.65 g/m^3).[79,88] All the samples had similar grafting densities (0.51 – 0.62 chains/cm^{-2}), which indicated that the PS chains were grown from most POEOMA chain ends.

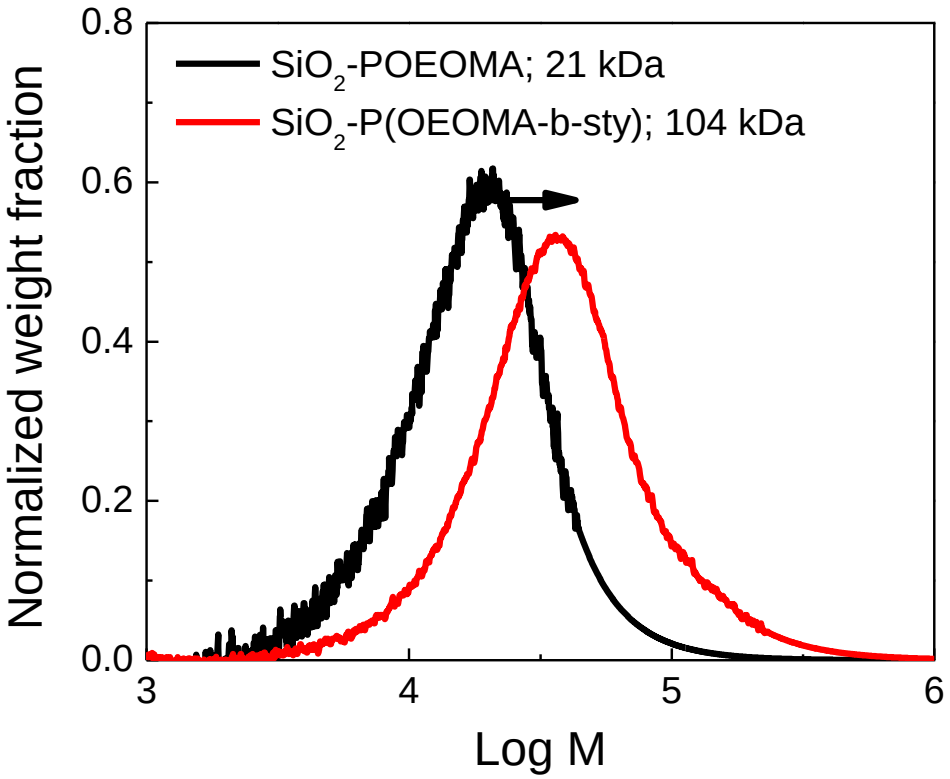

Figure 5.1 SEC curves of SiO_2-POEOMA macroinitiator and PS chain extended SiO_2-P(OEOMA-b-sty).

The structure of melt-state hybrid nanoparticles was estimated by small angle X-ray scattering (SAXS). As observed in Figure 5.3, SAXS data from the hybrid nanoparticles melts presented two peaks labeled as q_1^* and q_2^* and q_1^*: q_2^*:: 1:$\sqrt{3}$ for all copolymer grafted nanoparticles, which indicated their lattice structure with weak face centered cubic (FCC) or random hexagonal close packed (HCP) ordering. Goel et al and Vlassapoulos et al reported similar observations on the ordered lattice structures of hybrid nanoparticles and star polymers.[73,80] The secondary peak (q_2^*) from the

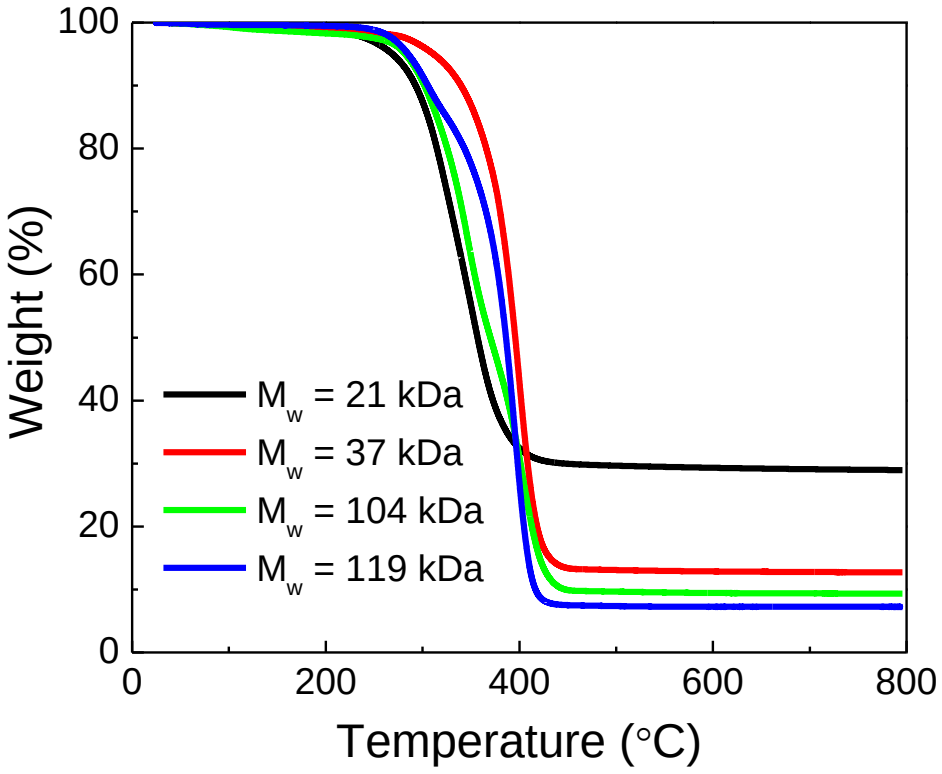

Figure 5.2 TGA plots of SiO_2-POEOMA macroinitiator and SiO_2-P(OEOMA-b-sty) nanoparticles.

hybrid nanoparticles with POEOMA homopolymer brushes was weak suggesting poorer order resulting from the weaker steric repulsion and volume-filling constraint between the hybrid nanoparticles due to the shorter brushes. With increasing molecular weight of the polymer brushes, the location of the primary scattering peak (q_1*) (and the secondary peak at q_2*)

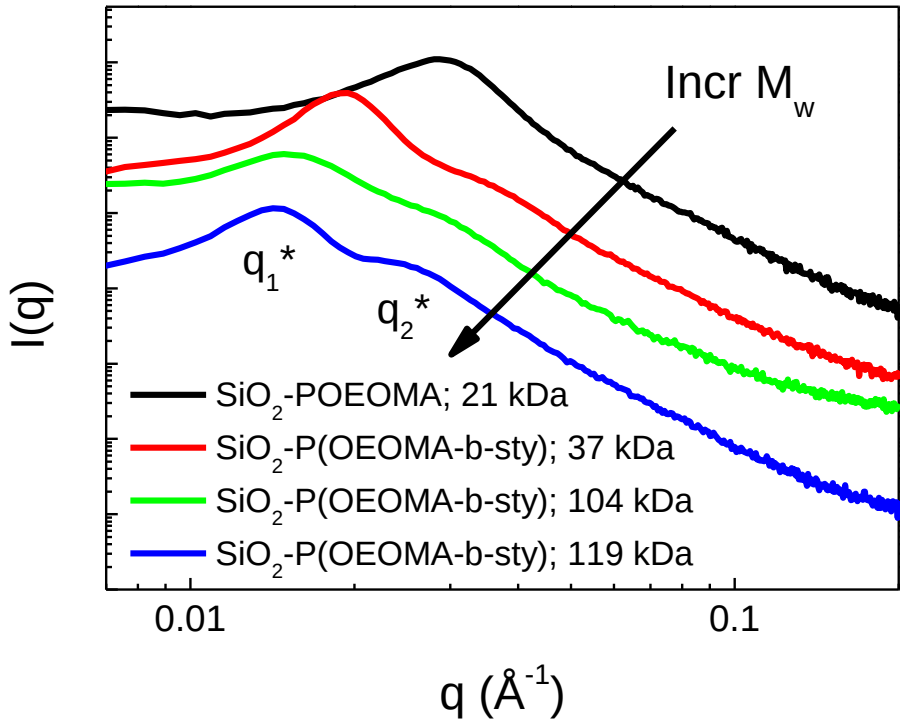

Figure 5.3 SAXS data for hybrid nanoparticles with varying molecular weight and fixed grafting density of the grafted polymer brushes.

shifted to smaller q-values, implying increased distance between silica cores due to the longer polymer brushes. Since the hybrid nanoparticles melts did not contain any solvents, the surface-to-surface distance between silica cores is a reasonable measure to estimate the height of polymer brushes grafted on the silica nanoparticles. From the melt-state scattering data, the center-to-center distance, d, between hybrid nanoparticles formula was calculated as

$$d = a\left(\frac{2\pi}{q_1^*}\right), \quad (3)$$

where, a is 1.22 for the FCC and HCP lattice. Additionally, the surface-to-surface distance between silica cores, h, can be obtained by subtracting the diameter of silica core (15.5 ± 0.9 nm, measured from DLS) from d. Although the POEOMA homopolymer grafted nanoparticles presented weak secondary peak (q_2^*), we estimated their size from the lattice parameter of FCC or HCP structures as well.

To understand the interaction of different solvents with the hybrid nanoparticles, the swelling behavior of the grafted polymer brushes in water, toluene and *n*-hexane were examined. Figure 5.4 shows the change in polymer brush height, estimated from SAXS measurements, as a function of solvent concentration. As increase the amount of solvent the scattering peaks of the SAXS plot shift to the low q value, indicating the increase of inter-particle distance (h) (Figure 5.4a). As presented in Figure 5.4b, polymer brushes of SiO_2-POEOMA nanoparticles were swollen by water and toluene. Since their swelling extent increased with increasing polarity of the solvents, their hydrophilicity is predominant compared to hydrophobicity. However, after PS chain extension, the swelling was induced by toluene but not by water or hexane. This suggests that the nature of PS, which interacts with neither hexane nor water, became dominant due to the PS chain extension in spite of the presence of hydrophilic POEOMA components.

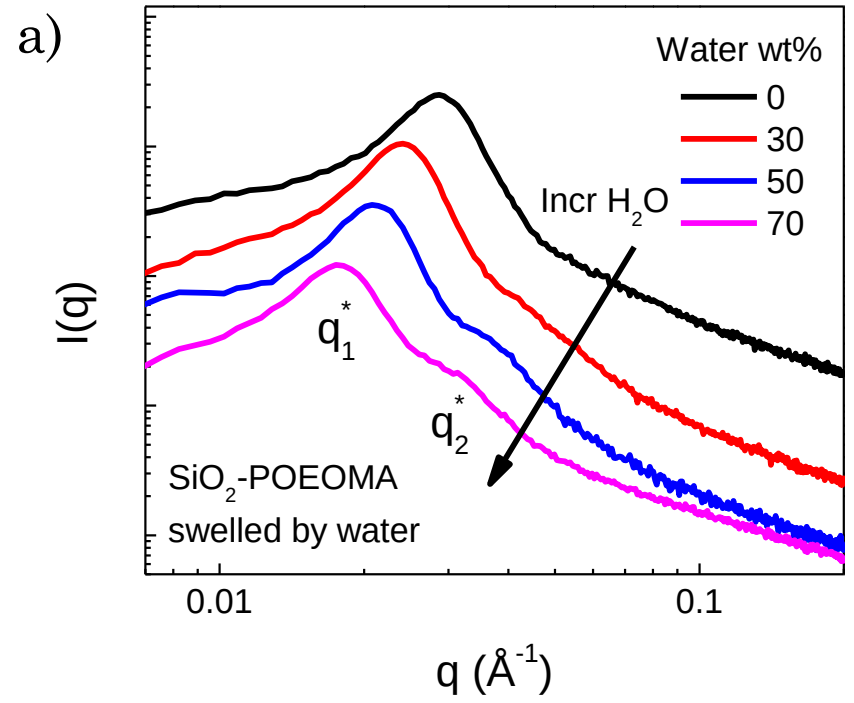
a)
Water wt%
0
30
50
70
Incr H2O
I(q)
q1*
q2*
SiO2-POEOMA
swelled by water
0.01
0.1
q (Å-1)

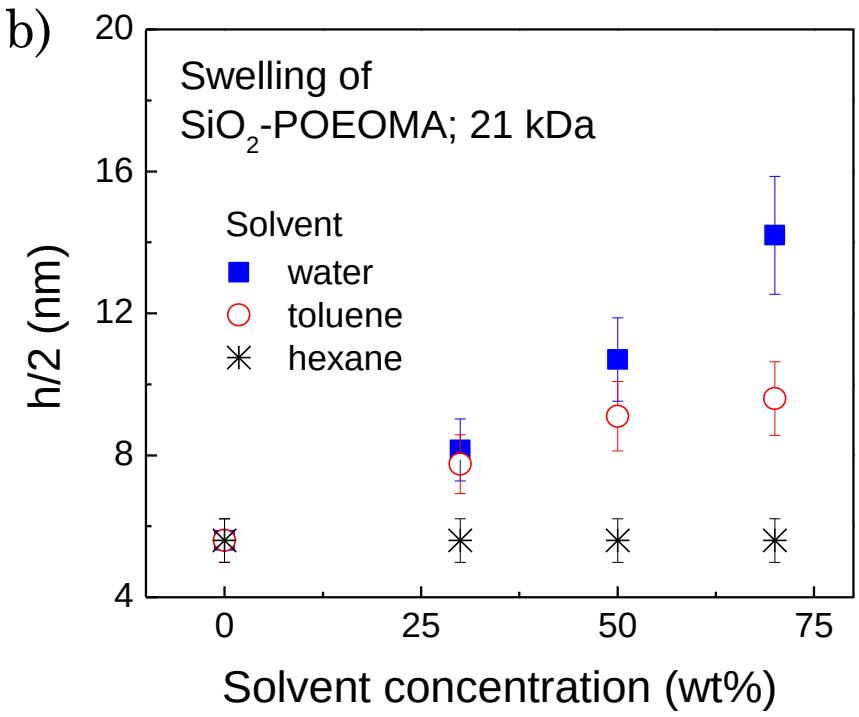
b)
Swelling of
SiO2-POEOMA; 21 kDa
Solvent
water
toluene
hexane
h/2 (nm)
20
16
12
8
4
0
25
50
75
Solvent concentration (wt%)

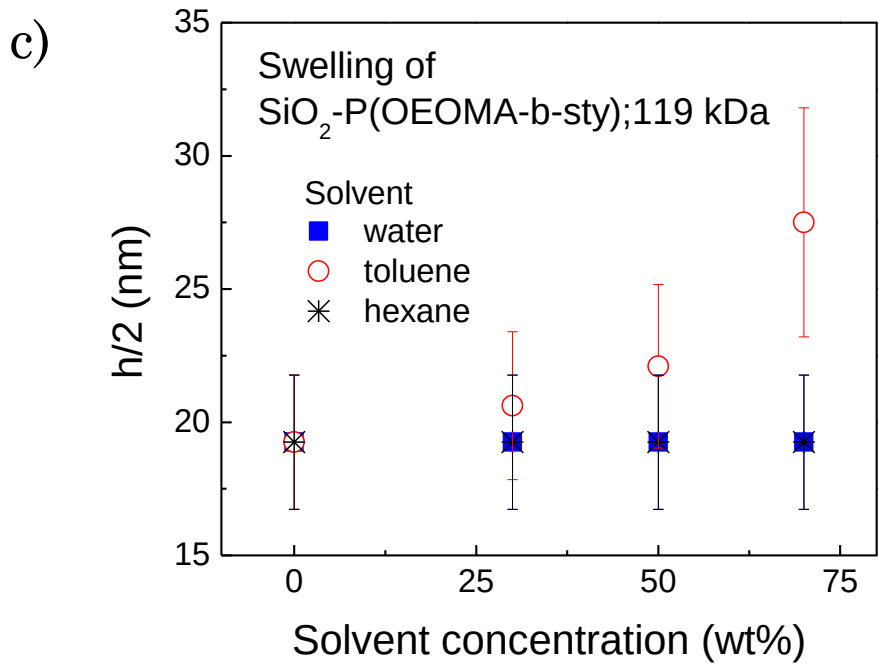

Figure 5.4 a) SAXS data demonstrating the swelling of the SiO_2-POEOMA by water. The polymer brush height ($h/2$) of b) SiO_2-POEOMA and c) SiO_2-P(OEOMA-b-sty) as a function of solvent concentration.

To study the interfacial activity of hybrid nanoparticles, toluene – water interfacial tension reduction, induced by the segregation of various hybrid nanoparticles and untethered free polymers to the toluene – water interface, was measured as a function of time using pendant drop method. All Hybrid nanoparticles and free polymers were dissolved in toluene before the interfacial tension measurement and the concentrations of the nanoparticles in toluene were used as the concentrations presented in this study. Figure 5.5 shows that SiO_2-POEOMA reduced the toluene – water interfacial tension from ~ 30 mN/m to ~ 5 mN/m. SiO_2 nanoparticles grafted with radical

initiator and SiO_2-PS did not reduce the interfacial tension with any appreciable amount, which indicates their weak adsorption on the toluene – water interface. However, toluene – water interfacial tension reached extremely low value (< 0.2 mN/m) with SiO_2-P(OEOMA-b-sty). As we expected, the amphiphilic nature of the block copolymer brushes induced dramatic improvement in the interfacial activity of the nanoparticles. These experimental results imply that the amphiphilicity of the block copolymer brushes were the key factor to reduce the oil – water interfacial tension as theoretical and simulational studies predicted since both hydrophilic SiO_2-POEOMA and hydrophobic SiO_2-PS did not reduce the interfacial tension with such a large extent.[35,42,43] Although the rate of the interfacial tension reduction was faster with the homopolymer grafted nanoparticles, both the copolymer grafted nanoparticles needed comparatively more time to reach to their saturated interfacial tension values. We assume that polystyrene outer corona of SiO_2-P(OEOMA-b-sty) nanoparticles originally made their week adsorption on toluene – water interface similar to that of SiO_2-PS nanoparticles, and the weak adsorption hindered interfacial tension reduction. This PS-dominant surface nature of the SiO_2-P(OEOMA-b-sty) nanoparticles is supported by the swelling tests shown in Figure 5.4. However, unlike SiO_2-PS nanoparticles which barely reduce the interfacial tension, P(OEOMA-b-sty) brushes can match their hydrophilic and hydrophobic components to water and toluene phase respectively through

conformational rearrangements over time. We noted that although dry SiO_2-P(OEOMA-b-sty) nanoparticle melts did not present affinity to water in swelling tests, their toluene dispersion, whose brushes were stretched, might have enough freedom to be rearranged toward water phase. Therefore, SiO_2-P(OEOMA-b-sty) nanoparticles reduce toluene – water interfacial tension with slower rate compared to SiO_2-POEOMA nanoparticles. Interestingly, at the low interfacial tension the nanoparticles formed thin films at oil – water interface and made anisotropically deformed pendant droplets (Figure 5.5b).

In order to verify the parameters determining the interfacial tension reduction efficiency, toluene – water interfacial tensions were observed with various concentrations of the hybrid nanoparticles as presented in Figure 5a. The rate of the interfacial tension reduction increased with increasing nanoparticle concentrations due to the more diffusion of the nanoparticles toward toluene – water interface (Figure 5.6). The interfacial tension reduction was not observed below certain concentration of the nanoparticles, which is defined as a critical particle concentration. The critical hybrid particle concentration was modified based on weight of silica core (*i.e.*, number-based conversion of the critical hybrid particle concentration) and this modified concentration named as critical core concentration. The critical particle concentration of the hybrid nanoparticles did not show a correlation with particle properties. In other hand, the critical core concentration of the

hybrid nanoparticles decreased with increasing their hydro dynamic diameter as we reported in previous chapter (table 5.2).

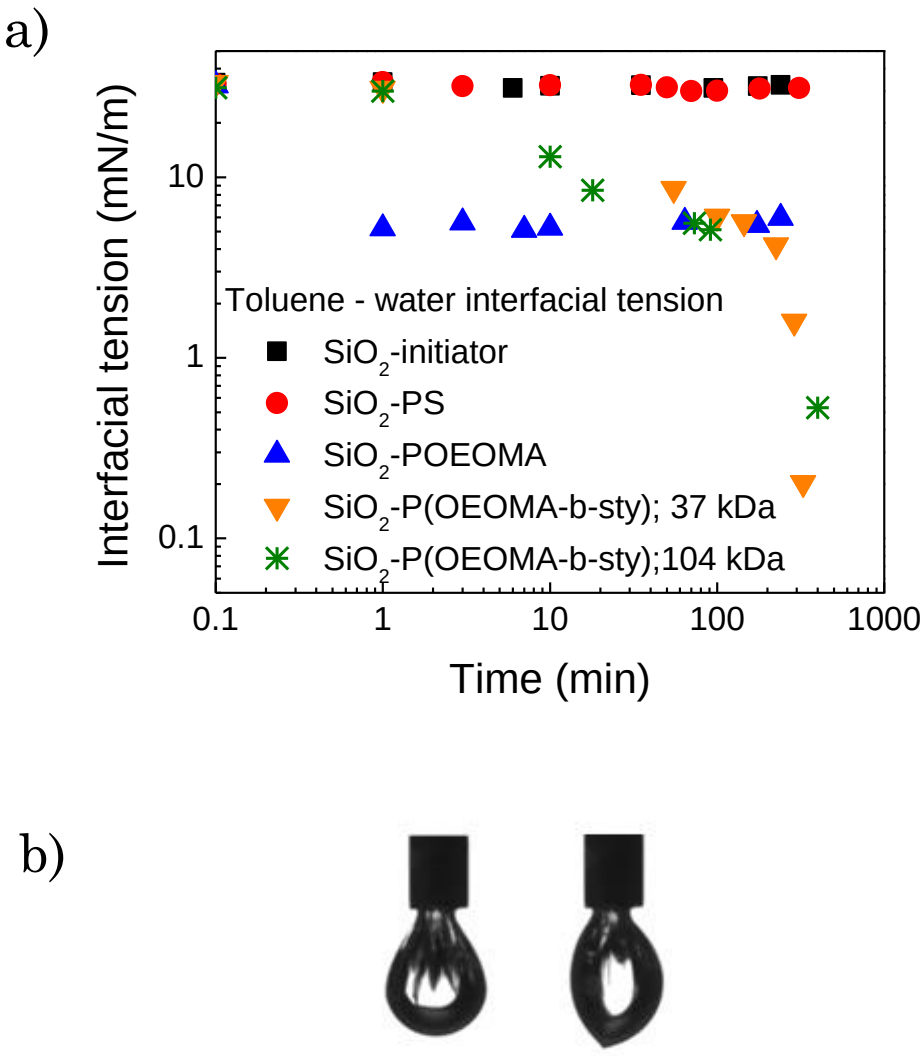

Figure 5.5 a) Toluene – water interfacial tension with hybrid nanoparticles as a function of time, b) Thin films of SiO_2-P(OEOMA-b-sty) hybrid nanoparticles at low interfacial tension less than 0.5 mN/m.

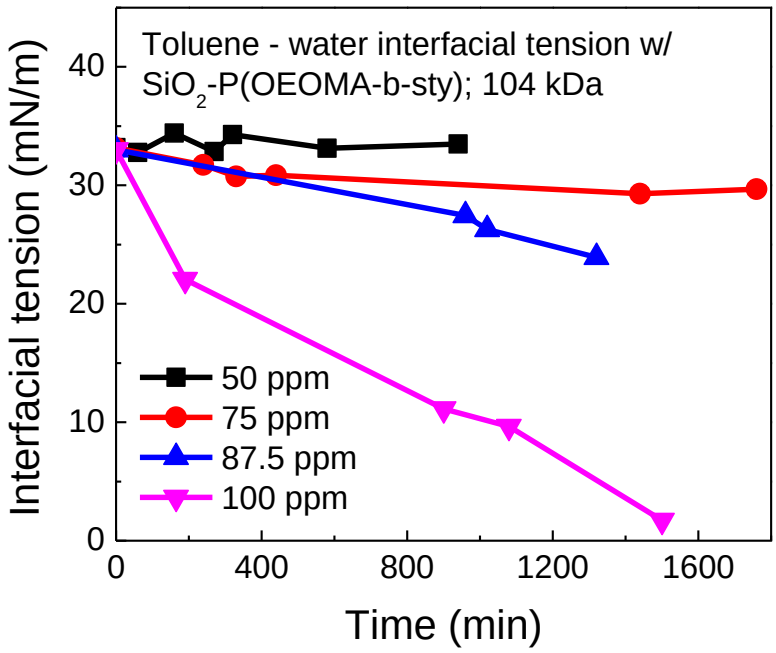

Figure 5.6 a) Change of toluene – water interfacial tension as a function of time with SiO_2-P(OEOMA-b-sty) (M_w = 104 kDa).

Table 5.2 Critical core concentration of the hybrid particles in toluene – water system

	M_w (kDa)	Hydrodynamic diameter in toluene (nm)	Critical particle concentration (ppm)	Critical core concentration (ppm)
SiO_2-POEOMA	21	69±1	75±25	2.2±0.7
SiO_2-P(OEOMA-b-sty)	37	81±2	87.5±12.5	1.6±0.2
	104	146±4	78.8±3.8	0.25±0.01
	119	155±4	87.5±12.5	0.23±0.03

Oil – water emulsions with 1:1 oil – water volume ratio were formed using toluene as an oil-like phase, deionized water (DIW) as a water phase, and SiO_2-P(OEOMA-b-sty) hybrid nanoparticles as emulsifiers. SiO_2-POEOMA hybrid nanoparticles whose chains were not extended with PS were used as reference to compare their emulsification efficiency. Toluene, DIW, and hybrid nanoparticles mixtures were mixed using a vortex mixer for 60 sec at the max speed to form oil – water emulsions. Then, the amounts of emulsion phases and the average sizes of the emulsion droplets obtained from the images taken by optical microscopy were studied. The SiO_2-P(OEOMA-b-sty) nanoparticles successfully formed toluene – water emulsions in spite of their slow interfacial tension reduction rate presented in Figure 5.5a. The shear force from the vortex mixing might provide enough energy for the P(OEOMA-b-sty) brushes to be rearranged at the toluene – water interface and the stable emulsions could be formed. The dispersed emulsion droplets were settled down when the SiO_2-P(OEOMA-b-sty) nanoparticles were used as emulsifier while emulsion droplets were situated above the water phase when the SiO_2-P(OEOMA-b-sty) nanoparticles were used. This implies water-in-oil emulsions were created by SiO_2-P(OEOMA-b-sty) nanoparticles and oil-in-water emulsions were created by SiO_2-POEOMA nanoparticles. Since the hydrophobicity of an emulsifier tends to make water-in-oil emulsions, the water-in-oil emulsions made by SiO_2-P(OEOMA-b-sty) nanoparticles as

emulsifiers reflected their increased hydrophobicity induced by adding hydrophobic PS chains to hydrophilic POEOMA brushes.[89]

Optical micrographs of the toluene – water emulsions shows that comparatively uniform emulsion droplets were formed by SiO_2-POEOMA nanoparticles (Figure 5.7a-b) whereas polydispersed emulsion droplets were formed by all three SiO_2-P(OEOMA-b-sty) nanoparticles (Figure 5.7c-h) for both two different nanoparticle concentrations. As presented in Figure 5.8, mean diameters of emulsion droplets decreased by increasing nanoparticle concentration since more toluene – water interfacial area could be covered by nanoparticles when their concentration was higher. Moreover, SiO_2-P(OEOMA-b-sty) nanoparticles made averagely smaller emulsion droplets than emulsion droplets made by SiO_2-POEOMA nanoparticles. It is known that the initial diameter of the oil – water emulsion droplets decreased by decreasing oil – water interfacial tension. Therefore, low interfacial tension achieved by SiO_2-P(OEOMA-b-sty) nanoparticles possibly influenced on reducing the size of the emulsion droplets.

For the further investigation of toluene – water emulsions made by hybrid nanoparticles, size distribution of the emulsion droplets was plotted (Figure 5.9). In many systems which are composed of discrete entities such as emulsion droplets[90] and broken solid particles[91], droplet size distribution can be commonly described by the probability density function, $p(a)$, of a log-normal distribution, which can be expressed as

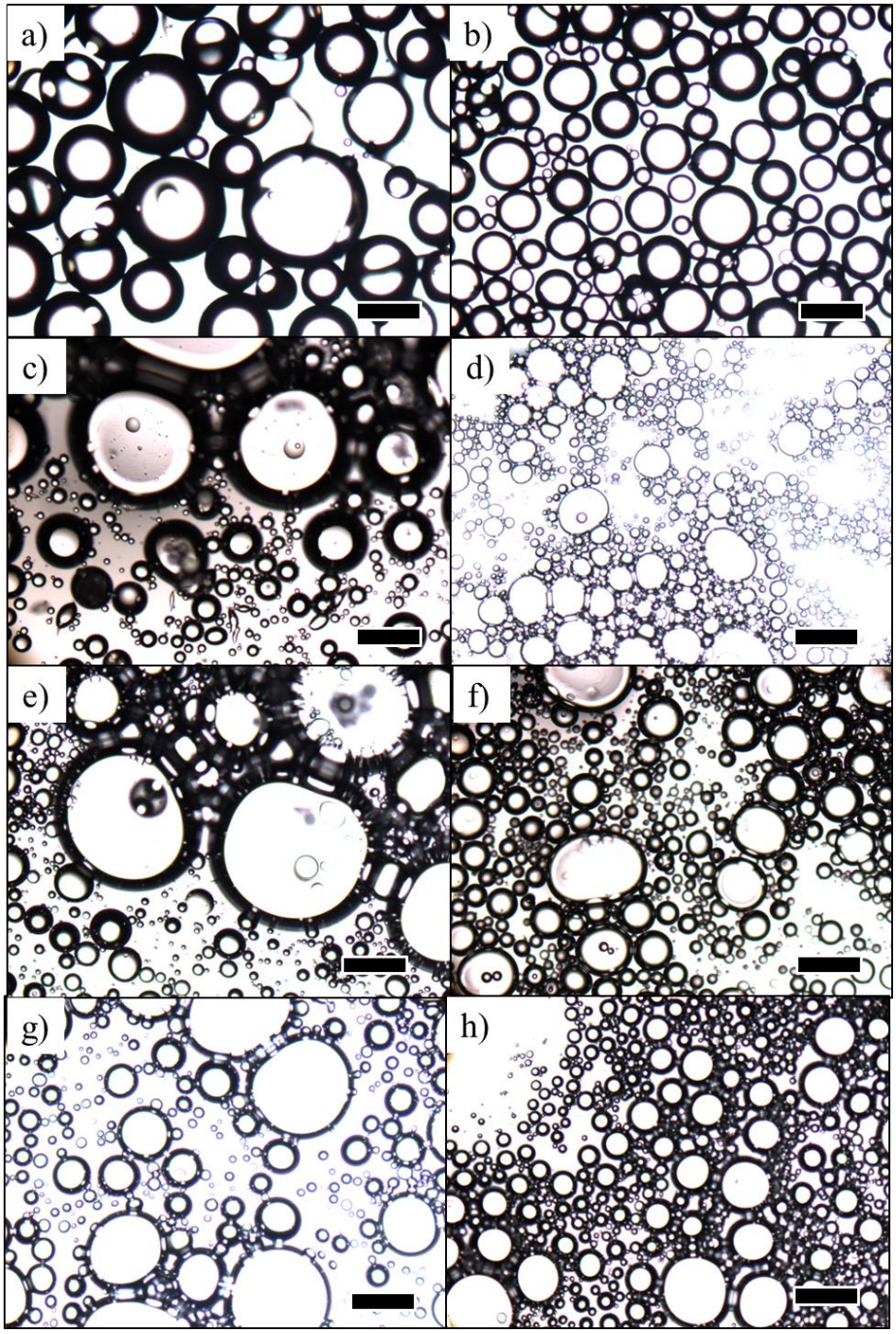

Figure 5.7 Optical micrographs of toluene – water emulsions formed by a) 500 ppm b) 2000 ppm SiO_2-POEOMA, c) 500 ppm d) 2000 ppm SiO_2-P(OEOMA-b-sty); 37 kDa, e) 500 ppm f) 2000 ppm SiO_2-P(OEOMA-b-sty); 104 kDa, and g) 500 ppm h) 2000 ppm SiO_2-P(OEOMA-b-sty); 119 kDa. Micrographs were taken 10 min after the emulsification. Scale bars indicate 200 μm.

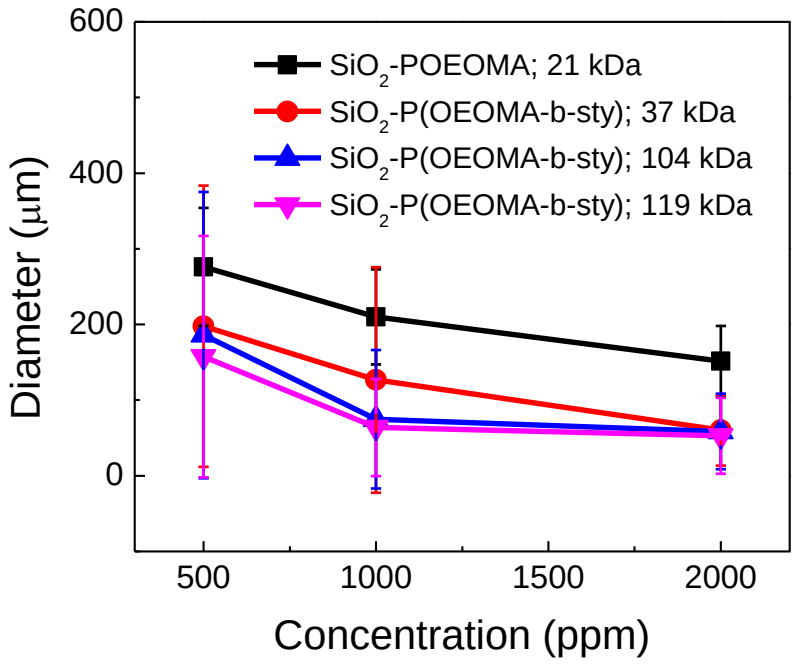

Figure 5.8 Mean diameters of toluene – water emulsion droplet 10 min after the emulsification as a function of the hybrid nanoparticle concentration.

$$p(a) = \frac{1}{2a\sigma_g\sqrt{2\pi}} e^{-\frac{(\ln 2a - \ln d_g)^2}{2\sigma_g^2}}, \qquad (4)$$

where, a is the droplet radius, σ_g is the geometric standard deviation, and d_g is the geometric mean droplet size.[92] The droplet size distribution of the emulsions made by SiO_2-P(OEOMA-b-sty) nanoparticles are well described by this log-normal distribution and the experimental data are well fitted by theoretical curves(Figure 5.9c-d). However, the log-normal distribution was failed to describe emulsions made by SiO_2-POEOMA nanoparticles. Their droplet size distribution rather follows Lifshitz-Slyozov-Wagner (LSW) theory, which expresses the droplet distribution induced by Ostwald ripening (Figure

5.9a-b). Therefore, we can conjecture that Ostwald ripening is dominant for toluene – water emulsions formed by SiO_2-POEOMA nanoparticles and droplet size becomes comparatively uniform due to the diffusion of the smaller droplets into the larger droplets. In contrast, amphiphilic SiO_2-P(OEOMA-b-sty) nanoparticles, which are strongly adsorbed at toluene – water interface, provide enough dilatational modulus and suppress Ostwald ripening. From this analysis, we can expect the improved stability of the emulsions made by SiO_2-P(OEOMA-b-sty) nanoparticles.

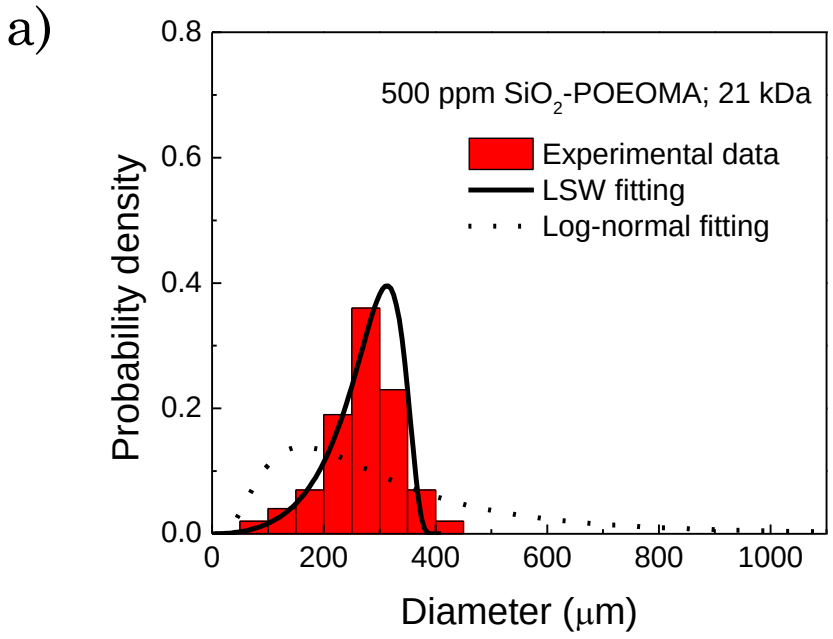

b)

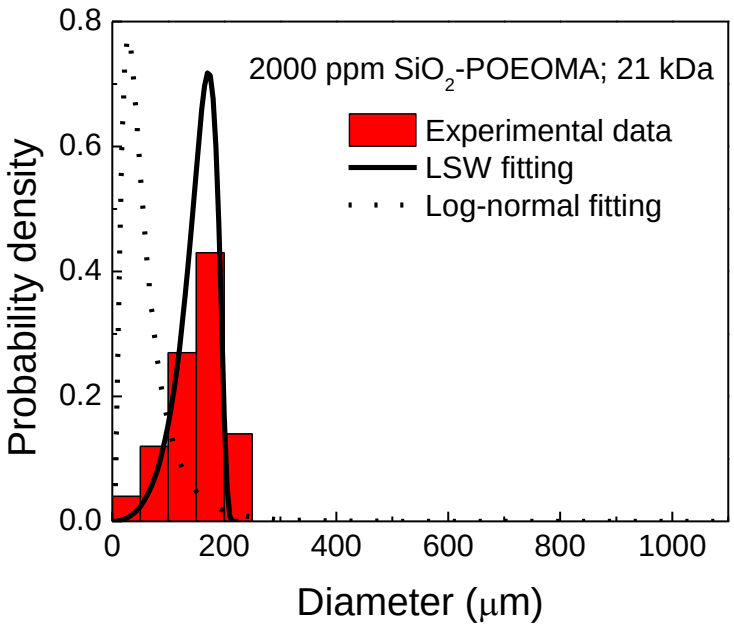
2000 ppm SiO2-POEOMA; 21 kDa
Experimental data
LSW fitting
Log-normal fitting
Probability density
Diameter (μm)
0.0
0.2
0.4
0.6
0.8
0
200
400
600
800
1000

c)

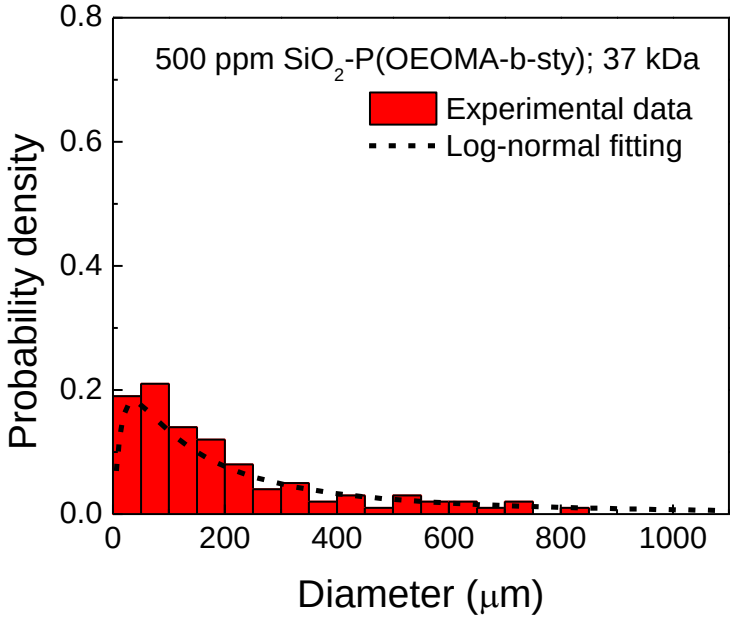
500 ppm SiO2-P(OEOMA-b-sty); 37 kDa
Experimental data
Log-normal fitting
Probability density
Diameter (μm)
0.0
0.2
0.4
0.6
0.8
0
200
400
600
800
1000

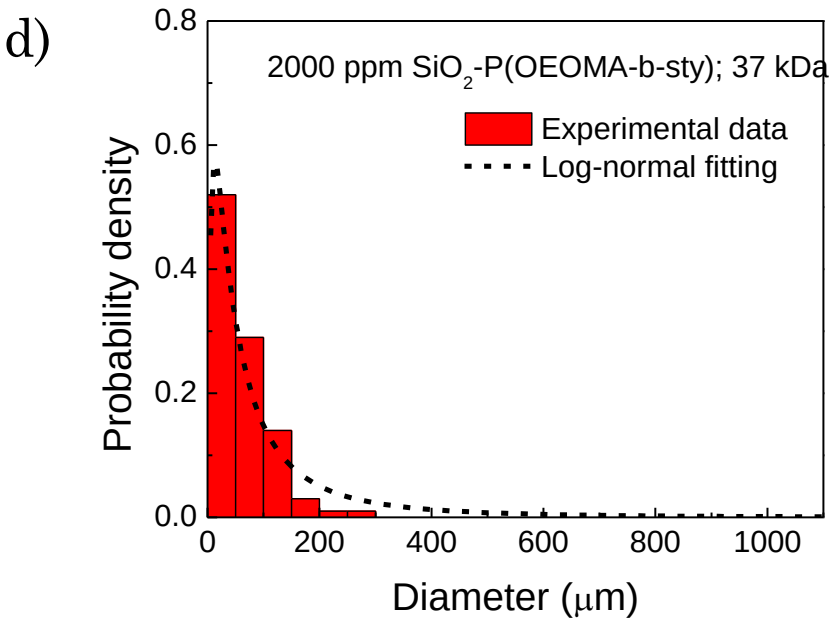

Figure 5.9 Droplet size distribution of toluene – water emulsions formed by a) 500 ppm, b) 2000 ppm SiO_2-POEOMA, and c) 500 ppm, d) 2000 ppm SiO_2-P(OEOMA-b-sty); 37 kDa.

In order to compare the stabilities of the emulsions formed with hybrid nanoparticles, the emulsification index, EI = (height of emulsion layer)/(total height of the mixture) × 100, was studied (Figure 5.10).[93] The height of emulsion layer and the total height of the mixture were measured using an image analyzing software from the images of toluene – water emulsions taken by a digital camera. Initially, SiO_2-POEOMA nanoparticles produced same or more volume of emulsion layer compared to SiO_2-P(OEOMA-b-sty) nanoparticles. However, the emulsions made with SiO_2-P(OEOMA-b-sty) nanoparticles were more stable and their emulsification indexes did not change in any appreciable extent 10000 min after the emulsification although

the emulsions made with SiO_2-POEOMA nanoparticles were dismissed and their emulsification index decreased rapidly. Moreover, emulsification indexes for SiO_2-P(OEOMA-b-sty) nanoparticles with various brush molecular weights were almost identical, so the effect of the polymer brush length or POEOMA/PS components ratio on the emulsion stability was limited in this study. This suggests that amphiphilicity of SiO_2-P(OEOMA-b-sty) nanoparticles mainly influence the improvement of their emulsification efficiency and emulsion stabilizing capacity

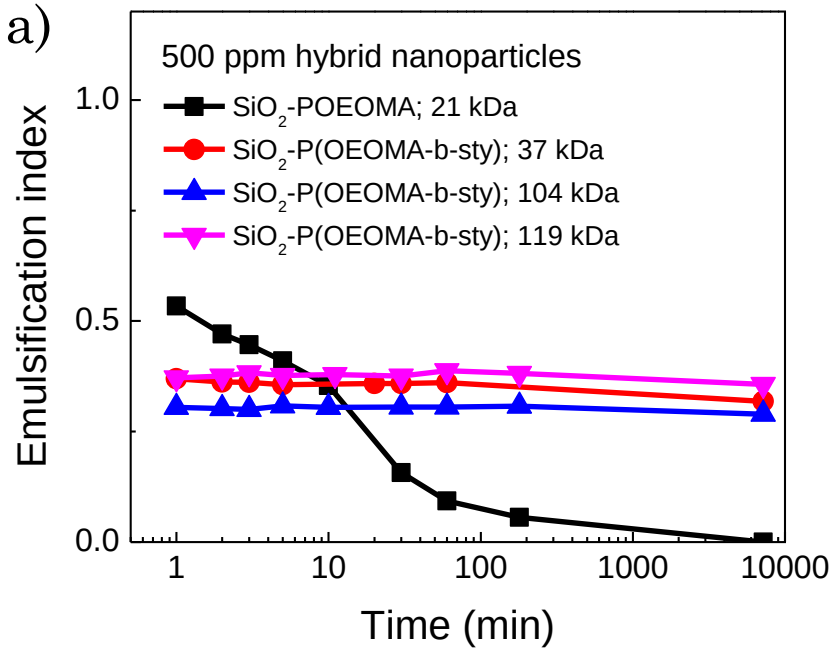

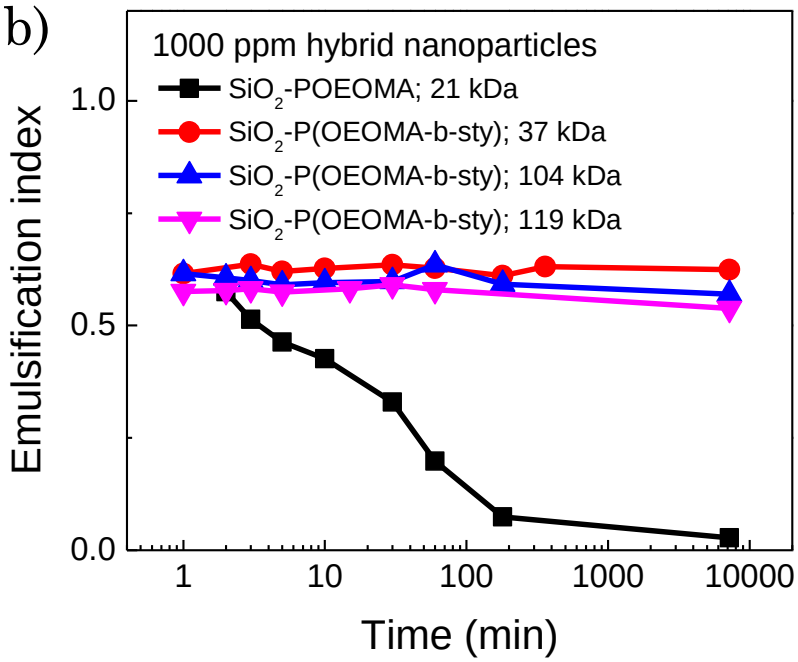

Figure 5.10 a) emulsification index of toluene – water emulsion formed by 500 ppm, and b) emulsification index of toluene – water emulsion formed by 1000 ppm hybrid nanoparticles as a function of time.

5.4 Conclusions

We have investigated the interfacial activity and emulsion stabilizing capacity of silica nanoparticles, grafted with amphiphilic block copolymers by surface initiated atom transfer living radical polymerization, at oil – water interface. Successful chain extension of the hydrophobic polymers (PS) from hydrophilic polymer (POEOMA) ends and synthesis of block copolymer (POEOMA-b-PS) brushes were confirmed by SEC measurements. Based on the two scattering peaks from the small angle X-ray scattering measurements of the solvent-free hybrid nanoparticle melt, their face

centered cubic or close packed hexagonal structure was estimated. Moreover, from the structural geometry and the value of the first scattering peak, diameters of the hybrid nanoparticle melts were calculated. Toluene – water interfacial tension, which was measured by the pendant drop method, was significantly reduced by SiO_2-P(OEOMA-b-sty) nanoparticles and reached to ~0.2 mN/m, whereas SiO_2-POEOMA reduced it to ~5 mN/m from 30 mN/m and SiO_2-PS did not reduce it. The critical core concentration, the number-based concentration of the hybrid nanoparticles where the interfacial tension reduction occurred first, was correlated to the hydrodynamic diameter of SiO_2-P(OEOMA-b-sty) nanoparticles as we reported previously using SiO_2-POEOMA nanoparticles.

Using the hybrid nanoparticles as emulsion stabilizers, toluene – water emulsions were made and their stability was observed. A larger volume of the emulsions was formed by SiO_2-P(OEOMA-b-sty) nanoparticles with smaller droplet size compared to the emulsions formed by SiO_2-POEOMA nanoparticles. Emulsion particle size distribution analysis suggested Ostwald ripening was successfully suppressed by applying SiO_2-P(OEOMA-b-sty). The emulsion stability was studied using emulsification index, % ratio of emulsion layer height to total height of the mixture, and the emulsions made by SiO_2-P(OEOMA-b-sty) were stable for more than 10,000 min whereas the emulsions made by SiO_2-POEOMA were dismissed rapidly.

Behavior of the hybrid nanoparticles at the oil – water interface of the emulsions were visually studied using Cryo-scanning electron microscopy. Micrographs of the emulsions revealed that the hybrid nanoparticles tended to compensate the void in the interfacial area by forming bridge-like structures at a low nanoparticle concentration. Additionally, segregation of the nanoparticles at the oil – water interface was confirmed with Cryo-scanning electron microscopy.

Chapter 6 Scanning electron microscopy (SEM) of oil – water emulsions

6.1 Introduction

Arrangement of nanoparticles and their morphology at oil – water interface are crucial factors determining the stability of Pickering emulsions, which are the emulsions stabilized by small particles such as nanoparticles.[34,35] However, common microscopic method such as optical microscopy and scanning electron microscopy cannot provide proper measures to study the fundamental interactions of the nanoparticles situated at the oil – water interface due to the difficulty in sample preparations which should not deform the emulsion droplets and detach the nanoparticles from the interface.

In the life science area such as biological, pharmaceutical, and food science, the cryogenic scanning electron microscopy (Cryo-SEM) have been widely used.[94-96] The Cryo-SEM is an excellent way to visualize and quantitatively analyze the oil – water emulsion system containing sub-micron size particle-based emulsifiers. The surface nature of the emulsion droplets, the droplet size distributions, and the segregating behavior of the solid particles at the oil – water interface can be directly imaged by Cryo-SEM measurements. Instant freezing of the oil – water emulsion samples makes it possible to maintain their morphology and other important structural

information. By keeping the sample frozen on a cold stage in the electron microscope, it is possible to visualize the emulsion or suspension samples and also to get compositional information from the x-rays emitted as the electron beam strikes the sample.[97] For example, the core-shell structure of the microgels and their interfacial arrangement at oil – water interface was observed using Cry-SEM measurements.[98] The quantitative measurements of the core diameter and inter-particle distance of the microgels at the oil – water interface were also conducted from the Cryo-SEM micrographs. The packing aspect of the ellipsoidal polystyrene particles and the formation of their monolayer at the oil – water interface were also visually reported using Cryo-SEM measurements.[99]

In this chapter, the interfacial behavior of polymer grafted silica nanoparticles was studied using the Cryo-SEM measurements. Interfacial characteristics of hexane – water emulsions formed by 500 ppm and 2000 ppm SiO_2-POEOMA nanoparticles were compared first. Then toluene – water emulsions formed by SiO_2-P(OEOMA-b-sty) nanoparticles and the emulsion hardening phenomenon were investigated.

6.2 Methodology

6.2.1 Materials

Colloidal silica nanoparticles (MIBK-ST, effective diameter ~15 nm, 30~31 wt% silica in methyl isobutyl ketone) were acquired from Nissan

Chemical. Allyl 2-bromo-2-methylpropionate (98%, Sigma-Aldrich), chlorodimethylsilane (98%, Sigma-Aldrich), 5% platinum on activated charcoal (Sigma-Aldrich), Hexamethyldisilazane (HMDS, 99.9%, Sigma-Aldrich), tetrahydrofuran (THF, 99.9+%, Sigma-Aldrich), copper(I) bromide (98%, Sigma-Aldrich), copper(II) bromide (99%, Sigma-Aldrich), anisole (anhydrous, 99.7%, Sigma-Aldrich), N,N,N′,N″,N″-Pentamethyldiethylene-triamine (PMDETA, 99%, Sigma-Aldrich), 2,2'-bipyridyl (bpy, 99+%, Sigma-Aldrich) methanol (99.8%, Mallinckrodt), hydrofluoric acid (48~51%, VWR), and magnesium sulfate (97+%, Sigma-Aldrich) were used as received. Toluene (99.5%, Macron) and *n*-hexane (98.5%, Macron), used for the interfacial tension measurements, was purified by passing through a basic alumina column three times. Oligo(ethylene oxide) monomethyl ether methacrylate (OEOMA, Mn=300, Sigma-Aldrich) and styrene monomer (99+%, Sigma-Aldrich) was passed through the column which was packed with inhibitor remover (for monomethyl ether hydroquinone, Sigma-Aldrich) and neutral alumina (Sigma-Aldrich) to remove inhibitors.

6.2.2 Synthesis of hybrid nanoparticles

Hydrophilic poly(oligo(ethylene oxide) monomethyl ether methacrylate) (POEOMA) brushes, and amphiphilic copolymer brushes of POEOMA and polystyrene (PS) were grafted from 15 nm diameter silica nanoparticles using the surface initiated atom transfer radical polymerization (ATRP) method

with similar procedure presented in previous chapters (Chapter 4, 5). The properties of polymer brushes were shown in table 6.1.

Table 6.1 Polymer-grafted silica nanoparticles for Cryo-SEM

Sample	M_w (kDa)	M_w/M_n	Grafting density (chains/nm^2)	Number of polymer chains per particle	d[1)] (nm)	D[2)] (nm)
SiO_2-POEOMA	21	1.4	0.57±0.04	487±54	27±1	69±1
SiO_2-P(OEOMA-b-sty)	104	1.9	0.62±0.05	436±50	51±2	146±4

1) Center-to-center distance of silica nanoparticles measured by SAXS in bulk melt state of the polymer
2) Hydrodynamic size of dispersed hybrid nanoparticles measured by DLS in toluene

6.2.3 Cryo-SEM measurements

Cryo-SEM (Hitachi 4800 high-resoluion SEM) was used to visualize the behavior of the nanoparticles in toluene – water emulsion. Figure 6.1a shows brief procedure of Cryo-SEM measurement. Continuous emulsion phase was sampled and instantly frozen under liquid nitrogen atmosphere. The frozen emulsion phase was crushed by blade and exposed cross section was investigated using electron microscope (Figure 6.1b). Frozen cross section from the Cryo-SEM measurement shows the morphology of the nanoparticles dispersed in bulk phase or segregated at oil – water interface without

deformations which possibly occur by sample treatment from non-Cryo measurements.

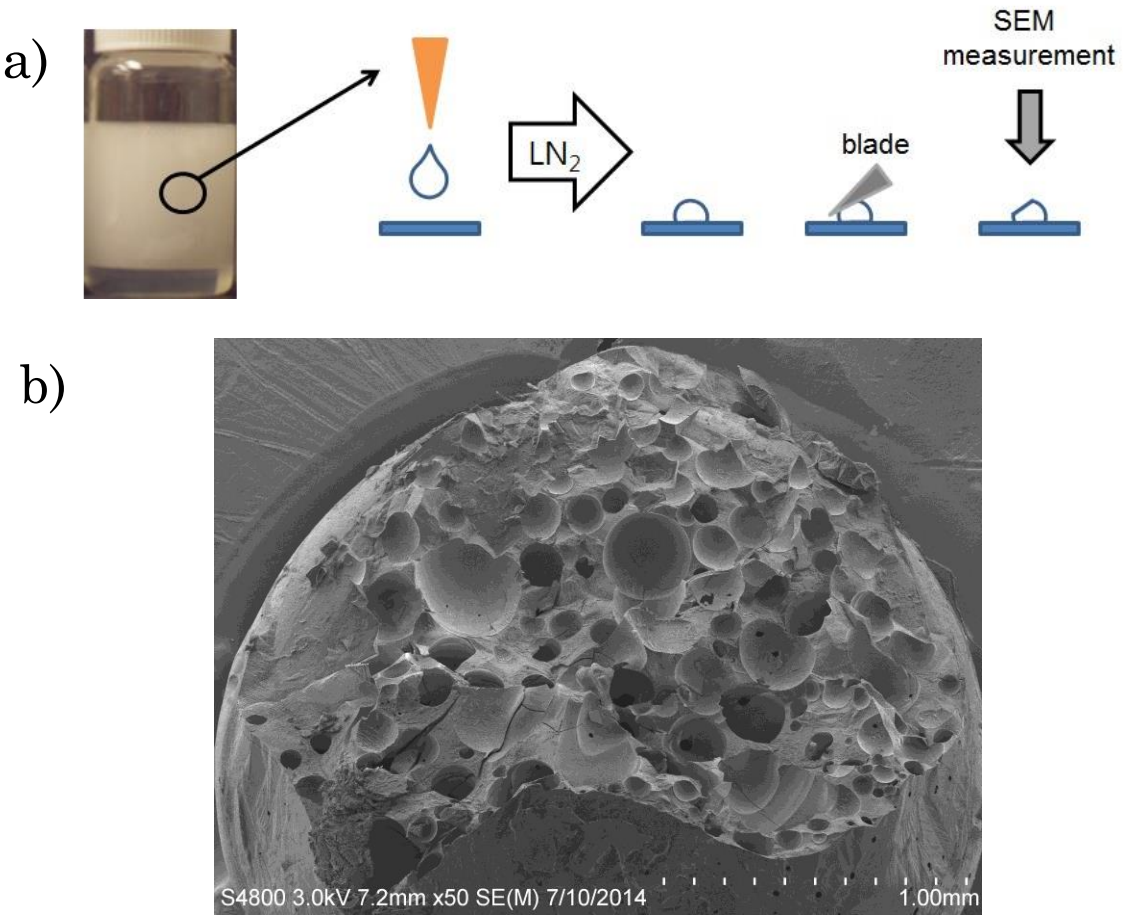

Figure 6.1 a) a sample preparation procedure for Cryo-SEM measurements, b) micrograph of the crushed frozen emulsion sample.

6.3 Results and discussions

First, the interfacial behavior of SiO_2-POEOMA nanoparticles at hexane – water interface was studies. In order to observe difference in morphology of oil – water interface, two different hybrid nanoparticle concentrations (500 ppm 2000 ppm) were used to from emulsions. Figure 6.2

shows Cryo – SEM micrographs of oil-in-water emulsions formed with 1:1 volume ratio of deionized water, where 500 ppm and 2000 ppm SiO_2-POEOMA (M_w = 21 kDa) nanoparticles were pre-dissolved, to hexane. Both micrographs show bulk water phase and hexane – water interface which were exposed by fracturing. Oil – water interfacial layer of the emulsion formed with 2000 ppm nanoparticles shows comparatively smooth surface and emulsion droplets seem to be fully covered with nanoparticles (Figure 6.2a). On the other hand, Figure 6.2b shows the incomplete coverage of nanoparticles at toluene – water interface. Haase *et al*. reported Cryo-SEM measurements of oil – water pickering emulsions stabilized with hard spherical silica nanoparticles which also showed incomplete coverage with some unoccupied regions at oil – water interface.[100] Unlike the previously reported interfacial layer of hard spherical particles, the hybrid nanoparticles formed stretched networks and made up for vacancies at the toluene – water interfacial area even if their concentration was not enough to cover the whole emulsion droplet surface. The cross section image of the hybrid nanoparticle interfacial layer of the emulsion formed with 2000 ppm SiO_2-POEOMA nanoparticles with 104 kDa brush molecular weight (Figure 6.2c) shows that the hexane-faced surface of the nanoparticle layer was comparatively clean, but some aggregates were observed at its water-faced surface. Since the POEOMA polymer brushes were hydrophilic and have poor hexane solubility,

the hybrid nanoparticles tended to avoid the hexane phase and gather at water-side.

The interfacial behavior of SiO_2-P(OEOMA-b-sty) nanoparticles at toluene – water interface was also studied by Cryo-SEM measurements. Figure 6.3 shows Cryo – SEM micrographs of oil-in-water emulsions formed with 1:1 volume ratio of toluene, where 500 ppm and 2000 ppm SiO_2-P(OEOMA-b-sty) nanoparticles with 104 kDa brush molecular weight were pre-dissolved, to deionized water. Both micrographs show bulk toluene phase and toluene – water interface which were exposed by fracturing. At the

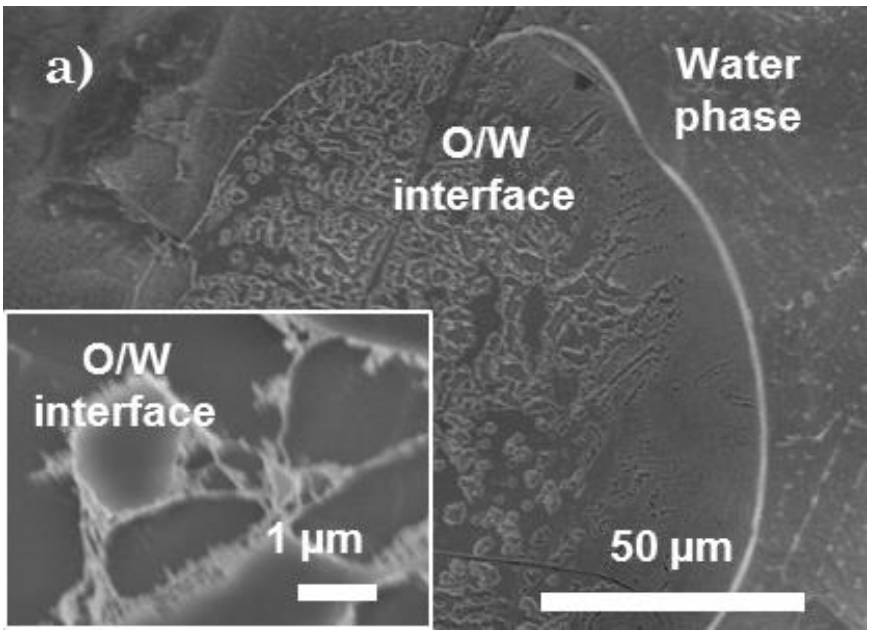

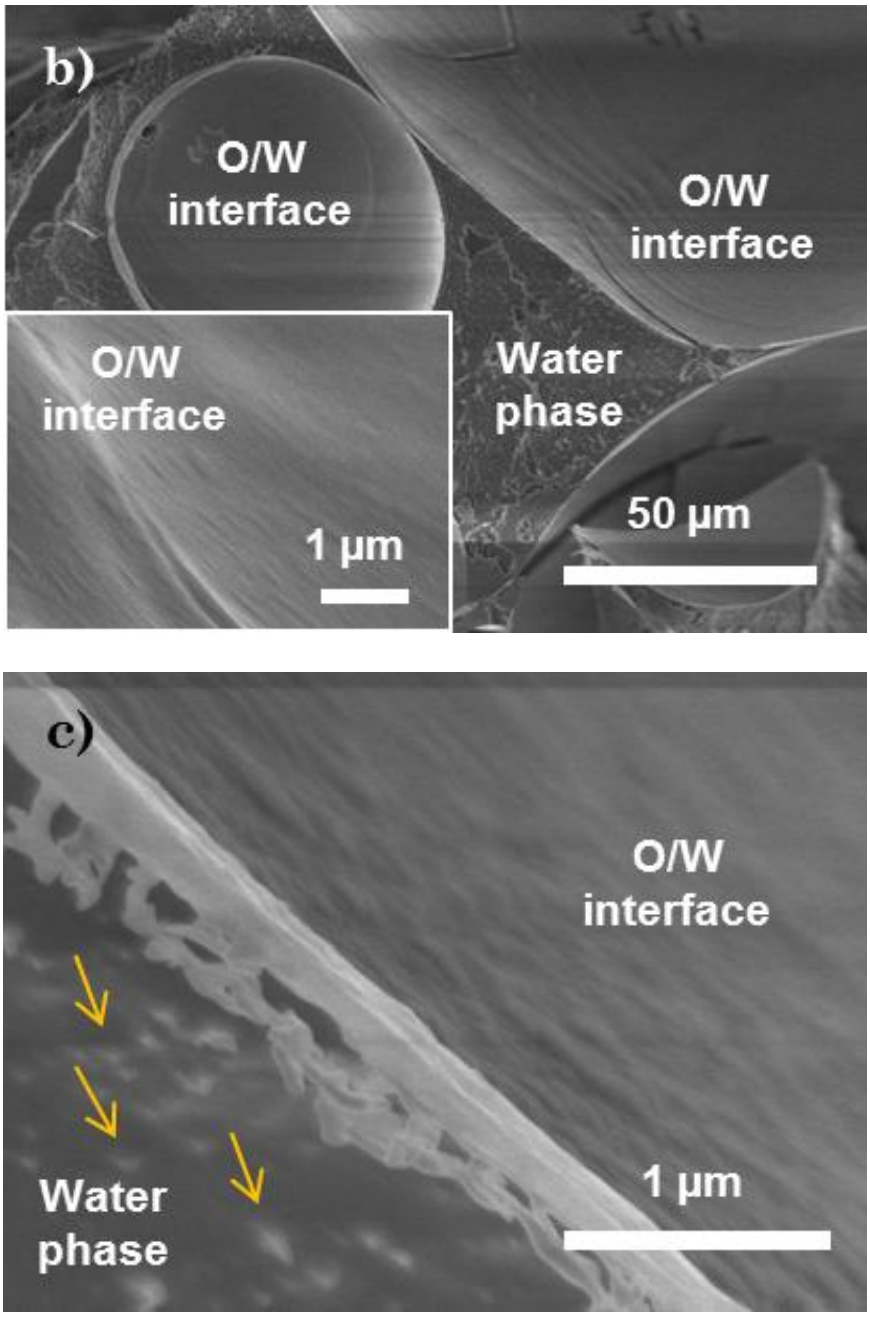

Figure 6.2 Cryo-SEM images of toluene – water emulsions formed by a) 500 ppm and b) 2000 ppm SiO_2-POEOMA hybrid nanoparticle (M_w = 37 kDa) in toluene solution, and c) cross section of the hybrid nanoparticle (2000 ppm) interfacial layer. Arrows indicate silica nanoparticle cores.

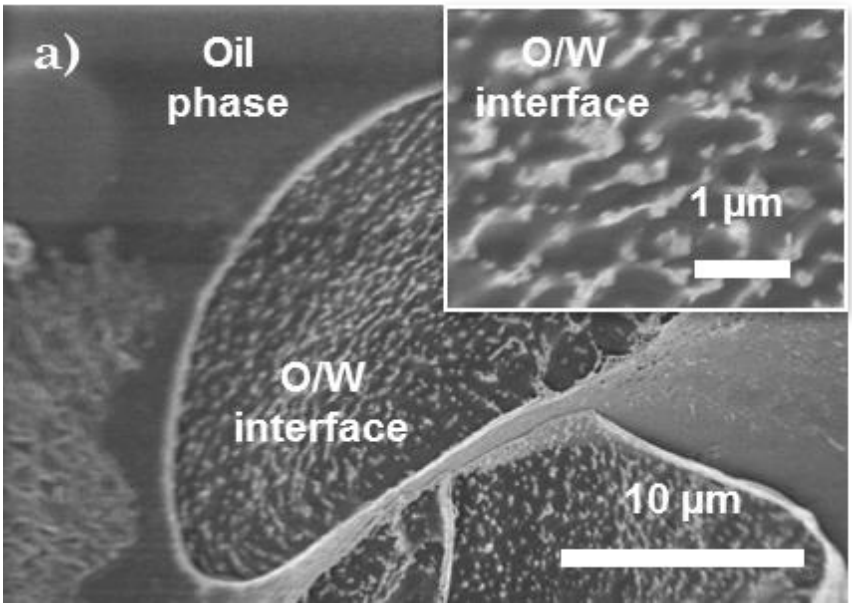

Figure 6.3 Cryo-SEM micrographs of hexane – water emulsions formed by 2000 ppm SiO_2-P(OEOMA-b-sty) (M_w = 104 kDa). Mean inter-particle distance is 376±120 nm at oil – water interface.

toluene – water interface, bright spots with ~15 nm diameter were observed (Figure 6.3) and those spots were considered as silica nanoparticle cores. SiO_2-P(OEOMA-b-sty) nanoparticles at the toluene – water interface was able to stretch its brushes into the dispersed water droplet of the water-in-oil emulsion due to the presence of the hydrophilic POEOMA component. This assuming is also supported by hairy structures arisen from the bright spots observed at the interface (Figure 6.3, inset). Therefore, with these stretched polymer brushes into the water droplet phase, the silica cores of SiO_2-P(OEOMA-b-sty) nanoparticles can be visually addressed at the toluene – water interface. Mean inter-particle distance (= mean hybrid particle diameter) of the silica cores were estimated from the micrograph as 376±120

nm which was large than the diameter of the same nanoparticles (146 nm) whose brushes were stretched in toluene (measured with DLS). This difference between the diameter of polymer grafted nanoparticles dispersed in bulk fluid and segregated at fluid interface agrees with the previous studies reported by Foster *et al.* and Isa *et al.*[39,45] Since the grafted polymer brushes stretch to the oil – water interface, the lateral brush height of hybrid particles increase from that in the bulk fluid phase. Figure 6.4 shows cross sections of interfacial layer of SiO_2-P(OEOMA-b-sty) nanoparticles in oil phase between the emulsion droplets. Due to the crush of the emulsion specimen, the cross section of the interfacial layer was revealed and somewhat sparse network-like structure was observed. The structure of this interfacial layer will be discussed later together with the interfacial layer of hardened emulsions.

10 days after the emulsification of toluene – water mixture using SiO_2-P(OEOMA-b-sty) nanoparticles, hardening (or solidification) of the emulsions was observed, and this phenomenon was not observed from the emulsion formed by SiO_2-P(OEOMA-b-sty) nanoparticles. The hardened emulsions lost their mobility and were stuck on the tube wall even if the tube flipped (Figure 6.5a). The optical micrograph of the dried hardened emulsions (Figure 6.5b) showed that the skeleton of the emulsion interfacial layer was maintained in spite of the hardening.

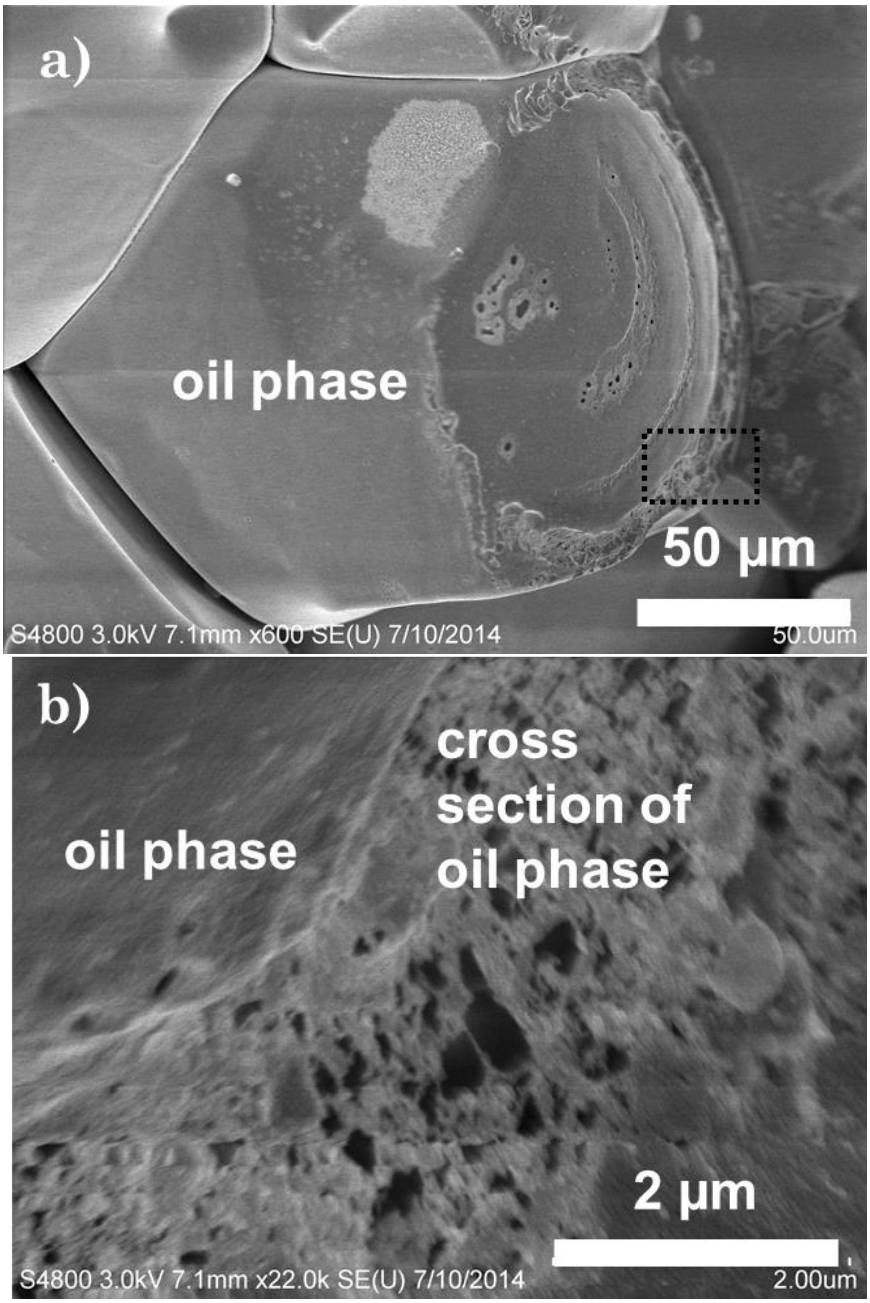

Figure 6.4 Cryo-SEM micrographs of a) oil (toluene) phases of emulsions formed by 2000 ppm SiO_2-P(OEOMA-b-sty) (M_w = 104 kDa), and b) cross section of oil phase.

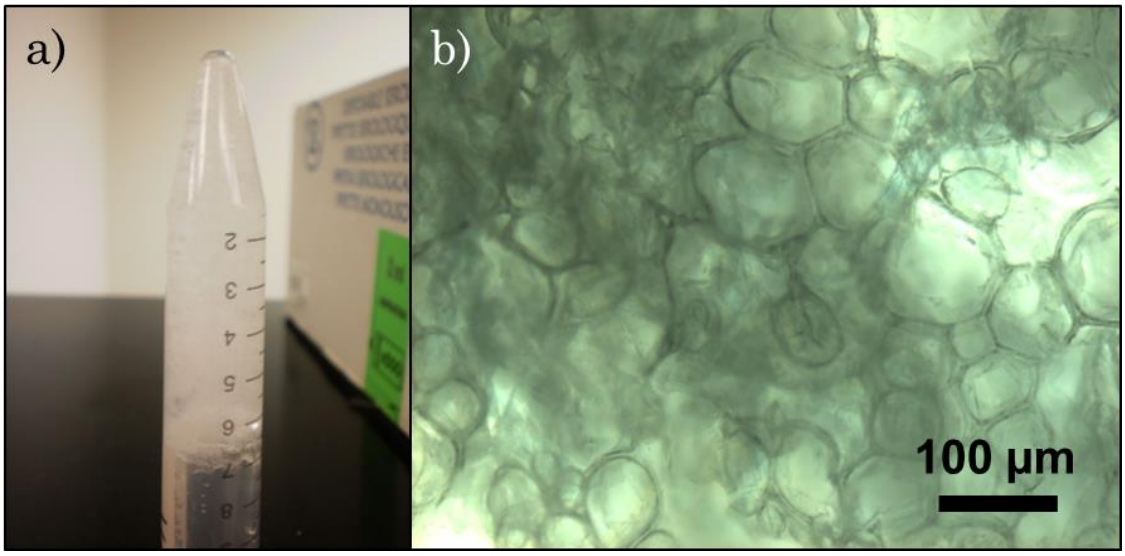

Figure 6.5 a) hardened emulsion formed 10 days after emulsification with SiO_2-P(OEOMA-b-sty) nanoparticles, b) an optical micrograph of hardened emulsion sample after drying under vacuum overnight.

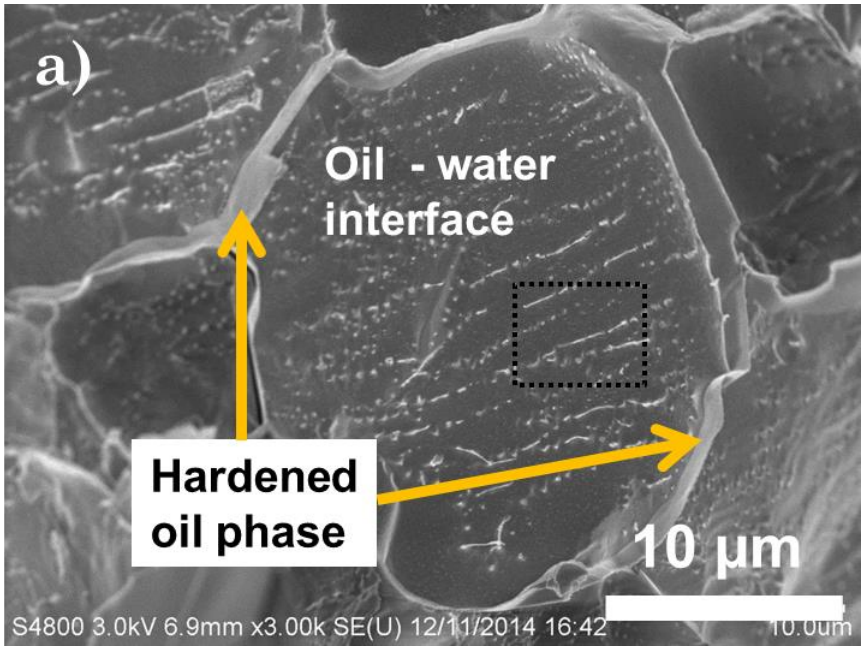

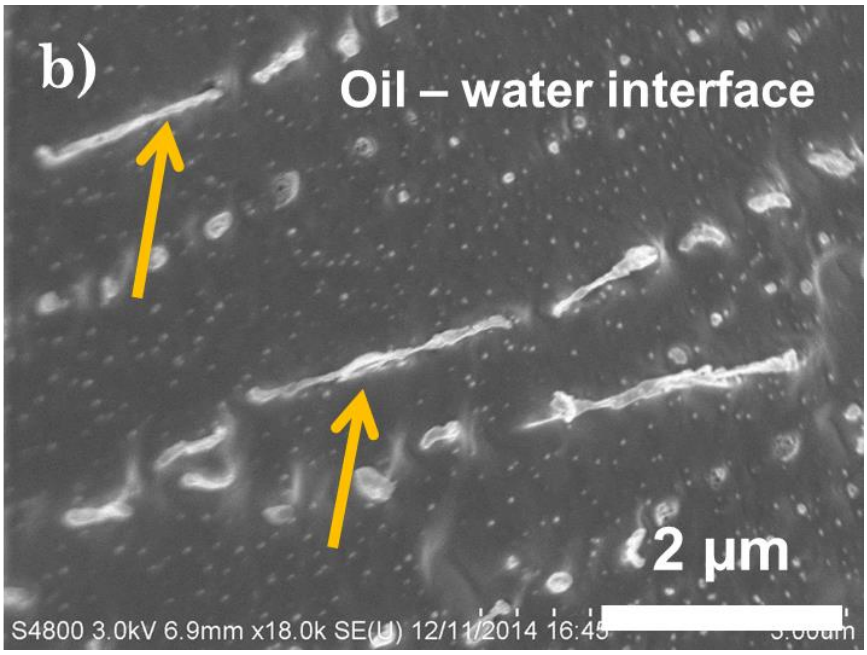

Figure 6.6 Cryo-SEM micrograph of a) hardened emulsion formed by SiO_2-P(OEOMA-b-sty); 104 kDa, b) oil – water interface. Mean inter-particle distance is 133±54 nm at oil – water interface.

In order to investigate the cause of the hardening and the behavior of the hybrid nanoparticles at the hardened emulsions, Cryo-SEM was used. The visualized oil – water interface and hardened oil phase of the hardened emulsions formed by SiO_2-P(OEOMA-b-sty) nanoparticles were presented in Figure 6.6. Hardened crust of oil phase, where the SiO_2-P(OEOMA-b-sty) nanoparticles were considered to be saturated, was observed between the emulsion droplets (Figure 6.6a). The segregation of nanoparticles were confirmed at the oil – water interface and the mean inter-particle distance of the silica cores of the SiO_2-P(OEOMA-b-sty) was measured as 133±54 nm. This distance is smaller than the inter-particle distance of the silica cores, measured from

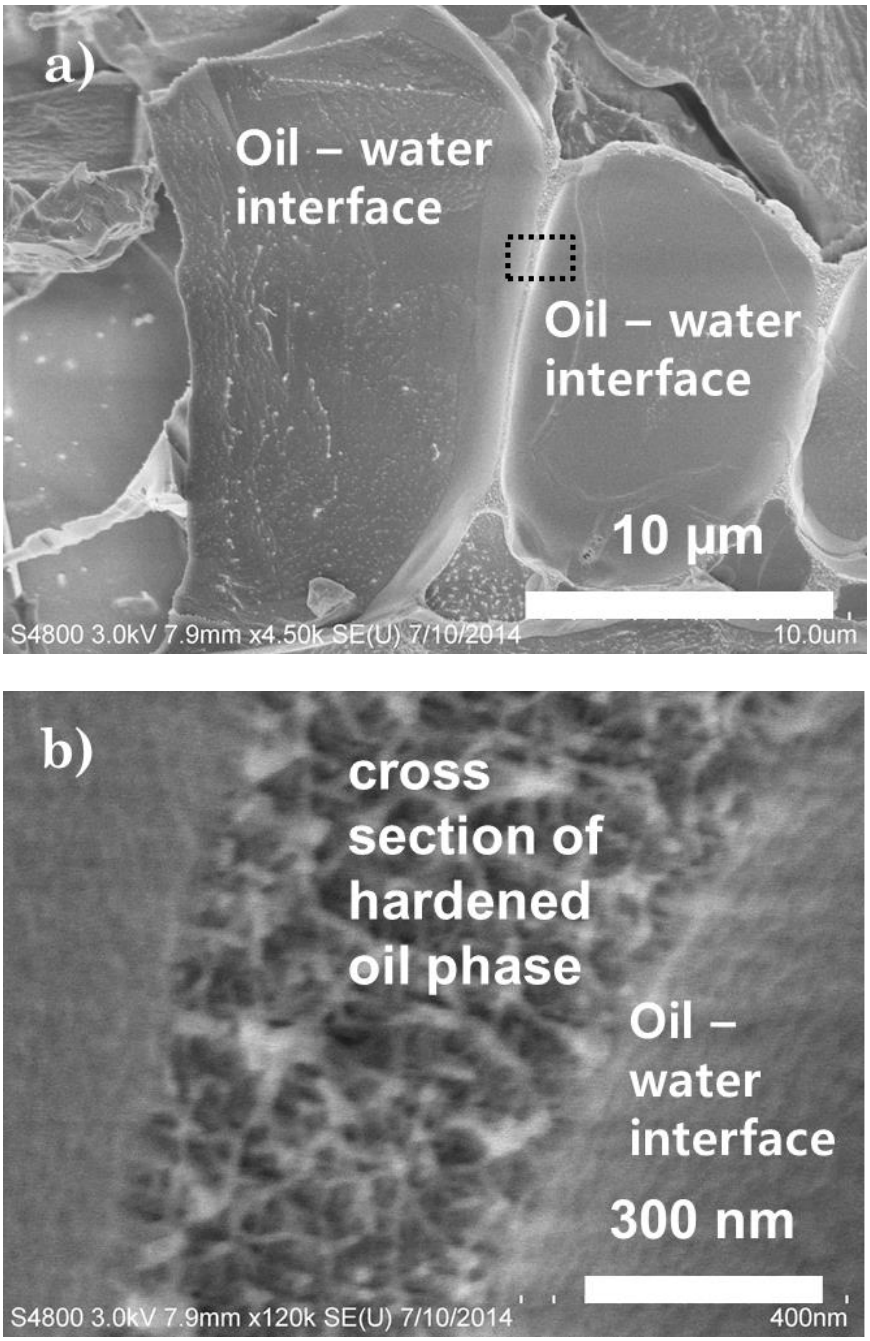

Figure 6.7 Cryo-SEM micrographs of a) the hardened emulsions formed by SiO_2-P(OEOMA-b-sty); 104 kDa, b) the interfacial layer of the hardened emulsions.

the emulsions made by same fluids and nanoparticles, before hardening (376±120 nm). Interestingly, linear aggregations of the nanoparticles were observed at the oil – water interface as well.

To clarify the cause of the hardening process, the interfacial layer of the hardened emulsions were further investigated by Cryo-SEM measurements. Figure 6.7b shows that the denser network structure of the cross section of the interfacial layer compared to that of unhardened emulsions presented in Figure 6.4b. This supports the observation of different inter-particle distances between hardened and unhardened emulsions.

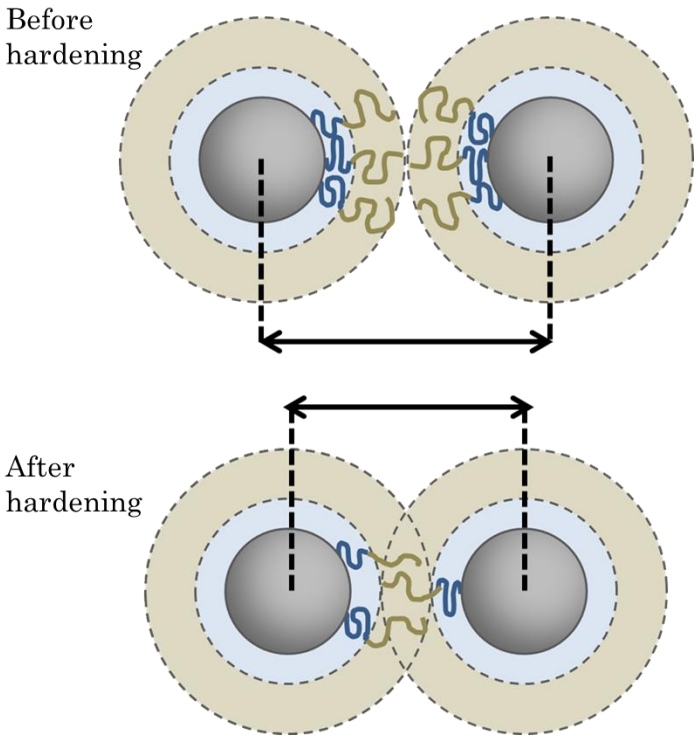

Figure 6.8 A proposed mechanism of emulsion hardening; gray spheres indicate silica cores, blue circles indicate inner polymer shell (POEOMA), and

Based on the Cryo-SEM investigations, a possible mechanism of the emulsion hardening phenomenon was proposed as presented in Figure 6.8. The decreased inter-particle distance after hardening (Figure 6.6) and the denser network-like structure of the interfacial layer (Figure 6.7) were observed from Cryo-SEM micrographs of the oil – water emulsions. These observations imply the copolymer brush rearrangement which is the similar behavior reported in many studies of the self-assembled amphiphilic block copolymers.[101,102] Therefore, the hybrid nanoparticles possibly approach each other by overlapping their outer polymer shell as a result of the self-assembly of the amphiphilic copolymer brushes (Figure 6.8). Consequently, hybrid nanoparticles, which are arranged densely, might become hardened.

6.4 Conclusions

Interfacial behaviors of polymer grafted nanoparticles were studied using Cryo-scanning microscopy of instantly frozen oil – water emulsions formed by those nanoparticles. The segregation of the nanoparticles at oil – water interface was confirmed from micrographs for all emulsion samples. The hybrid nanoparticles (SiO_2-POEOMA) with comparatively low concentration show void-compensating behavior at the oil – water interface in spite of their too low concentration to cover the whole area of the emulsion droplet.

The inter-particle distance, which can be considered as a particle diameter for the packed hybrid particles, was larger for the hybrid particles (SiO_2-P(OEOMA-b-sty)) at the oil – water interface compared to that for the hybrid particles in the bulk fluid due to the stretch of the polymer brushes toward the oil – water interface. 10 days after the emulsification, emulsion hardening was observed. Since the inter-particle distance of hardened emulsions is smaller than that of unhardened emulsions, the self-assembled copolymer brushes were suggested as a cause of this hardening phenomenon.

Chapter 7 Transport of carbon nanoparticles through Porous media

7.1 Introduction

The distinctive physical and chemical properties of nanoparticles, that can be tuned by varying molecular parameters, make them attractive for potential applications in oil and gas exploration and production.[1] For example, the temperature distribution of the reservoir can be sensed using the temperature-sensitive dyes attached nanoparticles,[103] and the surface area of the inter-well fractures can be probed using chemically modified nanoparticles, which move preferentially to the different pores.[104] The nanoparticles also can be applied to the oil recovery as enhancing agents. The structural disjoining pressure, which arise from arrangement of the nanoparticles at the three phase contact line of oil, rock, and the nanofluid, can help to detach the oil from the rock surface.[21] The effectiveness of the nanoparticles as enhanced oil recovery (EOR) agents has been reported experimentally using inorganic nanoparticles such as silica nanoparticles and polysilicon nanoparticles.[20,74,105]

However, applying the nanoparticles to the real oil field is challenging because their mechanical, chemical and electrical properties interact with rock surface under the non-uniform conditions such as temperature, permeability, salinity, and pressure. Therefore, understanding the behavior

of the nanoparticles in the porous media is crucial subject for application of nanoparticles to oil field. The transport behavior of small objects such as viruses and contaminants has mainly studied in the environmental and agricultural science area using the one dimensional convection-diffusion equation.[106-108] Combined with this equation, the core flooding experiment has been widely used to investigate the transport properties of the nanoparticles such as diffusion coefficients, differential pressure changes, and the particle retention. Yu *et al*. observed the effect of the salt on the breakthrough time and nanoparticle retention by the core flooding experiment with the carbon nanoparticles.[6] Kotsmar *et al*. studied the transport of magnetic iron oxide nanoparticles in the negatively charged core.[5] He *et al*. derived various transport parameters such as retardation factors and distribution coefficients of iron nanoparticles in porous media using CXTFIT codes.[52] However, studies about nanoparticle transport performed with various particle properties and rock conditions similar to the reservoir are still required to understand their behavior in the reservoir rock.

In this article, the transport behavior of negatively charged carbon nanoparticles with two different sizes was studied using the core flooding experiments. To mimic the harsh condition of the reservoir, rock cores having various properties were tested at two different temperatures and high pressure. Based on the nanoparticle breakthrough curves from the core flooding experiments and the one dimensional convection – dispersion

equation, transport parameters were estimated. The effect of the rock properties and the temperature on the nanoparticles' transport behavior through the porous media was studied and evaluated from these parameters.

7.2 Methodology

7.2.1 Materials

Sodium Chloride (99+%, Sigma-Aldrich), Sodium Sulfate (99+%, Sigma-Aldrich), Potassium Chloride (99+%, EMD chemicals), Sodium Bicarbonate (99.5+%, Sigma-Aldrich), Potassium Bromide (99+%, Sigma-Aldrich), Boric Acid (99.5+%, Sigma-Aldrich), Sodium fluoride (99%, Alfa Aesar), Magnesium Chloride hexahydrate (99+%, Mallinckrodt chemicals), Calcium Chloride dihydrate (99.5+%, EMD chemicals), Strontium Chloride hexahydrate (99+%, Alfa Aesar) used as received without further purification. Carbonate and sandstone cores (6 inch lehgth and 1.5 inch diameter) with various permeabilities were purchased from the Cleveland Quarries and Kocurek Industry respectively. Brine was prepared based on the literature.[109] The brine made by deionized water (DIW) and salts mixture was stirred a day and filtered by 200 nm PTFE filter paper using a vacuum pump.

7.2.2 Nanoparticle characterization

Negatively charged carbon nanoparticles, which were synthesized by the citrate chemistry, were received from Giannelis group.[55] Surface charges of the carbon nanoparticles were measured with Zetasizer Nano (Malvern). 2 wt% of 5 nm carbon nanoparticles and 0.1 wt% of 50 nm carbon nanoparticles in deionized water were prepared separately and their zeta potentials were measured. The high concentration

nanoparticle dispersions were used for sufficient particle count and signal intensity for the measurements. The diameters of the carbon nanoparticles (5 nm and 50 nm in diameters) were measured by transmission electron microscopy (TEM).

7.2.3 UV-vis spectroscopy

UV-vis spectrometer (V-570, Jasco) was used to measure the concentration of the nanoparticles in effluent solutions collected from core flooding experiments. To get the signal from the nanoparticles only, premeasured brine absorbance was subtracted from that of the nanoparticle – brine solution before the data processing. The absorbance peak intensity of 2000 ppm carbon nanoparticles – brine solution at certain wavelength (346 nm and 252 nm for 5 nm and 50 nm carbon nanoparticles respectively) was measured as a reference. Then the concentrations of the carbon nanoparticles in effluent solutions was estimated by comparing their absorbance peak intensity with reference value since each peak intensity is linearly proportional to the concentration of the carbon nanoparticles.

7.2.4 Fluorescence microscope

Fluorescence microscope was used on three different sections of the core (inlet, middle, outlet) in order to observe residual carbon nanoparticles adsorbed in the core after the core flooding experiments. Before the measurement, core was flushed with brine until nanoparticles was not appeared from the effluent. The excitation and emission wavelengths were 360 nm and 460 nm respectively and DAPI - EX 377/50 EM 447/60 filters were used.

7.2.5 Core flooding setup

The experimental set up was designed to mimic the reservoir conditions at the lab-scale and carry out the fluid transport experiment through a porous medium. The core

flooding setup consists of tri-axial core holder for placing the cylindrical rock piece, floating piston accumulator for storing and injecting nanoparticle solution, automatic sample collector for collecting the eluting samples, pressure transducers for recording the inlet and outlet pressures, and an oven for carrying out experiments at different temperatures.[74]

7.3 Results and discussion

In order to investigate the transport behavior of negatively charged carbon nanoparticles in porous media under various conditions, core flooding experiments were conducted. The photoluminescent carbon nanoparticles with nearly spherical geometry were synthesized by thermal oxidation of citrate salts.[55] The presence of sodium carboxylate groups on the carbon nanoparticle surface makes them charged negatively in water. The zeta potentials of the 5 nm and 50 nm carbon nanoparticles were -25 mV and -35 mV respectively. The carbon nanoparticles were dissolved in brine to make 20 ppm (by weight) dispersion and their stability in brine was confirmed using UV-vis spectrometer. For the 5 nm carbon nanoparticles, the absorbance peak was observed at the wavelength of 346 nm and a peak shift was not observed. However, for the 50 nm carbon nanoparticles, the absorbance peak was originally showed at the wavelength of 282 nm and then shifted to 252 nm in 5 days. (Figure 7.1a) We assume that the nanoparticle aggregates might induce the absorbance peak at comparatively higher wavelength but

the dispersion of the particles make the peak shift to the lower wavelength.[110,111] After stabilization of the absorbance peak, the concentrations of both 5 nm and 50 nm carbon nanoparticles were constant for 30 days. (Figure 7.1b)

Two different types of the rocks, sandstones and carbonates, with several different permeabilities were used as cylindrical porous cores for the nanoparticles transport experiments. The core size was selected as 3 inch in length (L) and 1.5 inch in diameter (d). The core was placed in the core holder and the radial pressure of 950 PSI and axial pressure of 450 PSI were applied. The pore volume of the core was obtained by measuring the volume of injected brine into the vacuumed core. The porosity was calculated based

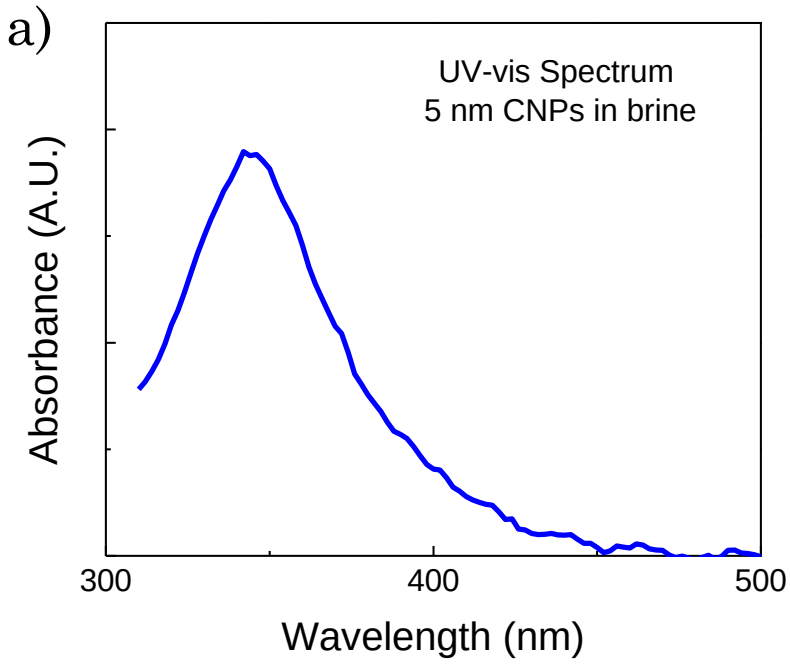

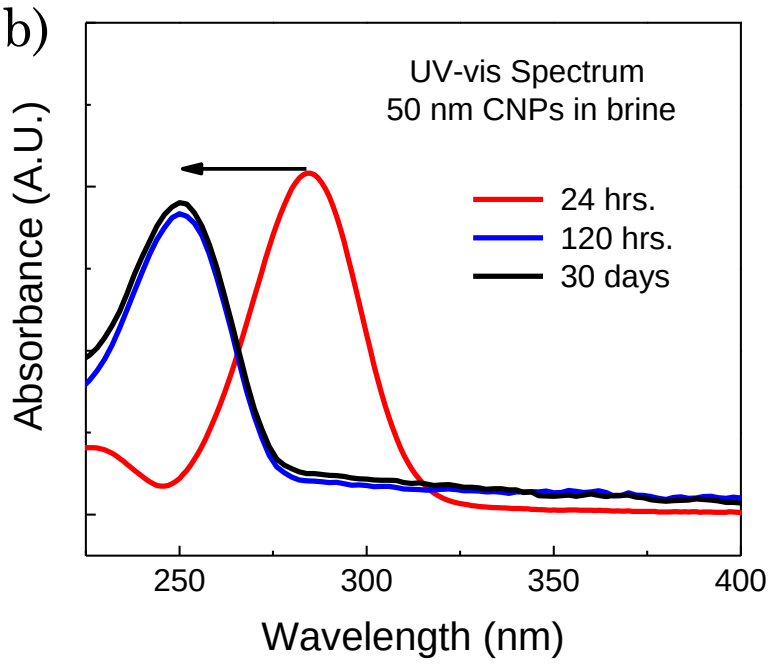
b)
UV-vis Spectrum
50 nm CNPs in brine
24 hrs.
120 hrs.
30 days
Absorbance (A.U.)
250
300
350
400
Wavelength (nm)

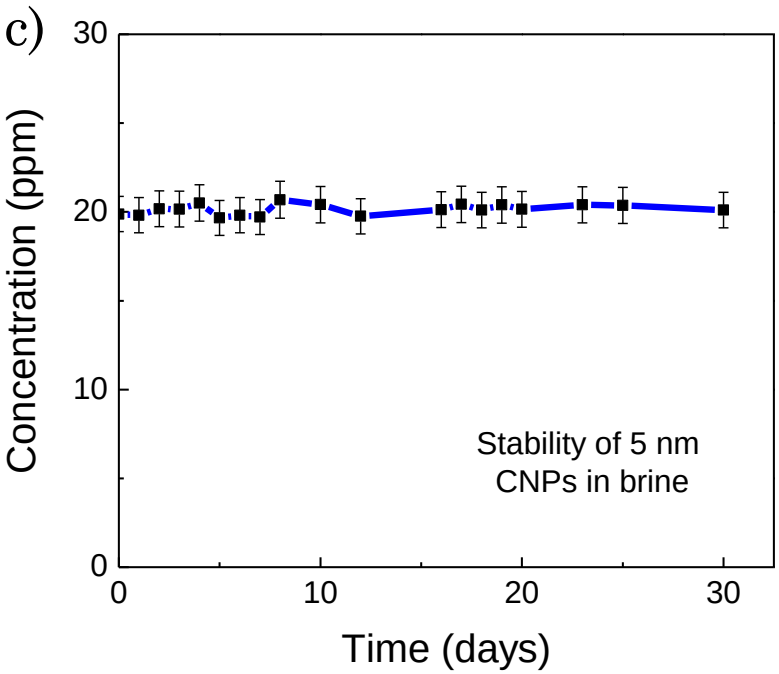
c)
30
20
10
0
Concentration (ppm)
Stability of 5 nm
CNPs in brine
0
10
20
30
Time (days)

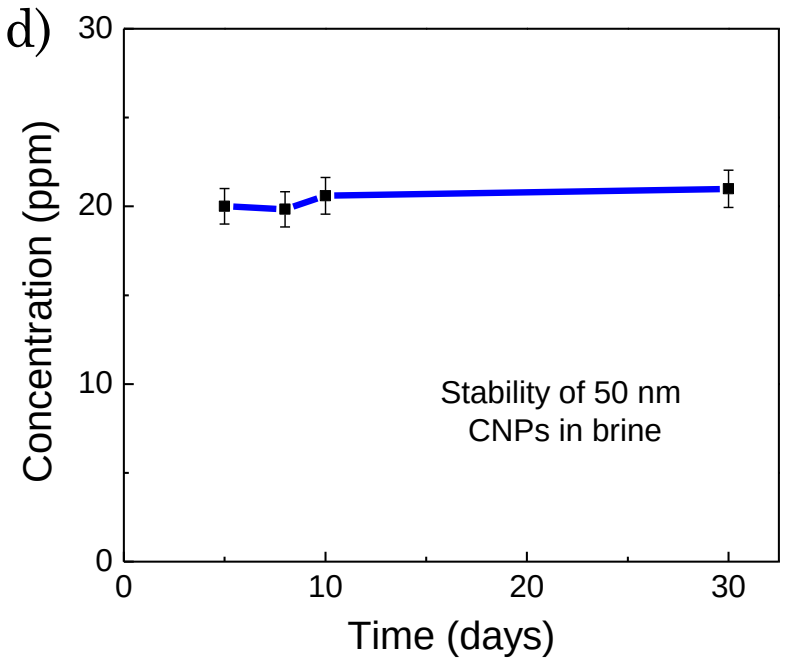

Figure 7.1 UV-vis spectroscopy of the (a) 5 nm and (b) 50 nm carbon nanoparticles and concentration of the (c) 5 nm and (d) 50 nm carbon nanoparticles as a function of time.

on the premeasured core geometry and the estimated pore volume. The permeability was calculated from the Darcy' law using the steady-state pressure difference across core at the several brine flow rates. These core properties were summarized in Table 7.1

Core flooding experiments were conducted with 1 ml/min flow rate at the two different temperature 25˚C and 95˚C. In every experiment, brine was flooded first and the flow was switched to the carbon nanoparticle solution. After 7~9 pore volumes of carbon nanoparticle solution flooding, the flow was re-switched to the brine. During the core flooding experiment, the pressure

Table 7.1 Summary of core properties

	S1	S2	S3	C1	C2
Rock type	sandstone	sandstone	sandstone	carbonate	carbonate
Permeability - before flooding (mD)	16	18	228	36	174
Permeability - after flooding (mD)	14	16	209	33	160
Porosity (%)	17	18	22	21	20
Pore Volume (cm^3)	14.1	14.1	17.1	17.4	16.4
Length of core (cm)	7.4	7.3	7.2	7.4	7.4
Diameter of core (cm)	3.8	3.7	3.7	3.7	3.7

difference across the core was recorded and effluents were collected. Nanoparticle breakthrough curve was made by measuring the concentration of the carbon nanoparticle in the effluent samples by the UV-vis spectroscopy (Figure 7.2). Differential pressure did not change significantly for all core flooding experiments. This is because both the pore size and pore throat size are at least several micrometers and this is very large compared to the carbon nanoparticles used in this study.[112] Moreover, the low nanoparticles concentration could minimize pore blockage induced by absorbed nanoparticle aggregates.[113] Nanoparticles

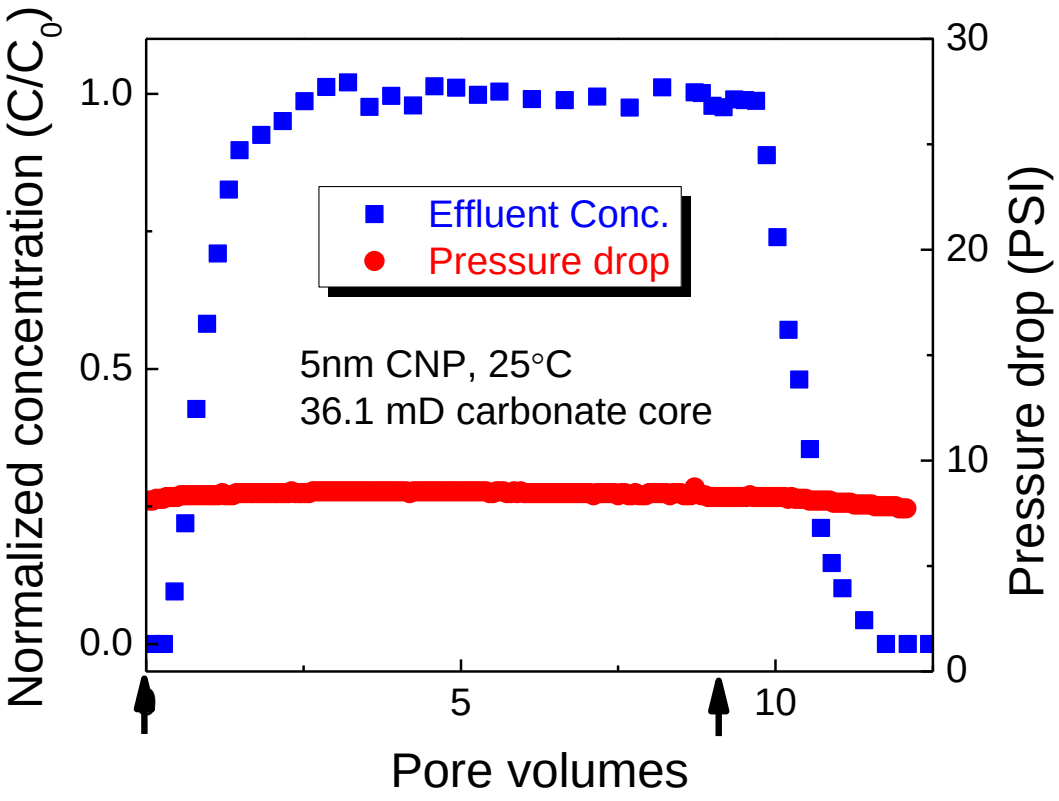

Figure 7.2 Core flooding with 20 ppm carbon nanoparticles. Arrows in the bottom indicate beginning and end of the nanoparticle injection.

were first observed earlier than 1 pore volume of the nanofluid flooding due to their comparatively high dispersion coefficient and small Peclet number (Table 7.2). After 3~4 pore volumes of the nanofluid flooding, the concentration of the nanoparticle reached to the original injected concentration and was retained as steady state (Figure 7.2).

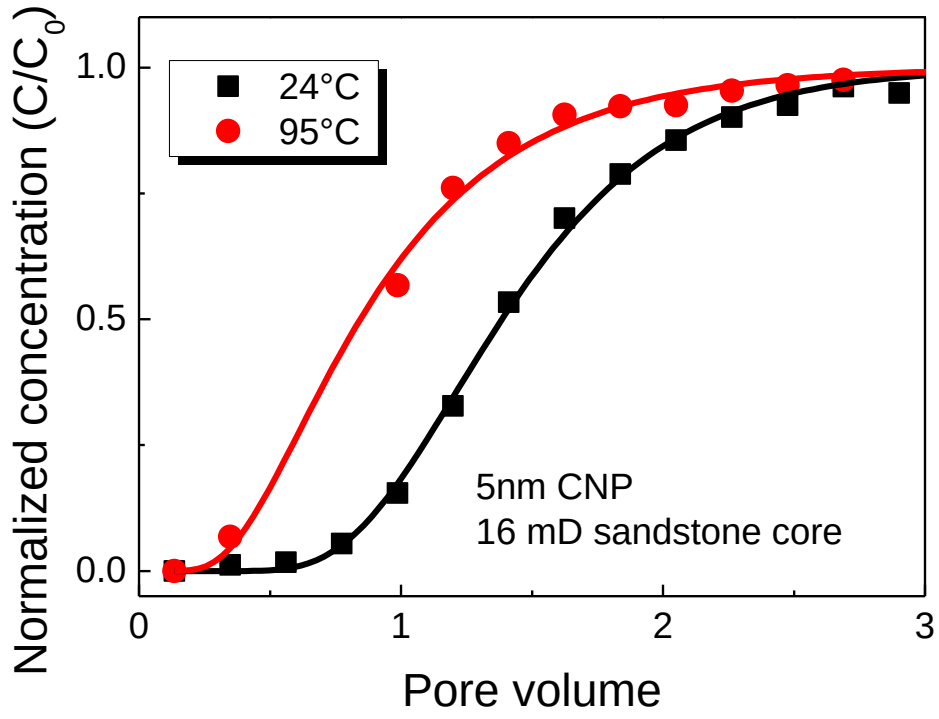
Normalized concentration (C/C0)
1.0
0.5
0.0
0
1
2
3
Pore volume
24°C
95°C
5nm CNP
16 mD sandstone core

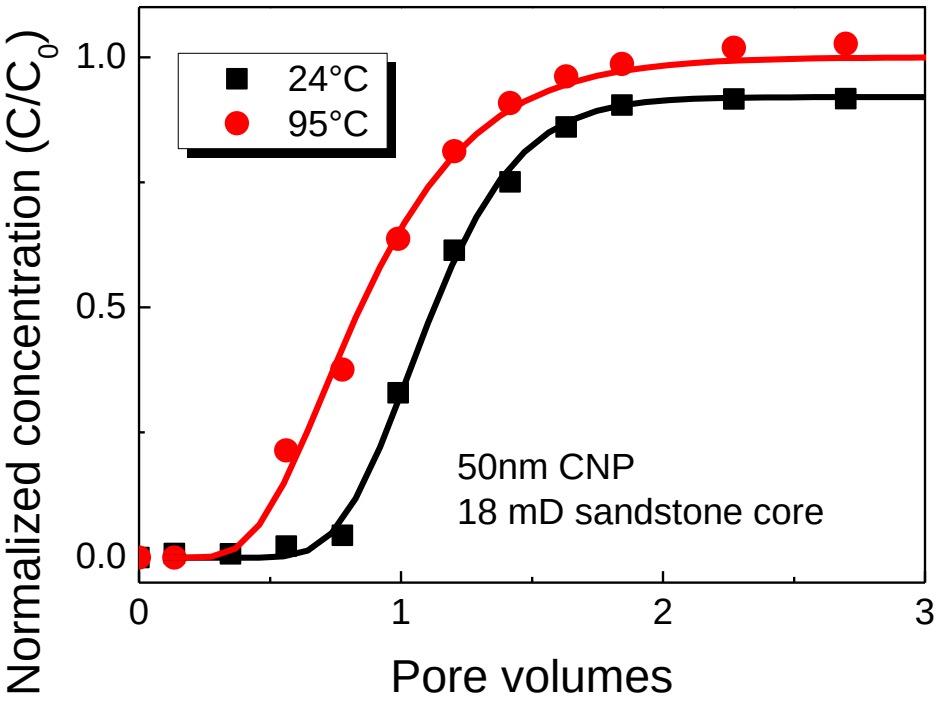
Normalized concentration (C/C0)
1.0
0.5
0.0
0
1
2
3
Pore volumes
24°C
95°C
50nm CNP
18 mD sandstone core

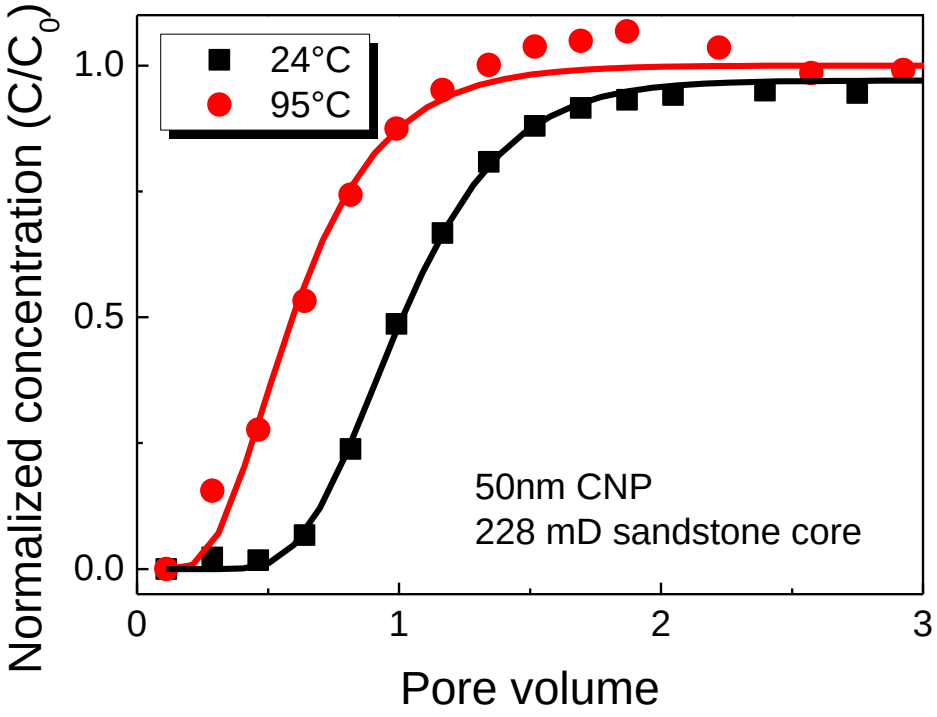
Normalized concentration (C/C0)
1.0
0.5
0.0
0
1
2
3
Pore volume
24°C
95°C
50nm CNP
228 mD sandstone core

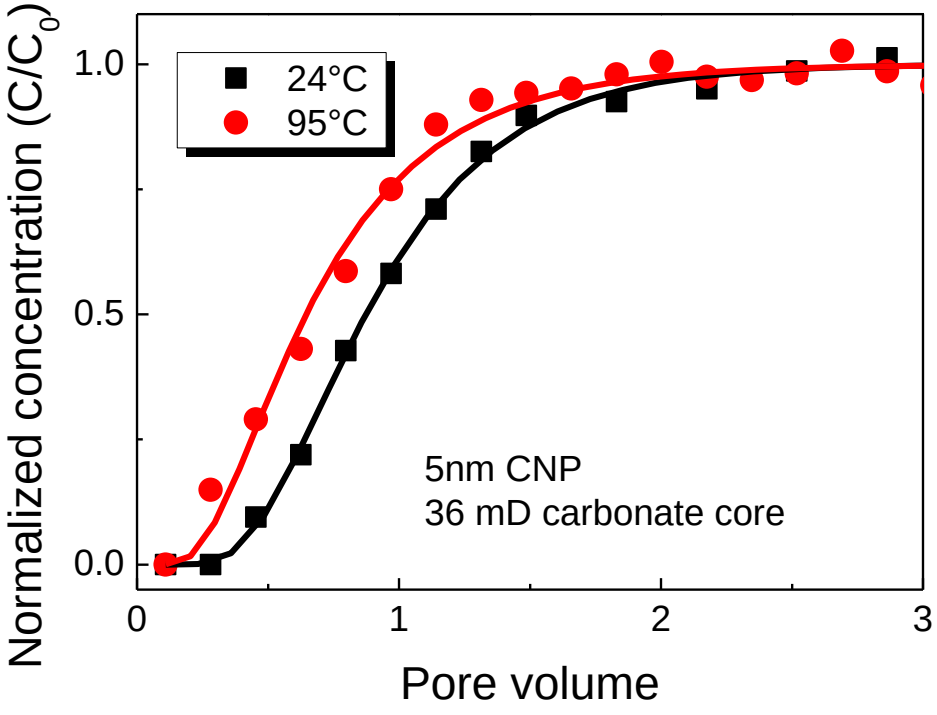
Normalized concentration (C/C0)
1.0
0.5
0.0
0
1
2
3
Pore volume
24°C
95°C
5nm CNP
36 mD carbonate core

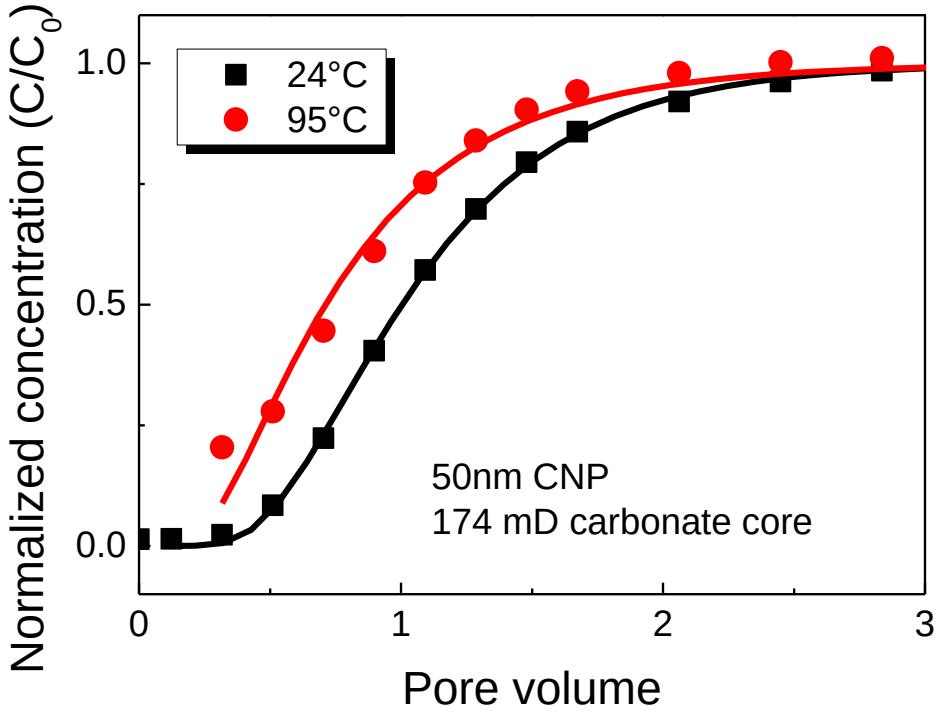

Figure 7.3 Fitting of core flooding experimental data using one dimensional convection – dispersion equation; Nanoparticle injection started from 0 pore volume.

To understand the effect of the various conditions such as temperature, particle size, and the rock permeability on the transport behavior of the nanoparticles in porous media, the breakthrough curves were simulated using the model equation. The simulated plots were fitted from experimental core flooding data using this analytical solution described in Chapter 2 (Figure 7.3) and estimated the retardation (R) factor and the dispersion coefficient (D). The estimated parameters are summarized in Table 7.2.

Table 7.2 Summary of transport parameters of core flooding experiments

	Peclet number		Dispersion coefficient (cm^2/min)		Retardation factor	
	25°C	95°C	25°C	95°C	25°C	95°C
S1 (16 mD)	2.42	0.98	0.27±0.02	0.48±0.06	1.46±0.01	1.00±0.02
S2 (18 mD)	4.85	1.58	0.14±0.00	0.43±0.05	1.36±0.01	1.11±0.03
S3 (228 mD)	3.72	1.97	0.18±0.02	0.34±0.07	1.01±0.00	0.63±0.02
C1 (36 mD)	1.35	0.98	0.51±0.06	0.70±0.06	1.27±0.02	0.97±0.03
C2 (174 mD)	1.30	0.77	0.53±0.02	0.89±0.06	1.11±0.02	0.86±0.02

The shape of the breakthrough curve is determined by the combined effect of the retardation factor and the dispersion coefficient if the normalized concentration and time scale were used. In general, breakthrough curve becomes more close to that of plug flow and shows stiffer slope when the Peclet number of the system is larger. If the other conditions such as length of the core and injection flow rate are identical, the Peclet number is inversely proportional to the dispersion coefficient.[114] In this point of view, the estimated dispersion coefficients were reasonable. For the two

breakthrough curves with similar retardation factors, the one with lower dispersion coefficients presented a stiffer curve compared to another with higher dispersion coefficient (Figure 7.4a). In addition, the higher retardation factor makes the breakthrough curve shift to the later time (eg. pore volume).[115] Based on this, the retardation factors estimated from the simulated plots seems to be reasonable as well. As shown in Figure 7.4b, for the two breakthrough curves with similar dispersion coefficients, the nanoparticles appearance was retarded by higher retardation factor.

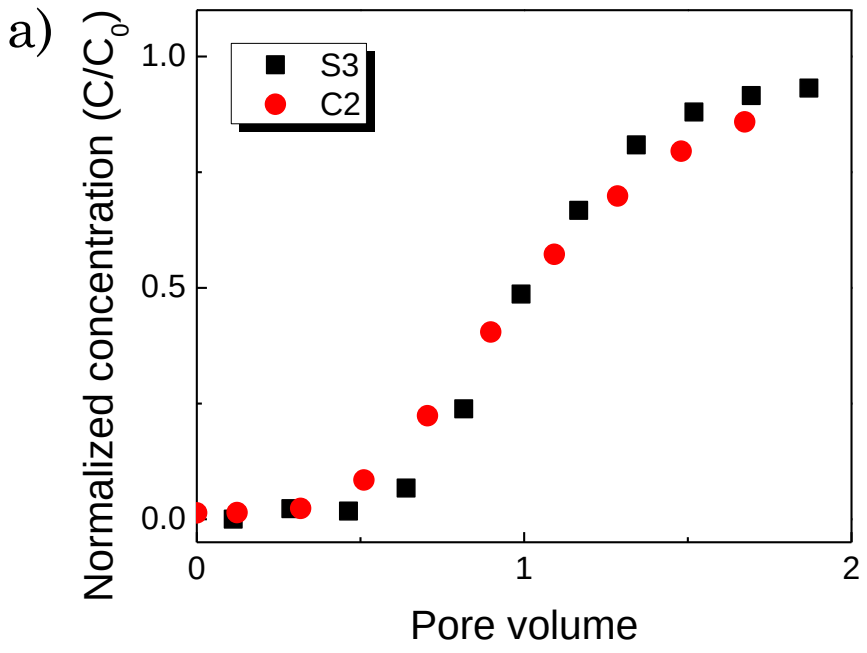

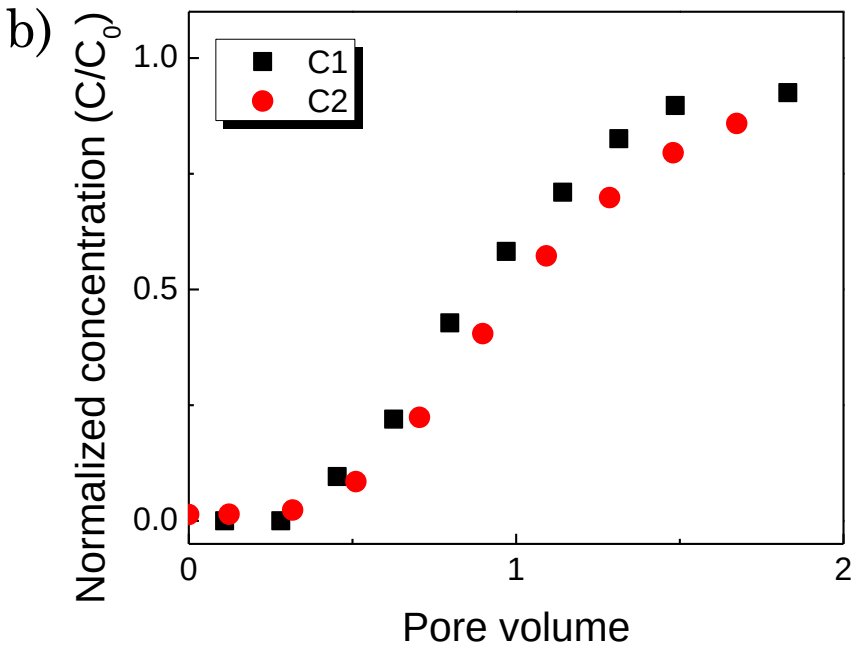

Figure 7.4 Shape transition in breakthrough curves of carbon nanoparticles by a) dispersion coefficients (S3: R=1.01, D=0.18 cm²/min, C2: R=1.11, D=0.53cm²/min), b) by retardation factors

The dispersion coefficients of the carbon nanoparticle at higher temperature were larger than those at lower temperature (Figure 7.5a). The dispersion coefficient can be expressed with combination of molecular diffusion and mechanical dispersion, which is

$$D = D_d + \alpha u^n, \qquad \text{(Eq 7.1)}$$

where D_d is diffusion coefficient, α is dispersivity, u is the pore velocity and n is empirical constant. Mechanical dispersion, which is expressed with coefficients α and n, originates from the local velocity variation in the porous media with heterogeneous pores. The diffusion coefficient represents the

random motion of the nanoparticles and can be expressed with Stokes-Einstein equation which is

$$D_d = \frac{k_b T}{6\pi\eta r}, \qquad \text{(Eq 7.2)}$$

where D_d is the diffusion coefficient, k_b is the Boltzmann constant, T is temperature, η is viscosity of the solution, and r is particle diameter. Since the molecular diffusion is proportional to the temperature, the dispersion coefficient is expected to be larger at higher temperature. As presented in Figure 7.5a, extracted dispersion coefficient from the experimental data showed agreement with this expectation. However, the dispersion coefficient was irrespective to the particles size. According to Delgado, the size of the particles transporting through the packed beds does not influence the dispersion coefficient as long as diameter of packed bed is 15 times larger than diameter of the particles.[116] Since the size of the carbon nanoparticles is very small compared to the size of rock grains of the core, the dispersion coefficient was independent to the size of the carbon nanoparticles.

The retardation factors of the carbon nanoparticle at higher temperature were smaller than those at lower temperature (Figure 7.5b). If the same core is used and only temperature changes, the retardation factor is a function of the partition coefficient (eq. 2.15). The partition coefficient K_b is expressed as

$$K_d = \frac{C_s}{C_l}, \qquad \text{(Eq 7.3)}$$

where C_s and C_l are the particle concentration in solid and liquid phase respectively.[117] At higher temperature, the higher thermal energy of the carbon nanoparticles makes more particles overcome the energy barrier of the particle adsorption on pore and the nanoparticles can be distributed to liquid phase more than solid phase. Therefore K_b decreased with increasing temperature, and the retardation factor decreases as well. In addition, the retardation factors of the carbon nanoparticles in higher permeable core were smaller than those in lower permeable core regardless of the type of the rock (Figure 7.6). Since the core with lower permeability has more small pores such as nanopores[118,119], the nanoparticles spend more time in these nanopores and their retention time increases. Therefore, K_d and R of the nanoparticles in the low permeability rock is larger than that in the high permeability rock.

The surface charge of the rock was another factor which influenced the transport parameters of carbon nanoparticles. Two different types of cores used in this study are sandstones and carbonates. Sandstones are predominantly composed of silica minerals which are negatively charged and the carbonates are positively charged because they are rich in calcium and magnesium ions.[50,51] Therefore, it is expected that negatively charged carbon

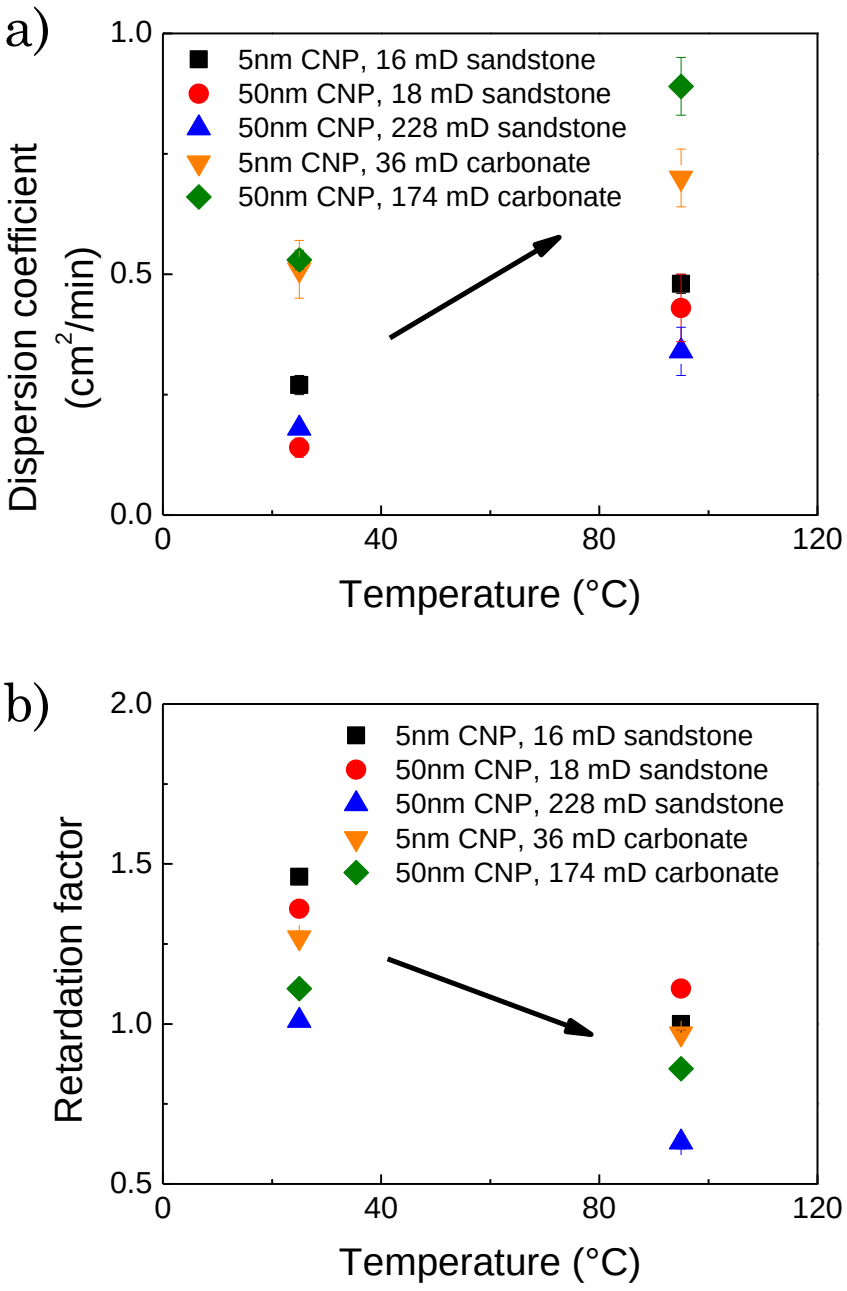

Figure 7.5 a) Dispersion coefficients and b) retardation factors extracted from the core flooding experiment as a function of temperature.

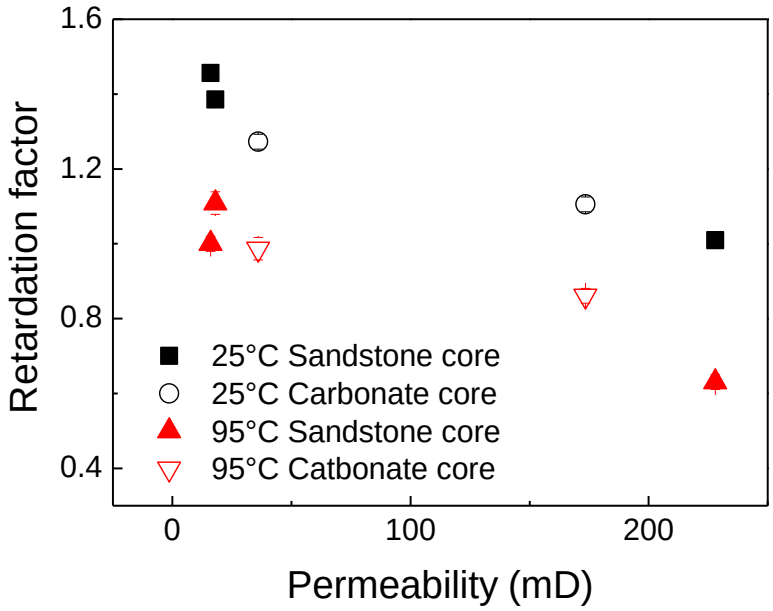

Figure 7.6 Retardation factor as a function of the permeability of the core. Some error bars for retardation factor were smaller than the symbols.

nanoparticles are preferentially attracted on positively charged carbonate cores rather than negatively charged sandstone cores. The UV fluorescence microscopy pictures taken from the cross sections of the core after the nanoparticle solution flooding confirmed that the carbon nanoparticles settled more on the positively charged carbonate pore surface than the negatively charged sandstone pore surface (Figure 7.7). Relatively higher dispersion coefficients of nanoparticles in sandstone cores compared to the carbonate cores support this observation (Figure 7.5a). The dispersion coefficient was irrespective of the particle size and the rock permeability. However, retardation factors were not significantly influenced by surface

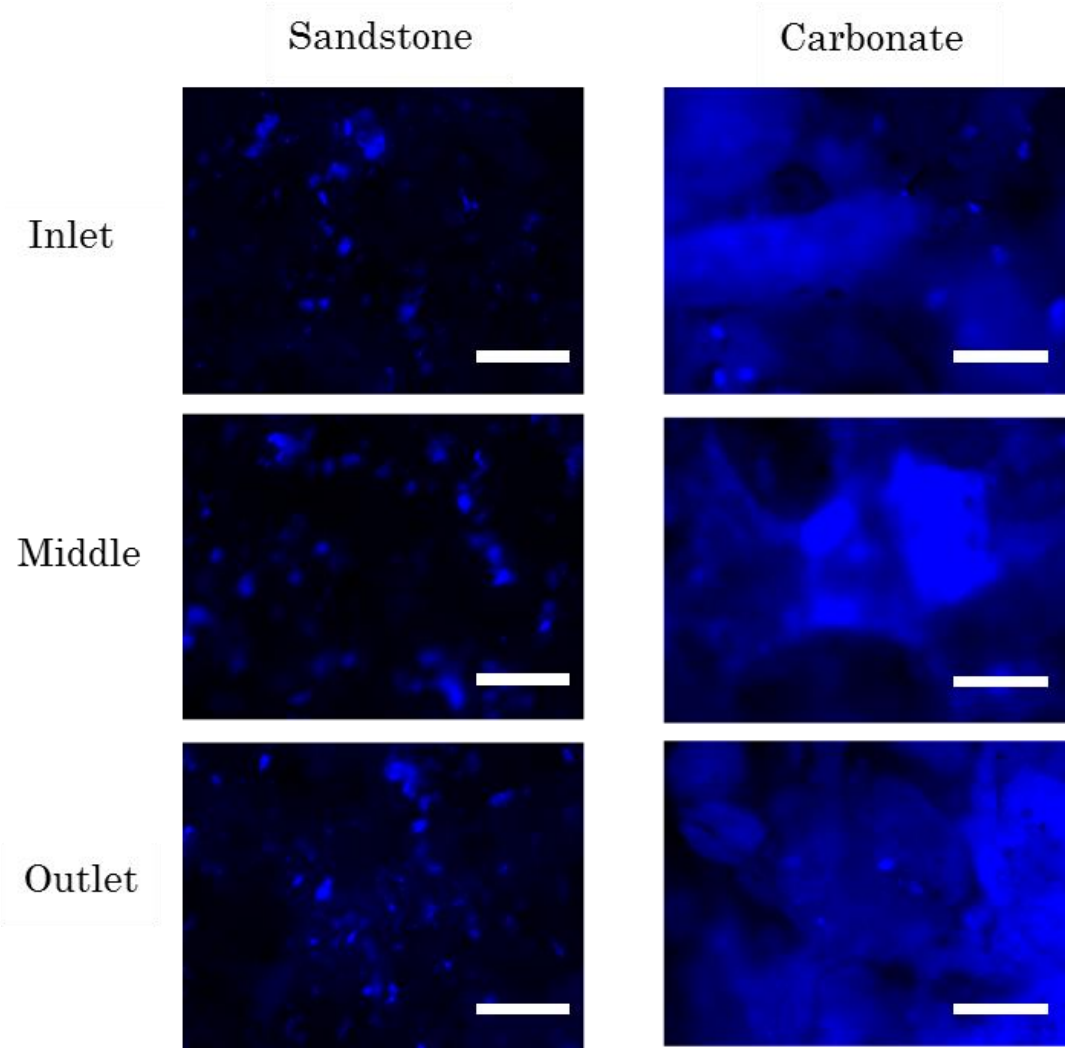

Figure 7.7 Fluorescence microscope measurements of cross sections at the inlet, middle, and outlet of the core. The scale bars indicate 200 μm.

charge interaction between cores and nanoparticles. This suggested that the retention time effect we discussed above is the dominant factor determining the retardation factor of the nanoparticle transport in porous media compared to the surface charge interaction.

7.4 Conclusion

Core flooding experiments were conducted to investigate the transport behavior of carbon nanoparticles in the cylindrical porous rock cores. Breakthrough curves of the carbon nanoparticles were made based on their concentrations in the effluent solutions and the curves were simulated with one dimensional convection – dispersion equation. Dispersion coefficients and retardation factors of each breakthrough curve were extracted from the simulated plot. The dispersion coefficients increased with increasing temperature from 25˚C and 95˚C due to larger molecular diffusion. The retardation factor decreased with increasing temperature because more nanoparticle can be distributed to the liquid phase at higher temperature. The retardation factor also decreased with increasing rock permeability because the more nanopores in the low permeable core made more interaction with nanoparticles and increase their retention time. Negative surface charge of the carbon nanoparticles made them to be absorbed on positively charged carbonate cores rather than negatively charged sandstone cores. The dispersion coefficient was larger when the nanoparticles and rock have opposite surface charge due to their attractive force. However, retardation factor of the carbon nanoparticles was not significantly influenced by surface charge interaction. This implies that the particle retention effect is dominant to determine the retardation factor of the nanoparticle transport in porous media.

Chapter 8 Summary and Conclusions

8.1 Summary and conclusions

Nanoparticles are promising materials which can be useful many areas in oil and gas industry due to their tunable properties and small size. In this dissertation, nanoparticles were studied in two different oil field applications which are environmentally friendly oil dispersants and nanosensors for reservoir characterizations.

As a candidate for non-toxic oil dispersants, the interfacial behavior of water-soluble poly(oligo(ethylene oxide) monomethyl ether methacrylate), grafted from 15 nm diameter silica nanoparticles using a living radical atom transfer polymerization technique, was examined for hexane and water interfaces. The polymer grafted nanoparticles (SiO_2-POEOMA) reduced the hexane – water interfacial tension from ~50 mN/m to ~20 mN/m at concentrations of silica in the range of 1 – 10 ppm. The hydrodynamic size of the dispersed hybrid nanoparticle, a function of the molecular weight of the polymer and the grafting density, was the dominant variable in determining the critical particle concentration and the efficacy of the hybrid nanoparticles in reducing hexane – water interfacial tension. A simple phenomenological model is used to explain the strong dependence of the critical particle concentration on the effective hydrodynamic size of the nanoparticles. Water

– hexane and water - squalene emulsions formed using 1000 ppm of hybrid nanoparticles were stable for more than 60 days.

To improve the interfacial activity of inorganic – polymer hybrid nanoparticles and further reduce the dispersed emulsion droplet size, amphiphilic block copolymers of poly(oligo(ethylene oxide) monomethyl ether methacrylate) (POEOMA) and polystyrene (PS) were grafted from silica (SiO_2) nanoparticles of 15 nm diameter using surface initiated atom transfer radical polymerization (ATRP) technique. Pendant drop interfacial tension measurements revealed significantly improved interfacial activity induced by introducing block copolymer brushes to the nanoparticles. Toluene – water interfacial tension decreased from ~30 mN/m to ~0.2 mN/m by SiO_2-P(OEOMA-b-sty) nanoparticles whereas it decreased from ~30 mN/m to ~5 mN/m by SiO_2-POEOMA nanoparticles. Moreover, more stable toluene – water emulsions were formed with smaller emulsion droplet size by SiO_2-P(OEOMA-b-sty) nanoparticels. The exponential correlation between the hydrodynamic size of the dispersed SiO_2-P(OEOMA-b-sty) nanoparticles and "critical core concentration" was observed as our previous study using SiO_2-POEOMA nanoparticles.

Cryo-scanning electron microscopy (SEM) of instantly frozen oil – water emulsions formed by those nanoparticles shows the interfacial behaviors of polymer grafted nanoparticles. From the Cryo-SEM measurements, the segregation of the nanoparticles at oil – water interface

was observed. The hybrid nanoparticles (SiO_2-POEOMA) shows unique void-compensating structures at the oil – water interface in spite of their low concentration to cover whole area of the emulsion droplet. The inter-particle distance increased for the hybrid particles (SiO_2-P(OEOMA-b-sty)) at the oil – water interface compared to that for the hybrid particles in the bulk fluid due to the stretch of the polymer brushes toward the oil – water interface. Interestingly, emulsion hardening was observed 10 days after the emulsification with SiO_2-P(OEOMA-b-sty) nanoparticles. Since the inter-particle distance of hardened emulsions is smaller than that of unhardened emulsions, the self-assembled copolymer brushes were suggested as a cause of this hardening phenomenon.

Since the transport behavior of the nanosensors in porous reservoir rock is essentially important for their commercialization, the single phase transport properties of brine dispersions of carbon nanoparticles in carbonate and sand stone cores with various permeabilities were studied as a function of temperature. Irrespective of rock type or permeability of the rock, with increased temperature an increased dispersion coefficient and a decreased retardation factor were observed by fitting of breakthrough curves. Also, the retardation factor was inversely proportional to the permeability of the rock. Florescence microscopy revealed that the carbon nanoparticles were preferentially absorbed on the carbonate rock pore rather than the sandstone rock pore due to the surface charge effect. This observation supported the

comparatively higher dispersion coefficients of the carbon nanoparticles in sandstone cores than those in carbonate cores.

8.2 Future works

Although a possible mechanism of the emulsion hardening induced by SiO_2-P(OEOMA-b-sty) nanoparticles was proposed based on the Cryo-SEM measurements, further studies are needed to verify the factors causing the hardening. To get the conformational information about the copolymer brushes in hardened emulsion matrix, transmitted electron microscopy (TEM) with selective staining of each copolymer block can be used. It is know that the phosphotungstic acid can selectively stain the ether group of POEOMA block of the copolymer brush. Therefore the TEM measurement will show the arrangement of each block separately and give useful information to confirm the cause of emulsion hardening. Moreover, small angle neutron scattering (SANS) techniques with deuterated solvents can be applied. With contrast matching of two solvents (oil and water) and silica core of the hybrid nanoparticles, the SANS measurements of oil – water emulsions give the only signal from the polymer brushes at oil – water interface.

In order to improve oil dispersion efficiency, nanoparticles with various geometries such as disk, sheet, and rod can be tested. In contrast to the sphere-like nanoparticles, nanoparticles with those geometries can cover more oil – water interfacial area per unit weight and this aspect is expected

to result in the improvement of the oil dispersing efficiency. The possible candidates of the nanoparticles can be carbon nanotubes (CNTs) and graphene sheet with hydrophilic polymers brushes grafted by the ATRP method. Hydrophobic CNTs/graphene surface and hydrophilic polymers are expected to act like surfactants and show good interfacial activity.

To recover heavy oil or oil in low permeability reservoirs, the nanoparticles with interfacially active polymer brushes can be used as enhanced oil recovery (EOR) agents. The polymer grafted nanoparticles possibly improve the oil recovery efficiency in two different ways. First, structural disjoining pressure induced from arrangement of the nanoparticles at the three phase contact line of oil, rock, and the nanofluid, can help to detach the oil from the rock surface. Moreover, their polymeric natures such as interfacial activity and higher viscosity expected to be effective to the oil recovery especially for heavy oil and low permeability reservoirs.

References

(1) Krishnamoorti, R. Extracting the benefits of nanotechnology for the oil industry *Journal of petroleum technology* **2006**, *58*.

(2) Nabhani, N.; Emami, M.; Moghadam, A. T. *Application of nanotechnology and nanomaterials in oil and gas industry*, AIP Publishing **2011**.

(3) Matteo, C.; Candido, P.; Vera, R. R.; Francesca, V. Current and future nanotech applications in the oil industry *American Journal of Applied Sciences* **2012**, *9*, 784.

(4) Ryoo, S.; Rahmani, A. R.; Yoon, K. Y.; Prodanović, M.; Kotsmar, C.; Milner, T. E.; Johnston, K. P.; Bryant, S. L.; Huh, C. Theoretical and experimental investigation of the motion of multiphase fluids containing paramagnetic nanoparticles in porous media *Journal of Petroleum Science and Engineering* **2012**, *81*, 129.

(5) Kotsmar, C.; Yoon, K. Y.; Yu, H.; Ryoo, S. Y.; Barth, J.; Shao, S.; Prodanović, M. a.; Milner, T. E.; Bryant, S. L.; Huh, C. Stable citrate-coated iron oxide superparamagnetic nanoclusters at high salinity *Industrial & Engineering Chemistry Research* **2010**, *49*, 12435.

(6) Yu, J.; Berlin, J. M.; Lu, W.; Zhang, L.; Kan, A. T.; Zhang, P.; Walsh, E. E.; Work, S.; Chen, W.; Tour, J. *Transport study of nanoparticles for oilfield application*, Society of Petroleum Engineers **2010**.

(7) Peyvandi, A.; Soroushian, P.; Balachandra, A. M.; Sobolev, K. Enhancement of the durability characteristics of concrete nanocomposite pipes with modified graphite nanoplatelets *Construction and Building Materials* **2013**, *47*, 111.

(8) Baker, M.; Rebholz, C.; Leyland, A.; Matthews, A. Electron spectroscopic studies of nanocomposite PVD TiAlBN coatings *Vacuum* **2002**, *67*, 471.

(9) Abdo, J.; Haneef, M. Clay nanoparticles modified drilling fluids for drilling of deep hydrocarbon wells *Applied Clay Science* **2013**, *86*, 76.

(10) Wasan, D. T.; Nikolov, A. D. Spreading of nanofluids on solids *Nature* **2003**, *423*, 156.

(11) Johnson, K.; Correspondent, S. Advances in nanotechnology hold huge potential promise in upstream applications *The American Oil and Gas Reporter. July issue* **2010**, 112.

(12) Huang, T.; Crews, J. B.; Willingham, J. R.; Pace, J. R.; Belcher, C. K. *Nano-sized particle-coated proppants for formation fines fixation in proppant packs*, Google Patents **2013**.

(13) González, J.; Figueiras, F.; Aranguren-Gassis, M.; Crespo, B.; Fernández, E.; Morán, X. A. G.; Nieto-Cid, M. Effect of a simulated oil spill on natural assemblages of marine phytoplankton enclosed in microcosms *Estuarine, Coastal and Shelf Science* **2009**, *83*, 265.

(14) Wolfe, D. A.; Hameedi, M.; Galt, J.; Watabayashi, G.; Short, J.; O'CLAIRE, C.; Rice, S.; Michel, J.; Payne, J.; Braddock, J. The fate of the oil spilled from the Exxon Valdez *Environmental science & technology* **1994**, *28*, 560A.

(15) Mullin, J. V.; Champ, M. A. Introduction/overview to in situ burning of oil spills *Spill Science & Technology Bulletin* **2003**, *8*, 323.

(16) Bob Graham, W. K. R. *Deep Water: The Gulf Oil Disaster and the Future of Offshore Drilling: Report to the President*, National Commission on the BP Deepwater Horizon Spill **2011**.

(17) Rico-Martínez, R.; Snell, T. W.; Shearer, T. L. Synergistic toxicity of Macondo crude oil and dispersant Corexit 9500A® to the Brachionus plicatilis species complex (Rotifera) *Environmental Pollution* **2013**, *173*, 5.

(18) Hamdan, L. J.; Fulmer, P. A. Effects of COREXIT® EC9500A on bacteria from a beach oiled by the Deepwater Horizon spill *Aquatic microbial ecology* **2011**, *63*, 101.

(19) Rodd, A. L.; Creighton, M. A.; Vaslet, C. A.; Rangel-Mendez, J. R.; Hurt, R. H.; Kane, A. B. Effects of Surface-Engineered Nanoparticle-Based Dispersants for Marine Oil Spills on the Model Organism Artemia franciscana *Environmental science & technology* **2014**, *48*, 6419.

(20) Ju, B.; Fan, T.; Ma, M. Enhanced oil recovery by flooding with hydrophilic nanoparticles *China Particuology* **2006**, *4*, 41.

(21) Chengara, A.; Nikolov, A. D.; Wasan, D. T.; Trokhymchuk, A.; Henderson, D. Spreading of nanofluids driven by the structural disjoining pressure gradient *Journal of colloid and interface science* **2004**, *280*, 192.

(22) Ogolo, N.; Olafuyi, O.; Onyekonwu, M. *Enhanced oil recovery using nanoparticles*, Society of Petroleum Engineers **2012**.

(23) Zhang, H.; Nikolov, A.; Wasan, D. Enhanced oil recovery (EOR) using nanoparticle dispersions: Underlying mechanism and imbibition experiments *Energy & Fuels* **2014**, *28*, 3002.

(24) Espinoza, D. A.; Caldelas, F. M.; Johnston, K. P.; Bryant, S. L.; Huh, C. *Nanoparticle-stabilized supercritical CO2 foams for potential mobility control applications*, Society of Petroleum Engineers **2010**.

(25) Beydoun, D.; Guang, D.; Chhabra, R.; Raper, J. A. Particle settling in oil-in-water emulsions *Powder technology* **1998**, *97*, 72.

(26) Verwey, E. J. W.; Overbeek, J. T. G.; Overbeek, J. T. G. *Theory of the stability of lyophobic colloids*; Courier Corporation, 1999.

(27) Becher, P. Emulsions: theory and practice **1965**.

(28) Dickinson, E.; Ritzoulis, C.; Yamamoto, Y.; Logan, H. Ostwald ripening of protein-stabilized emulsions: effect of transglutaminase crosslinking *Colloids and Surfaces B: Biointerfaces* **1999**, *12*, 139.

(29) Schuster, D. *Encyclopedia of emulsion technology*; CRC Press, 1996; Vol. 4.

(30) Derjaguin, B.; Landau, L. Theory of the stability of strongly charged lyophobic sols and of the adhesion of strongly charged particles in solutions of electrolytes *Progress in Surface Science* **1993**, *43*, 30.

(31) Verwey, E. Theory of the stability of lyophobic colloids *The Journal of Physical Chemistry* **1947**, *51*, 631.

(32) Hamaker, H. The London—van der Waals attraction between spherical particles *physica* **1937**, *4*, 1058.

(33) Bresme, F.; Oettel, M. Nanoparticles at fluid interfaces *Journal of Physics: Condensed Matter* **2007**, *19*, 413101.

(34) Binks, B.; Lumsdon, S. Influence of particle wettability on the type and stability of surfactant-free emulsions *Langmuir* **2000**, *16*, 8622.

(35) Binks, B.; Fletcher, P. Particles adsorbed at the oil-water interface: A theoretical comparison between spheres of uniform wettability and “Janus” particles *Langmuir* **2001**, *17*, 4708.

(36) Glaser, N.; Adams, D. J.; Böker, A.; Krausch, G. Janus particles at liquid-liquid interfaces *Langmuir* **2006**, *22*, 5227.

(37) Brittain, W. J.; Minko, S. A structural definition of polymer brushes *Journal of Polymer Science Part A: Polymer Chemistry* **2007**, *45*, 3505.

(38) Yoon, K. Y.; Li, Z.; Neilson, B. M.; Lee, W.; Huh, C.; Bryant, S. L.; Bielawski, C. W.; Johnston, K. P. Effect of adsorbed amphiphilic copolymers on the interfacial activity of superparamagnetic nanoclusters and the emulsification of oil in water *Macromolecules* **2012**, *45*, 5157.

(39) Foster, L. M.; Worthen, A. J.; Foster, E. L.; Dong, J.; Roach, C. M.; Metaxas, A. E.; Hardy, C. D.; Larsen, E. S.; Bollinger, J. A.; Truskett, T. M. High Interfacial Activity of Polymers “Grafted through” Functionalized Iron Oxide Nanoparticle Clusters *Langmuir* **2014**, *30*, 10188.

(40) Weiss, J.; Canceliere, C.; McClements, D. J. Mass transport phenomena in oil-in-water emulsions containing surfactant micelles: Ostwald ripening *Langmuir* **2000**, *16*, 6833.

(41) Alvarez, N. J.; Anna, S. L.; Saigal, T.; Tilton, R. D.; Walker, L. M. Interfacial dynamics and rheology of polymer-grafted nanoparticles at air–water and xylene–water interfaces *Langmuir* **2012**, *28*, 8052.

(42) Dong, J.; Li, J.; Zhou, J. Interfacial and phase transfer behaviors of polymer brush grafted amphiphilic nanoparticles: a computer simulation study *Langmuir* **2014**, *30*, 5599.

(43) Koski, J.; Chao, H.; Riggleman, R. A. Predicting the structure and interfacial activity of diblock brush, mixed brush, and Janus-grafted nanoparticles *Chemical Communications* **2015**.

(44) Saleh, N.; Sarbu, T.; Sirk, K.; Lowry, G. V.; Matyjaszewski, K.; Tilton, R. D. Oil-in-water emulsions stabilized by highly charged polyelectrolyte-grafted silica nanoparticles *Langmuir* **2005**, *21*, 9873.

(45) Isa, L.; Calzolari, D. C.; Pontoni, D.; Gillich, T.; Nelson, A.; Zirbs, R.; Sánchez-Ferrer, A.; Mezzenga, R.; Reimhult, E. Core–shell nanoparticle monolayers at planar liquid–liquid interfaces: effects of polymer architecture on the interface microstructure *Soft Matter* **2013**.

(46) van Rijn, P.; Park, H.; Özlem Nazli, K.; Mougin, N. C.; Böker, A. Self-Assembly Process of Soft Ferritin-PNIPAAm Conjugate Bionanoparticles at Polar–Apolar Interfaces *Langmuir* **2012**, *29*, 276.

(47) Saigal, T.; Dong, H.; Matyjaszewski, K.; Tilton, R. D. Pickering emulsions stabilized by nanoparticles with thermally responsive grafted polymer brushes *Langmuir* **2010**, *26*, 15200.

(48) Hiemenz, P. C.; Lodge, T. P. *Polymer chemistry*; CRC press, 2007.

(49) Matyjaszewski, K. Atom transfer radical polymerization (ATRP): current status and future perspectives *Macromolecules* **2012**, *45*, 4015.

(50) Sharma, M. M.; Kuo, J.; Yen, T. Further investigation of the surface charge properties of oxide surfaces in oil-bearing sands and sandstones *Journal of colloid and interface science* **1987**, *115*, 9.

(51) Agnihotri, R.; Mahuli, S. K.; Chauk, S. S.; Fan, L.-S. Influence of surface modifiers on the structure of precipitated calcium carbonate *Industrial & engineering chemistry research* **1999**, *38*, 2283.

(52) He, F.; Zhang, M.; Qian, T.; Zhao, D. Transport of carboxymethyl cellulose stabilized iron nanoparticles in porous media: Column experiments and modeling *Journal of colloid and interface science* **2009**, *334*, 96.

(53) Kumar, A.; Jaiswal, D. K.; Yadav, R. Analytical Solutions of One-Dimensional Temporally Dependent Advection-Diffusion Equation along Longitudinal Semi-Infinite Homogeneous Porous Domain for Uniform Flow.

(54) Misak, M. D. Equations for determining 1/H versus S values in computer calculations of interfacial tension by the pendent drop method *Journal of colloid and interface science* **1968**, *27*, 141.

(55) Bourlinos, A. B.; Stassinopoulos, A.; Anglos, D.; Zboril, R.; Georgakilas, V.; Giannelis, E. P. Photoluminescent carbogenic dots *Chemistry of Materials* **2008**, *20*, 4539.

(56) Wolfe, D. A.; Hameedi, M. J.; Galt, J. A.; Watabayashi, G.; Short, J.; O'Claire, C.; Rice, S.; Michel, J.; Payne, J. R.; Braddock, J.; Hanna, S.; Sale, D. The Fate

of the Oil Spilled from the Exxon Valdez *Environmental Science & Technology* **1994**, *28*, 560A.

(57) Hemmer, M. J.; Barron, M. G.; Greene, R. M. Comparative toxicity of eight oil dispersants, Louisiana sweet crude oil (LSC), and chemically dispersed LSC to two aquatic test species *Environmental Toxicology and Chemistry* **2011**, *30*, 2244.

(58) Wooten, K. J.; Finch, B. E.; Smith, P. N. Embryotoxicity of Corexit 9500 in mallard ducks (Anas platyrhynchos) *Ecotoxicology* **2012**, *21*, 662.

(59) Shafir, S.; Van Rijn, J.; Rinkevich, B. Short and long term toxicity of crude oil and oil dispersants to two representative coral species *Environmental Science & Technology* **2007**, *41*, 5571.

(60) Ramachandran, S. D.; Hodson, P. V.; Khan, C. W.; Lee, K. Oil dispersant increases PAH uptake by fish exposed to crude oil *Ecotoxicology and environmental safety* **2004**, *59*, 300.

(61) Berninger, J. P.; Williams, E. S.; Brooks, B. W. An initial probabilistic hazard assessment of oil dispersants approved by the United States National Contingency Plan *Environmental Toxicology and Chemistry* **2011**, *30*, 1704.

(62) Dickson, J. L.; Binks, B. P.; Johnston, K. P. Stabilization of carbon dioxide-in-water emulsions with silica nanoparticles *Langmuir* **2004**, *20*, 7976.

(63) Chiu, J. J.; Kim, B. J.; Kramer, E. J.; Pine, D. J. Control of nanoparticle location in block copolymers *Journal of the American Chemical Society* **2005**, *127*, 5036.

(64) Bansal, A.; Yang, H.; Li, C.; Cho, K.; Benicewicz, B. C.; Kumar, S. K.; Schadler, L. S. Quantitative equivalence between polymer nanocomposites and thin polymer films *Nature materials* **2005**, *4*, 693.

(65) Dong, J.; Worthen, A. J.; Foster, L. M.; Chen, Y.; Cornell, K. A.; Bryant, S. L.; Truskett, T. M.; Bielawski, C. W.; Johnston, K. P. Modified Montmorillonite Clay Microparticles for Stable Oil-in-Seawater Emulsions *ACS Appl Mater Interfaces* **2014**, *submitted*.

(66) Worthen, A. J.; Foster, L. M.; Dong, J.; Bollinger, J. A.; Peterman, A. H.; Pastora, L. E.; Bryant, S. L.; Truskett, T. M.; Bielawski, C. W.; Johnston, K. P. Synergistic Formation and Stabilization of Oil-in-Water Emulsions by a Weakly Interacting Mixture of Zwitterionic Surfactant and Silica Nanoparticles *Langmuir* **2014**, *30*, 984.

(67) Yusoff, A.; Murray, B. S. Modified starch granules as particle-stabilizers of oil-in-water emulsions *Food Hydrocolloids* **2011**, *25*, 42.

(68) Tikhonov, A. M. X-ray study of the electric double layer at the n-hexane/nanocolloidal silica interface *The Journal of chemical physics* **2006**, *124*, 164704.

(69) Al-Sahhaf, T.; Suttar Ahmed, A.; Elkamel, A. Producing ultralow interfacial tension at the oil/water interface *Petroleum science and technology* **2002**, *20*, 773.

(70) Zhou, J.; Qiao, X.; Binks, B. P.; Sun, K.; Bai, M.; Li, Y.; Liu, Y. Magnetic Pickering Emulsions Stabilized by Fe3O4 Nanoparticles *Langmuir* **2011**, *27*, 3308.

(71) Fujii, S.; Yokoyama, Y.; Miyanari, Y.; Shiono, T.; Ito, M.; Yusa, S.-i.; Nakamura, Y. Micrometer-sized gold-silica Janus particles as particulate emulsifiers *Langmuir* **2013**.

(72) Kini, G. C.; Biswal, S. L.; Wong, M. S.; Miller, C. A. Characteristics of spontaneously formed nanoemulsions in octane/AOT/brine systems *Journal of colloid and interface science* **2012**, *385*, 111.

(73) Goel, V.; Pietrasik, J.; Dong, H.; Sharma, J.; Matyjaszewski, K.; Krishnamoorti, R. Structure of polymer tethered highly grafted nanoparticles *Macromolecules* **2011**, *44*, 8129.

(74) Ponnapati, R.; Karazincir, O.; Dao, E.; Ng, R.; Mohanty, K.; Krishnamoorti, R. Polymer-functionalized nanoparticles for improving waterflood sweep efficiency: Characterization and transport properties *Industrial & engineering chemistry research* **2011**, *50*, 13030.

(75) Chevigny, C.; Dalmas, F.; Di Cola, E.; Gigmes, D.; Bertin, D.; Boué, F. o.; Jestin, J. Polymer-grafted-nanoparticles nanocomposites: Dispersion, grafted chain conformation, and rheological behavior *Macromolecules* **2010**, *44*, 122.

(76) Gibaud, T.; Mahmoudi, N.; Oberdisse, J.; Lindner, P.; Pedersen, J. S.; Oliveira, C. L.; Stradner, A.; Schurtenberger, P. New routes to food gels and glasses *Faraday discussions* **2012**, *158*, 267.

(77) Rotenberg, Y.; Boruvka, L.; Neumann, A. Determination of surface tension and contact angle from the shapes of axisymmetric fluid interfaces *Journal of colloid and interface science* **1983**, *93*, 169.

(78) Pasetto, P.; Blas, H. l. n.; Audouin, F.; Boissière, C. d.; Sanchez, C. m.; Save, M.; Charleux, B. Mechanistic Insight into Surface-Initiated Polymerization of Methyl Methacrylate and Styrene via ATRP from Ordered Mesoporous Silica Particles *Macromolecules* **2009**, *42*, 5983.

(79) Dong, J.; Xue, M.; Zink, J. I. Functioning of nanovalves on polymer coated mesoporous silica Nanoparticles *Nanoscale* **2013**, *5*, 10300.

(80) Vlassopoulos, D.; Fytas, G.; Pakula, T.; Roovers, J. Multiarm star polymers dynamics *Journal of Physics: Condensed Matter* **2001**, *13*, R855.

(81) Daoud, M.; Cotton, J. Star shaped polymers: a model for the conformation and its concentration dependence *Journal de Physique* **1982**, *43*, 531.

(82) Flory, P. J.; Rehner Jr, J. Statistical Mechanics of Cross-Linked Polymer Networks II. Swelling *The Journal of chemical physics* **1943**, *11*, 521.

(83) Aveyard, R.; Clint, J. H.; Nees, D.; Paunov, V. N. Compression and structure of monolayers of charged latex particles at air/water and octane/water interfaces *Langmuir* **2000**, *16*, 1969.

(84) Wang, Y.; Zhang, C.; Tang, C.; Li, J.; Shen, K.; Liu, J.; Qu, X.; Li, J.; Wang, Q.; Yang, Z. Emulsion interfacial synthesis of asymmetric Janus particles *Macromolecules* **2011**, *44*, 3787.

(85) Yu, J.; Berlin, J. M.; Lu, W.; Zhang, L.; Kan, A. T.; Zhang, P.; Walsh, E. E.; Work, S. N.; Chen, W.; Tour, J. M. *Transport study of nanoparticles for oilfield application*, **2010**.

(86) Sanguansri, P.; Augustin, M. A. Nanoscale materials development–a food industry perspective *Trends in Food Science & Technology* **2006**, *17*, 547.

(87) Gelperina, S.; Kisich, K.; Iseman, M. D.; Heifets, L. The potential advantages of nanoparticle drug delivery systems in chemotherapy of tuberculosis *American journal of respiratory and critical care medicine* **2005**, *172*, 1487.

(88) Pasetto, P.; Blas, H.; Audouin, F.; Boissiere, C.; Sanchez, C.; Save, M.; Charleux, B. Mechanistic insight into surface-initiated polymerization of methyl methacrylate and styrene via ATRP from ordered mesoporous silica particles *Macromolecules* **2009**, *42*, 5983.

(89) Sjoblom, J. *Encyclopedic handbook of emulsion technology*; CRC Press, 2010.

(90) Sherman, P. *Emulsion science*; Academic Press New York, 1968; Vol. 6.

(91) Raabe, O. G. Particle size analysis utilizing grouped data and the log-normal distribution *Journal of Aerosol Science* **1971**, *2*, 289.

(92) Liu, C.; Li, M.; Liang, C.; Wang, W. Measurement and analysis of bimodal drop size distribution in a rotor–stator homogenizer *Chemical Engineering Science* **2013**, *102*, 622.

(93) Triveni, R.; Shamala, T.; Rastogi, N. Optimised production and utilisation of exopolysaccharide from Agrobacterium radiobacter *Process Biochemistry* **2001**, *36*, 787.

(94) Craig, S.; Beaton, C. D. A simple cryo-SEM method for delicate plant tissues *Journal of Microscopy* **1996**, *182*, 102.

(95) Ferrer, M. L.; Garcia-Carvajal, Z. Y.; Yuste, L.; Rojo, F.; del Monte, F. Bacteria viability in sol-gel materials revisited: Cryo-SEM as a suitable tool to

study the structural integrity of encapsulated bacteria *Chemistry of materials* **2006**, *18*, 1458.

(96) Walther, P.; Hentschel, J.; Herter, P.; Müller, T.; Zierold, K. Imaging of intramembranous particles in frozen-hydrated cells (Saccharomyces cerevisiae) by high resolution cryo SEM *Scanning* **1990**, *12*, 300.

(97) Mikula, R.; Munoz, V. Characterization of emulsions and suspensions in the petroleum industry using cryo-SEM and CLSM *Colloids and Surfaces A: Physicochemical and Engineering Aspects* **2000**, *174*, 23.

(98) Destribats, M.; Lapeyre, V.; Wolfs, M.; Sellier, E.; Leal-Calderon, F.; Ravaine, V.; Schmitt, V. Soft microgels as Pickering emulsion stabilisers: role of particle deformability *Soft Matter* **2011**, *7*, 7689.

(99) Madivala, B.; Vandebril, S.; Fransaer, J.; Vermant, J. Exploiting particle shape in solid stabilized emulsions *Soft Matter* **2009**, *5*, 1717.

(100) Haase, M. F.; Grigoriev, D.; Moehwald, H.; Tiersch, B.; Shchukin, D. G. Encapsulation of amphoteric substances in a pH-sensitive Pickering emulsion *The Journal of Physical Chemistry C* **2010**, *114*, 17304.

(101) Klok, H. A.; Lecommandoux, S. Supramolecular materials via block copolymer self-assembly *Advanced Materials* **2001**, *13*, 1217.

(102) Register, R. A. Materials science: On the straight and narrow *Nature* **2003**, *424*, 378.

(103) Alaskar, M.; Ames, M.; Liu, C.; Connor, S.; Horne, R.; Li, K.; Cui, Y. *Smart Nanosensors for In-situ Temperature Measurement in fractured geothermal reservoirs*, **2011**.

(104) Rose, P.; Riasetto, D.; Siy, J.; Bartl, M.; Reimus, P.; Mella, M.; Leecaster, K.; Petty, S. *Quantum dots as tracers in geothermal and EGS reservoirs*, **2011**.

(105) Phuong-Tung Nguyen, S.; Do, B.-P. H.; Student, S.; Pham, D.-K.; Nguyen, H.-A.; Dao, D.-Q. P.; Nguyen, B.-D. Evaluation on the EOR potential capacity of the synthesized composite silica-core/polymer-shell nanoparticles blended with surfactant systems for the HPHT offshore reservoir conditions **2012**.

(106) Toride, N.; Leij, F.; Van Genuchten, M. T. *The CXTFIT Code for Estimating Transport Parameters from Laboratory Or Filed Tracer Experiments*; US Salinity Laboratory Riverside, CA, 1995.

(107) Jin, Y.; Yates, M. V.; Thompson, S. S.; Jury, W. A. Sorption of viruses during flow through saturated sand columns *Environmental Science & Technology* **1997**, *31*, 548.

(108) Pang, L.; Goltz, M.; Close, M. Application of the method of temporal moments to interpret solute transport with sorption and degradation *Journal of Contaminant Hydrology* **2003**, *60*, 123.

(109) Kester, D. R.; Duedall, I. W.; Connors, D. N.; Pytkowicz, R. M. Preparation of artificial seawater *Limnol. Oceanogr* **1967**, *12*, 176.

(110) Kato, H.; Nakamura, A.; Takahashi, K.; Kinugasa, S. Size effect on UV-Vis absorption properties of colloidal C60 particles in water *Physical Chemistry Chemical Physics* **2009**, *11*, 4946.

(111) Goh, E.; Xu, X.; McCormick, P. Effect of particle size on the UV absorbance of zinc oxide nanoparticles *Scripta Materialia* **2014**, *78*, 49.

(112) Nelson, P. H. Pore-throat sizes in sandstones, tight sandstones, and shales *AAPG bulletin* **2009**, *93*, 329.

(113) Ehtesabi, H.; Ahadian, M. M.; Taghikhani, V.; Ghazanfari, M. H. Enhanced Heavy Oil Recovery in Sandstone Cores Using TiO2 Nanofluids *Energy & Fuels* **2013**.

(114) Kühn, M.; Stöfen, H. *Reaction front fingering in anhydrite cemented sandstone*, **2001**.

(115) Starr, R.; Gillham, R.; Sudicky, E. Experimental investigation of solute transport in stratified porous media: 2. The reactive case *Water Resources Research* **1985**, *21*, 1043.

(116) Delgado, J. A critical review of dispersion in packed beds *Heat and mass transfer* **2006**, *42*, 279.

(117) Chin, Y.-P.; Peven, C. S.; Weber Jr, W. J. Estimating soil/sediment partition coefficients for organic compounds by high performance reverse phase liquid chromatography *Water Research* **1988**, *22*, 873.

(118) Gane, P. A.; Ridgway, C. J.; Lehtinen, E.; Valiullin, R.; Furo, I.; Schoelkopf, J.; Paulapuro, H.; Daicic, J. Comparison of NMR cryoporometry, mercury intrusion porosimetry, and DSC thermoporosimetry in characterizing pore size distributions of compressed finely ground calcium carbonate structures *Industrial & engineering chemistry research* **2004**, *43*, 7920.

(119) Rezaee, M.; Jafari, A.; Kazemzadeh, E. Relationships between permeability, porosity and pore throat size in carbonate rocks using regression

analysis and neural networks *Journal of Geophysics and Engineering* **2006**, *3*, 370.